Nanocomposites for Nitrogen Oxide Emissions Control in Lean-Burn Engines

by

Pemakorn Pitukmanorom

M. S. Chemical Engineering Practice
Massachusetts Institute of Technology, 2002

M. Eng. Chemical Engineering
University of Cambridge, 1999

B. A. Chemical Engineering
University of Cambridge, 1999

Submitted to the Department of Chemical Engineering
in Partial Fulfillment of the Requirements for the Degree of

Doctor of Philosophy in Chemical Engineering

at the

MASSACHUSETTS INSTITUTE OF TECHNOLOGY

September 2004

Author: _____
Department of Chemical Engineering
August 31, 2004

Certified by: _____
Jackie Y. Ying
Professor of Chemical Engineering
Thesis Supervisor

Accepted by: _____
Daniel Blankschtein
Professor of Chemical Engineering
Chairman, Committee for Graduate Studies

Nanocomposites for Nitrogen Oxide Emissions Control in Lean-Burn Engines

by

Pemakorn Pitukmanorom

M. S. Chemical Engineering Practice
Massachusetts Institute of Technology, 2002

M. Eng. Chemical Engineering
University of Cambridge, 1999

B. A. Chemical Engineering
University of Cambridge, 1999

Submitted to the Department of Chemical Engineering on August 31, 2004
in Partial Fulfillment of the Requirements for the Degree of
Doctor of Philosophy in Chemical Engineering

Abstract

Over the past few years, increase in environmental concern has led to a demand for more effective pollution control strategies that would satisfy the new EPA standards regarding automotive emissions of nitrogen oxides (NO_x). In particular, the removal of NO_x from lean-burn and diesel engines operating under an oxygen-rich atmosphere presents a significant challenge as conventional three-way catalysts are ineffective in this environment. Moreover, the presence of water vapor and sulfur oxides (SO_x) in the exhaust stream both inhibits catalyst activity and results in long-term catalyst instability. Thus, it is necessary to develop novel technologies for the removal of NO_x from the exhaust of lean-burn engines. This thesis examined three metal oxide nanocomposite systems to serve as (i) catalysts for the selective catalytic reduction (SCR) of NO_x by propene, (ii) sorbents for SO_2 storage, and (iii) catalysts for NO_x storage-reduction (NSR).

In_2O_3-Ga_2O_3/Al_2O_3 nanocomposite catalysts have been synthesized using the sequential precipitation technique. These alumina-based catalysts exhibited superior NO reduction activity to those produced by the impregnation and sol-gel methods due to their higher surface area and dispersion of active components. In fact, an excellent N_2 yield of 80% was achieved at 450°C over the In_2O_3-Ga_2O_3/Al_2O_3 nanocomposite with 2 wt% In and 8 wt% Ga. The high catalytic activity was attributed to better propene activation by In and improved NO_x adsorption on the high surface area Ga_2O_3/Al_2O_3. The In_2O_3-Ga_2O_3/Al_2O_3 nanocomposite remained active even in the presence of SO_2. The NO reduction activity of this catalyst system depended on the hydrocarbons that were used as the reducing agents. Propene was found to be a more effective reducing agent than propane in the SCR of NO.

Pt-Rh/CuO/Al_2O_3 nanocomposites capable of adsorbing SO_2 in oxygen-rich environment as metal sulfates and releasing SO_2 in reducing atmosphere were synthesized with sequential precipitation technique. These CuO-based sorbents possessed excellent SO_2 adsorption capacity and superior regenerability by CO compared to those produced by the impregnation method due to higher surface area and dispersion of Cu species. A gram of sorbent with 30 wt% Cu could adsorb over 50 mg of SO_2 before SO_2 breakthrough was observed. The rate of SO_2 desorption from the CuO/Al_2O_3 sorbents could be enhanced through the incorporation of noble metals. With the use of 0.1 wt% Pt, the CuO/Al_2O_3 sorbent with 30 wt% Cu could be regenerated twice as quickly. Also, on average only 8 ppm of SO_2 were detected downstream of this sorbent over each adsorption cycle at 400°C. The excellent sorbent regeneration was attributed to better CO adsorption and lower sulfate decomposition temperature as a result of Pt addition. The nature of sulfur deactivation of these sorbents was highly dependent on the composition of noble metals used. By employing both Rh and Pt, sorbent regeneration rate and stability could be optimized.

Rh/CuO-MgO/Al_2O_3 nanocomposites capable of adsorbing NO_x and SO_2 in oxygen-rich environment and releasing N_2 and SO_2 in reducing atmosphere were successfully prepared by sequential precipitation. These novel sorbents were able to maintain NSR activities in the presence of SO_2 due to the excellent SO_2 desorption efficiency provided by both CuO and noble metals. The addition of Pt improved the rate of SO_2 desorption of the CuO/Al_2O_3 sorbents, but led to reduced stability for the adsorbed nitrates, resulting in poor NO_x adsorption. The use of Rh, on the other hand, significantly enhanced the NO_x storage under oxygen-rich conditions. Further improvement in the NO_x storage capacity of the Pt-Rh/CuO/Al_2O_3 sorbent was achieved through the incorporation of MgO. Although the MgO addition greatly increased the NO breakthrough capacity and allowed almost complete NO conversion, it also resulted in lower SO_2 desorption efficiency. With the loading of 12 wt% Mg and 18 wt% Cu, the Rh/CuO-MgO/Al_2O_3 sorbent was able to maintain its NSR activity over 6 hours of operation at 300°C. The activity of the aged sorbent could be recovered by regeneration at 500°C under CO, providing a stable NO conversion of over 85%.

Thesis Supervisor: Jackie. Y. Ying
Title: Professor of Chemical Engineering

Acknowledgments

First and foremost, I thank Professor Jackie Ying for giving me the opportunity to work on this thesis project and I am grateful for her encouragement and guidance throughout my research. I also thank my thesis committee members: Professor William Green, Professor Jack Howard, Professor Paul Laibinis and Professor Bernhardt Trout for valuable suggestions on this project.

I would like to thank the members of the Nanostructured Materials Research Laboratory for their support during my time at MIT. In particular, Dr. Michael Wong, Dr. Edward Ahn, Dr. Neeraj Sangar and Dr. Justin McCue for many discussions that helped me in initiating my research. I also thank Dr. Jason Sweeney for his help and advice; his work on nanocomposites for SO_2 adsorption provided the foundation for my work on the SO_2 storage materials. I was fortunate to have worked with Dr. Javier García-Martínez, Dr. Todd Zion, Dr. Thomas Lancaster and Steven Weiss, who have provided many interesting discussions and broadened my knowledge beyond the immediate scope of my research. Finally, I like to thank Tseh-Hwan Yong and Dr. Yee San Su for their friendship both inside and outside of the lab, which helped me through the tougher days of my work and put many smiles on my face.

I would like to acknowledge Michael Frongillo and Dr. Anthony Garratt-Reed of the MIT CMSE for their assistance with electron microscopy. I also thank Linda Mousseau for all her administrative assistance throughout my time in this research group.

Most of all, I like to thank my parents for their love and encouragements that have allowed me to pursue my own interest and accomplish the work presented here. Their financial support along with those of my uncle and my grandmother for my studies overseas these past 13 years are also greatly appreciated.

This research was supported by the David and Lucile Packard Foundation and the MIT Institute for Soldier Nanotechnologies (funded in part by the Army Research Office).

Contents

List of Figures

List of Tables

List of Symbols

r_o initial grain radius
r_u unreacted radius
X conversion at breakthrough

Chapter 1 – Background and Research Motivation

Over the past decades, atmospheric emissions of nitrogen oxides (NO_x) have been scrutinized by many environmental and regulatory agencies around the world because of the harmful effects these compounds have on both human health and the environment. Exposure to high levels of NO_x produces immediate acute effects in human such as cyanosis and pulmonary edema, while prolonged exposure to NO_x above natural levels leads to bronchitis, pneumonia, and alterations to the immune system [1]. In addition, NO_x also contributes to the formation of urban smog and acid rain. Although a significant proportion of NO_x is natural in origin, emissions of NO_x from anthropogenic sources present a greater concern because of their proximity to the population. Of all the man-made NO_x emitted in the United States in 1992, 45% arose from the combustion of fossil fuels inside the engines of motor vehicles [2]. The development of improved methods to reduce NO_x emissions from this type of non-stationary source is therefore of critical importance to the global environment.

1.1. NO_x Emissions from Internal Combustion Engines

Although many strategies are being developed for the treatment of NO_x in gasoline and diesel engines, the effectiveness of each method depends primarily on the temperature, pressure and composition of the exhaust stream. These three factors in turn are dictated by both the type of engine and the conditions under which the engine operates. One of the main parameter that influences these conditions is the engine's intake air-to-fuel (A/F) ratio.

For a conventional gasoline engine that operates at stoichiometry, the A/F ratio is 14.8. At lower A/F ratios, the engine operates with excess fuel, which results in incomplete combustion. Under these fuel-rich conditions, relatively high concentrations of reducing agents, such as CO and hydrocarbons, are present in the exhaust stream. At A/F ratios above 14.8, the engine operates under fuel-lean conditions where the combustion is more complete due to the presence of excess air. This large quantity of air also lowers the combustion temperature of the engine and reduces the production of

thermal NO_x, which are formed through gas-phase reactions between nitrogen, oxygen, and their radicals according to the Zeldovich mechanism.

Despite significantly lower NO_x emissions, lean-burn engines that operate in highly oxidizing conditions are not currently used since further removal of NO_x from the exhaust gas to meet the emission regulations is difficult as conventional three-way catalysts are ineffective in this environment. The demand for lean-burn engines, however, is projected to increase in the near future as car manufacturers seek to improve the fuel economy and reduce the CO_2 and hydrocarbon emissions from gasoline engines [2]. It is therefore of great importance to develop catalyst technologies that allow for the reduction of NO_x in oxygen-rich environment.

1.2. Catalytic Approaches to NO_x Remediation

Today, there are three main types of catalytic technologies for NO_x removal from the exhaust stream: direct decomposition, selective catalytic reduction, and storage follow by reduction. The nature and applicability of each of these techniques to the reduction of NO_x in the oxygen-rich environment are described below.

1.2.1. Direct Decomposition of NO

In the catalytic decomposition of NO_x that occurs in the absence of reducing agents, NO is directly converted into nitrogen and oxygen according to the reaction:

$$NO \rightarrow \tfrac{1}{2} N_2 + \tfrac{1}{2} O_2 \qquad (1.1)$$

The standard Gibbs free energy change ($\Delta G°_{298K}$) for this reaction is –86 kJ/mol [1], indicating that the NO decomposition is thermodynamically favorable. This reaction however, is never observed in the absence of catalyst because the decomposition of NO is kinetically limited with a high activation energy of 364 kJ/mol [3].

The catalyst that exhibits the greatest activity for direct conversion of NO_x into nitrogen and oxygen is Cu-ZSM-5 [4]. The high activity of this catalyst however is inhibited by the presence of excess oxygen because the active species, Cu^+, is easily oxidized to Cu^{2+} in this environment. The use of Cu-ZSM-5 to decompose NO in lean-burn engines is therefore impractical.

1.2.2. Selective Catalytic Reduction of NO_x

In the selective catalytic reduction (SCR) of NO_x in excess oxygen, the reactions between NO_x and various reducing agents lead to the reduction of NO_x together with the deep oxidation of reductants. These reactions in principle could proceed with stoichiometric amounts of NO_x and reducing agents to produce nitrogen and various combustion products. In practice, however, excess amounts of reducing agents are necessary because the SCR of NO_x is in competition with the direct oxidation of reductants by oxygen. This problem can be overcome with the use of reductants that are selective towards reaction with NO instead of oxygen. These selective reducing agents include ammonia, methane, and other hydrocarbons. The SCR processes by the reductants typically found in the engine exhaust are described below.

1.2.2.1. Carbon Monoxide as Reducing Agent

The SCR of NO_x by carbon monoxide as part of the three-way catalysis process has been the industrial standard for the treatment of emissions from gasoline engines for two decades. In this process, most of the NO_x, CO and hydrocarbons are simultaneously removed from the exhaust by the three-way catalyst, provided that all the oxidizing and reducing agents are present in stoichiometric amounts. This balance between two types of species is achieved by means of a closed-loop air/fuel recirculation system, which controls the engine A/F ratio at ~ 14.8.

Over the three-way catalyst, NO_x is reduced by CO over noble metals (Pt, Rh and Pd) according to the reaction:

$$2\ NO + 2\ CO \rightarrow N_2 + 2\ CO_2 \qquad (1.2)$$

Since this reaction over the noble metals is ineffective in an oxidizing atmosphere, this technology is unsuitable for NO_x remediation in lean-burn engines.

1.2.2.2. Hydrocarbons as Reducing Agent

The SCR of NO_x with hydrocarbons offers an advantage over the use of other reducing agents such as ammonia or urea because small quantities of hydrocarbons are

always present in the engine exhaust due to incomplete combustion. These hydrocarbons reduce NO_x to nitrogen according to the general reaction:

$$2\ NO + C_xH_y + (x + y/4 - 1)\ O_2 \rightarrow N_2 + x\ CO_2 + y/2\ H_2O \qquad (1.3)$$

Although in principle all hydrocarbons can be used in this reaction, most studies have focused on short-chain alkanes and alkenes that are typically found in the engine exhaust. In general, the reactivities of unsaturated alkenes are higher than those of the saturated alkanes, with propene being the most active reductant. This reaction of propene with NO_x proceeds over many forms of catalysts according to:

$$2\ NO + C_3H_6 + 7/2\ O_2 \rightarrow N_2 + 3\ CO_2 + 3\ H_2O \qquad (1.4)$$

Since the discovery of this SCR reaction over Cu-ZSM-5 [5,6], the reduction of NO_x by propene and other hydrocarbons over many ion-exchanged zeolites, especially Cu-ZSM-5 and Co-ZSM-5, has been investigated [7]. The results of these numerous studies conclude that even though many zeolite-based catalysts are active for the SCR of NO with hydrocarbons in the presence of excess oxygen, zeolites are not suitable for automotive application because of the inherent limitation in their hydrothermal stability. Due to this problem, the use of metal oxide-based catalysts for SCR of NO has drawn a great deal of interest in recent years [8,9]. This is the subject of the investigation in Chapter 2 of this thesis.

1.2.3. NO_x Storage-Reduction

In the NO_x storage-reduction (NSR) process, many of the difficulties that are associated with the direct reduction of NO_x in the oxidizing atmosphere are avoided since the only function of the "catalyst" is to store all the NO_x in the form of metal nitrates, instead of reducing them to nitrogen [10,11]. When the engine is temporarily switched to fuel-rich operation, NO_x is released and the sorbent is regenerated. This NO_x is reduced to nitrogen over a conventional three-way catalyst before the engine resumes its normal lean-burn operation. This adsorption and desorption of NO_x take place over the NSR systems according to the reactions:

$$2\ NO + O_2 \rightarrow 2\ NO_2 \qquad (1.5)$$

$$4\ NO_2 + O_2 + 2\ MO\ (s) \rightarrow 2\ M(NO_3)_2\ (s) \qquad (1.6)$$

$$2\ M(NO_3)_2\ (s) \rightarrow 2\ MO\ (s) + 4\ NO_2 + O_2 \qquad (1.7)$$

The metal oxides that are used as the NO_x storage components for the NSR systems are typically alkaline or alkaline earth oxides to provide high NO_x storage capacity. These basic oxides, such as BaO, are easily poisoned by SO_2 in the exhaust, which reacts with the oxides to form sulfites that are later oxidized into sulfates. As these sulfates are extremely stable and difficult to decompose, their accumulation leads to the gradual deactivation of the NSR catalyst [12,13]. This sorbent deactivation problem has to be addressed to allow the commercialization of the NSR technology in countries that use fuels with relatively high sulfur contents. The solution may involve a regenerable SO_x trap to capture all the SO_2 upstream of the NSR catalyst, or a NO_x storage system that is highly tolerant towards SO_2 poisoning. These approaches are investigated in Chapters 3 and 4 of this thesis.

1.3. Research Goals and Directions

The goal of this research is to develop catalytic technologies that are suitable for the removal of NO_x from the exhaust of lean-burn engines. These technologies consist of three series of novel metal oxide nanocomposites that serve as catalysts for the SCR of NO_x with propene, sorbents for SO_2 storage, and catalysts for the NSR system. The composition of each type of nanocomposite is tailored towards the specific requirements of the tasks, as described in the following sections.

1.3.1. SCR of NO_x with Propene

Currently, the most active metal oxide catalysts for the SCR of NO_x by hydrocarbons in the presence of excess oxygen are neither active nor stable enough to be employed in commercial automotive applications. We therefore focus our attention on the development of novel supported metal oxide catalysts with both high SCR activity and good hydrothermal stability.

Early studies on the use of metal oxides for the SCR of NO_x have focused on simple bulk oxides, such as alumina, silica, titania and zirconia. Of these four high surface area oxides, alumina is the most active with 32% NO conversion at 300°C [14]. Since alumina has been used successfully as a support for the three-way catalyst, the

resistance of alumina against deactivation by both water and SO_2 is well established. Alumina is therefore chosen as the support for our SCR catalysts.

To enhance the SCR activity of alumina, various metal oxides are loaded onto this support material. The effects of these metal oxides on the SCR activity of the alumina-supported catalysts are analyzed according to two criteria. The first is the activity of the catalyst, which measures the fractional conversion of NO to N_2. The second is the selectivity of the catalyst, which measures its ability to preferentially react hydrocarbons with NO_x rather than with O_2. Both properties are important to the overall performance of the SCR catalysts as the concentration of hydrocarbons in the exhaust is very limited.

To create the ideal materials that are both active and selective, various alumina-supported metal oxide catalysts are explored for the SCR of NO_x by propene. Although the mechanism of this reaction is still unclear, the results of many studies on surface kinetics have emphasized the roles of both adsorbed nitrates and oxygenated hydrocarbons as potential intermediates in the reduction of NO_x over many catalysts [15-19]. A good catalyst must therefore be able to both adsorb NO_x on its surface and activate the propene molecule to make it reactive towards other species. Both properties must be effective over the same range of temperatures. Various alumina-supported metal oxide nanocomposites are examined as SCR catalysts in Chapter 2.

1.3.2. Reversible SO_2 Storage

One possible solution to the SO_2 deactivation of the NO_x storage component is to employ a SO_x trap to capture all the SO_2 upstream of the NSR catalyst in the oxygen-rich environment, and release SO_2 during the fuel-rich condition. We therefore focus our attention on the development of novel supported metal oxide sorbents that have both high SO_2 adsorption capacity and good regeneration efficiency.

Although there are currently very few studies on the use of solid SO_x trap in automotive applications, the absorption of SO_2 by aqueous solutions of lime and limestone has long been the industrial standard for the removal of SO_2 from the flue gas. This liquid-phase absorption process, however, is unsuitable for SO_x removal from the engine exhaust system, which is conventionally designed to accommodate only solid sorbents.

Among the SO_2 sorbents being developed for the simultaneous removal of NO_x and SO_x from the flue gas, CuO/Al_2O_3 is the most promising candidate for automotive applications. The fresh CuO/Al_2O_3 sorbent readily adsorbs SO_2 in the presence of oxygen to form $CuSO_4$ below 500°C, while the aged sorbent can be regenerated at the same temperature in the reducing atmosphere with gases such as hydrogen, methane and carbon monoxide [20-24]. The low-temperature regeneration of the aged CuO/Al_2O_3, however, is too slow for practical applications of the SO_x trap, which operates in an exhaust stream that is limited in both the concentration of reducing agents and the duration of the fuel-rich period.

To improve the SO_2 adsorption capacity and the regeneration efficiency of CuO/Al_2O_3, various noble metals are loaded onto the sorbent by wet-impregnation method. The addition of these noble metals is expected to improve the oxidation of SO_2 to SO_3 and increase the rate of SO_x adsorption in the oxygen-rich environment. As noble metals are also known to promote CO adsorption in many catalysts that are used for CO oxidation, the presence of noble metals may also lead to a higher rate of sorbent regeneration under the reducing atmosphere. The effects of noble metal addition on CuO/Al_2O_3-based nanocomposite sorbents are examined in Chapter 3.

1.3.3. Sulfur-Tolerant NSR System

Another approach to minimize the detrimental effects of SO_2 on the performance of the NSR system is to increase the resistance of the NO_x storage component against SO_2 poisoning. This can be achieved by reducing the amount of SO_2 adsorbed under fuel-lean condition, and increasing the rate of SO_2 desorption during the regeneration process. We therefore focus our attention on the development of novel supported metal oxide sorbents that have high NO_x adsorption capacity and SO_2 resistance.

Today, most of the NSR systems with high NO_x adsorption capacity are based on the $Pt/BaO/Al_2O_3$ sorbent that was originally developed by Toyota. The performance of this system, however, quickly deteriorates in the presence of SO_2 due to the formation of extremely stable barium sulfate. To minimize this problem, the NO_x storage component of our NSR system is based on MgO. MgO is chosen because in this least basic oxide, SO_2 adsorption is least favorable and the sulfate is easiest to decompose. Although Mg

sulfate is still significantly more stable than Mg nitrate [25,26], the difference between the adsorption energies of SO_x and NO_x on MgO is the smallest among the alkaline earth oxides [27]. This relatively small preference towards the adsorption of SO_x over NO_x also makes MgO a more suitable NO_x storage component in the presence of SO_2 than other alkaline earth oxides.

To improve the SO_2 regeneration efficiency of the NO_x storage component, MgO is incorporated directly into the CuO-based sorbent that we have developed in Chapter 3 for reversible SO_2 adsorption. This integration of NO_x trap with SO_x trap, however, is expected to improve the SO_2 resistance of the NSR sorbent at the expense of its NO_x storage capacity. This trade-off between the NO_x adsorption and SO_2 desorption properties of the SO_x-tolerant NO_x trap is examined in Chapter 4.

1.4. Nanocomposite Processing

Besides the proper selection of catalyst compositions, the effectiveness of the proposed systems also depends on the synergism between the different functions of the catalysts, and the thermal stability of the supports. These attributes are determined by the loading and dispersion of the active components, as well as the surface area of the support, all of which can be controlled by the synthesis approach and parameters.

To synthesize high surface area material with high loadings and dispersion of the active components for automotive applications, the sequential precipitation technique has been developed in this thesis. In this approach, the basic precipitations of the support and the active components are carried out separately and sequentially, thereby allowing the properties of the support and the active components to be independently tailored through the use of different synthesis conditions. This is accomplished by chemically precipitating a salt solution of the chosen active components onto a suspension of pre-formed hydroxide particles of the support material. With this liquid-phase deposition approach, a large amount of active components can be dispersed onto the support with minimal loss of surface area associated with grain growth and agglomeration. This prevents the decrease in active component dispersion, which is common in the conventional wet-impregnation synthesis, especially at high loadings.

To overcome the problem of poor dispersion, synthesis methods, such as co-precipitation and sol-gel processing, have been developed. These two methods, however, frequently lead to the formation of complex mixed oxide phases during heat treatment. For example, the co-precipitation of Cu and Al salts would cause undesirable $CuAl_2O_4$ formation, which would reduce the SO_2 adsorption capacity in the resulting SO_x trap. The extent of such Cu doping can be reduced when Cu is preferentially deposited on the surface of pre-formed $Al(OH)_3$ particles via the sequential precipitation approach.

In this work, various sequentially precipitated alumina-supported metal oxide nanocomposites are investigated as catalysts for the reduction of NO by propene, sorbents for SO_2 storage, and catalysts for the NSR system. The effects of the preparation method, as well as the amount and composition of active components loaded on the performance of these catalysts are reported in Chapters 2–4.

1.5. References

[1] A. Fritz, V. Pitchon, Appl. Catal. B 13 (1997) 1.

[2] C.J. Pereira, M.D. Amiridis, in: U.S. Ozkan, S.K. Agarwal, G. Marcelin (Eds.), Reduction of Nitrogen Oxide Emissions, ACS Symposium Series 587, American Chemical Society, Washington, D.C., 1995, p. 1.

[3] H. Glick, J.J. Klein, W. Squire, J. Chem. Phys. 27 (1957) 850.

[4] Y. Li, W.K. Hall, J. Phys. Chem. 94 (1990) 6145.

[5] M. Iwamoto, H. Yahiro, Y. Yu-u, S. Shundo, N. Mizuno, Shikubai 32 (1990) 430.

[6] W. Held, A. Koenig, T. Richter, L. Puppe, SAE Paper 900496 (1990).

[7] M. Amiridis, T. Zhang, R.J. Farrauto, Appl. Catal. B 10 (1996) 203.

[8] M.D. Fokema, J.Y. Ying, Catal. Rev. 43 (2001) 1.

[9] R. Burch, J.P. Breen, F.C. Meunier, Appl. Catal. B 39 (2002) 283.

[10] S. Matsumoto, Catal. Today 22 (1994) 12.

[11] W. Bogner, M. Kramer, B. Krutzsch, S. Pischinger, D. Vigtlander, G. Wenninger, F. Wirbeleit, M.S. Brogan, R.J. Brisley, D.E. Webster, Appl. Catal. B 7 (1995) 153.

[12] P. Engstrom, A. Amberntsson, M. Skoglundh, E. Fridell, G. Smedler, Appl. Catal. B 22 (1999) L241.

[13] A. Amberntsson, M. Skoglundh, M. Jonsson, E. Fridell, Catal. Today 73 (2002) 279.

[14] Y. Kintaichi, H. Hamada, M. Tabata, M. Sasaki, T. Ito, Catal. Lett. 6 (1990) 239.

[15] K. Shimizu, H. Kawabata, A. Satsuma, T. Hattori, J. Phys. Chem. B 103 (1999) 5240.

[16] F.C. Meunier, J.P. Breen, V. Zuzaniuk, M. Olsson, J.R.H. Ross, J. Catal. 187 (1999) 493.

[17] Y. Chi, S.S.C. Chuang, J. Catal. 190 (2000) 75.

[18] T. Maunula, J. Ahola, H. Hamada, Appl. Catal. B 26 (2000) 173.

[19] P.W. Park, S.C. Ragle, C.L. Boyer, M.L. Balmer, M. Engelhard, D. McCready, J. Catal. 210 (2002) 97.

[20] S.G. Deng, Y.S. Lin, Ind. Eng. Chem. Res. 35 (1996) 1429.

[21] K.S. Yoo, S.M. Jeong, S.D. Kim, S.B. Park, Ind. Eng. Chem. Res. 35 (1996) 1543.

[22] S.M. Jeong, S.D. Kim, Ind. Eng. Chem. Res. 36 (1997) 5425.

[23] C. Macken, B.K. Hodnett, Ind. Eng. Chem. Res. 37 (1998) 2611.

[24] C. Macken, G. Paparatto, B.K. Hodnett, Ind. Eng. Chem. Res. 39 (2000) 3868.

[25] J.A. Rodriguez, T. Jirsak, A. Freitag, J.Z. Larese, A. Maiti, J. Phys. Chem. B 104 (2000) 7439.

[26] W.F. Schneider, J. Li, K.C. Hass, J. Phys. Chem. B 105 (2001) 6972.

[27] W.F. Schneider, J. Phys. Chem. B 108 (2004) 273.

Chapter 2 – Metal Oxide Nanocomposites for SCR of NO_x by Propene

2.1. Introduction

Due to increasingly stringent government regulations on vehicle nitrogen oxides (NO_x) emission levels [1], the selective catalytic reduction (SCR) of NO_x to N_2 by hydrocarbons has gained a great deal of attention. In particular, the removal of NO_x from lean-burn and diesel engines operating under an oxygen-rich atmosphere presents significant challenges since conventional three-way catalysts are ineffective in this environment [2-4]. Moreover, the presence of water vapor and sulfur oxides (SO_x) in the exhaust stream both inhibits catalyst activity and results in long-term catalyst instability [5]. Therefore, it is necessary to develop catalyst that is both active and stable under actual exhaust conditions.

Since the first independent reports by Held *et al.* [6] and Iwamoto *et al.* [7] show that Cu-ZSM-5 catalyzes the SCR of NO_x by hydrocarbons, numerous catalysts, ranging from zeolites to supported noble metals and metal oxides, have been extensively investigated. In particular, metal oxides supported on alumina show the most promise for practical applications due to alumina's superior hydrothermal stability to zeolites. The effectiveness of this type of catalysts for NO_x reduction depends strongly on the nature and the dispersion of metal additives, which in turn are controlled by the catalyst loading and catalyst preparation technique, as evident in the studies on Sn/Al_2O_3 [8], Co/Al_2O_3 [9], Ag/Al_2O_3 [10,11], and Ga/Al_2O_3 [12,13]. Although the mechanism of this reaction is not fully understood, recent studies have emphasized the role of adsorbed nitrates and oxygenated hydrocarbons as intermediates in the SCR of NO_x by propene [14-18]. It appears that for a catalyst to be effective, it must be able to activate the propene molecule as well as adsorb NO_x on its surface at the temperatures of interest.

This chapter examines the synthesis and characterization of various metal oxides supported on alumina for the reduction of NO by propene. The effects of the catalyst preparation method as well as the amount and composition of the metals loaded on the performance of these catalysts are evaluated according to their activity and selectivity. The latter indicates the efficiency of a catalyst in utilizing the available propene to react

with NO instead of oxygen, and is given by the ratio of propene that reacts with NO to total propene conversion:

$$\text{Selectivity}(\%) = \frac{2[N_2]}{3[CO_2]+2[CO]} \times 100 \qquad (2.1)$$

From the broad range of Al_2O_3-supported catalysts that we have screened, which includes transition metals (Co, Cu, Zn, Ag) as well as main group elements (Ga, In, Sn), Ga_2O_3/Al_2O_3 exhibits the highest selectivity and the best NO reduction activity. This is in agreement with the finding of Maunula *et al.* [19], and Miyadera and Yoshida [20].

2.2. Experimental

2.2.1. Catalyst Preparation

To achieve high surface area materials with good dispersion of active components, Al_2O_3-based nanocomposite catalysts were prepared using a sequential chemical precipitation technique. In this synthesis, an aqueous solution of aluminum nitrate was first added to a solution of tetraethylammonium hydroxide to yield an aluminum hydroxide precipitate. After aging for 24 hours, a metal salt solution of the active component(s) was then added. Metal nitrates were used as precursors, except in the case of tin, where tin chloride was employed. The suspension was stirred for 24 hours, and the resulting "coated" catalysts were centrifuged, washed and dried, before calcination in air at 700°C for 3 hours.

To study the effects of synthesis methods, catalysts were also prepared by impregnation and sol-gel methods. "Impregnated" catalysts were prepared by impregnating the pre-calcined alumina support with an aqueous solution of metal nitrate(s) or chloride(s). "Mixed oxide" catalysts were synthesized by the sol-gel method by addition of metal precursors pre-dissolved in ethylene glycol to the boehmite sol prepared according to the procedure of Maeda *et al.* [21]. The loadings of all the catalysts in this work were reported in wt% metal.

2.2.2. Catalyst Characterization

Catalyst surface area and pore size distribution were calculated from the nitrogen adsorption isotherm (Micromeritics ASAP 2000) using the BET and BJH methods, respectively. Phase identification was achieved by X-ray diffraction (XRD) with a Siemens D5000 diffractometer using Cu Kα radiation at 45 kV and 40 mA. Scherrer's analysis of X-ray peak broadening was employed to determine crystallite size. Particle morphology was studied using transmission electron microscopy (TEM) performed on a JEOL 2010 high-resolution microscope. Elemental mapping was collected using a VG HB603 scanning transmission electron microscope (STEM) equipped with energy dispersive X-ray (EDX) analysis. Elemental analysis was performed by inductively coupled plasma (ICP) at Desert Analytics (Tucson, AZ).

2.2.3. Catalytic Reactions

Catalytic activities under steady-state conditions were measured in a quartz tube fixed-bed reactor. A feed gas mixture that contained 0.1% NO, 0.1% C_3H_6, 15% O_2, and 0% or 10% H_2O with He as a balance was fed to 0.2 g of catalyst at a total flow rate of 200 cm^3/min, which corresponded to a contact time of 0.06 g·s/cm^3 or a space velocity of ~ 30,000 h^{-1}. Water was introduced into the gas stream through a syringe pump with the He flow rate adjusted to keep the concentrations of the other gas components constant. The reactor effluent was analyzed with a HP 6890 Plus gas chromatograph equipped with a washed molesieve 13X column and a Porapak Q column. This allowed oxygen, nitrogen, nitrous oxide, carbon monoxide, carbon dioxide, water and propene to be separated and quantified. No N_2O was detected in our catalytic studies.

2.2.4. Temperature-Programmed Desorption (TPD)

Prior to each NO_x TPD experiment, 0.2 g of catalyst sample was purged in a flow of 15% O_2 in He at 200 cm^3/min at 600°C for 2 hours. Following cooling to 50°C, NO_x adsorption was performed by exposing the sample to 0.1% NO and 15% O_2 in He at 200 cm^3/min for 2 hours. Desorption of adsorbed species was performed at a ramp rate of 2°C/min in a He flow of 60 cm^3/min with 0.5% Ar as internal standard; the effluent was

analyzed using a HP 6890 Plus gas chromatograph equipped with a HP 5972A Mass Selective Detector.

2.3. Results and Discussion

2.3.1. Effect of Gallium Loading

The effects of Ga addition on the catalytic activities of Ga_2O_3/Al_2O_3 catalysts synthesized by the sol-gel method in the absence of water are shown in Figure 2.1. Small addition of Ga_2O_3 led to enhancements in propene conversion and catalyst selectivity. However, as the Ga loading was further increased, additional propene conversion was achieved at the expense of selectivity. The optimal performance was attained at 40 wt% Ga loading. Our results were in good agreement with that reported by Haneda *et al.* [22] in that the existence of composite oxide of Ga and Al appeared to be essential for high catalytic activity.

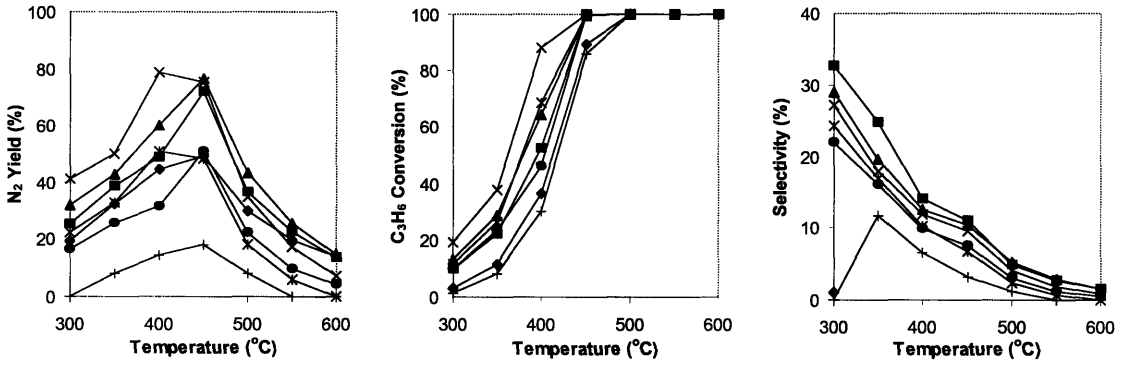

Figure 2.1. N_2 yield, propene conversion and selectivity for NO reduction by propene over sol-gel derived Ga_2O_3/Al_2O_3 catalysts with (♦) 0 wt%, (■) 20 wt%, (▲) 30 wt%, (×) 40 wt%, (*) 50 wt%, (●) 60 wt% and (+) 100 wt% Ga. The reactions were run at a space velocity of 30,000 h^{-1} with 0.1% NO, 0.1% C_3H_6, and 15% O_2.

2.3.2. Effect of Preparation Method

To study the effect of synthesis technique, Ga_2O_3/Al_2O_3 catalysts with various Ga loadings were prepared using the wet-impregnation method (I), sol-gel processing (S), and the sequential precipitation or "coating" method (C). The optimal activities of the Ga_2O_3/Al_2O_3 catalysts prepared by the different synthesis methods are shown in Figure

2.2. The Ga_2O_3/Al_2O_3 (S) and Ga_2O_3/Al_2O_3 (C) catalysts displayed high N_2 yields of 80% in the absence of water; they were superior to the Ga_2O_3/Al_2O_3 (I) catalyst. The origins of their high NO yields, however, were quite different. The optimal Ga_2O_3/Al_2O_3 (S) showed a greater propene conversion, which could be associated with its high Ga loading (40 wt%). The optimal Ga_2O_3/Al_2O_3 (C) has a lower Ga loading of 10 wt%, and its high yield was associated with a high selectivity.

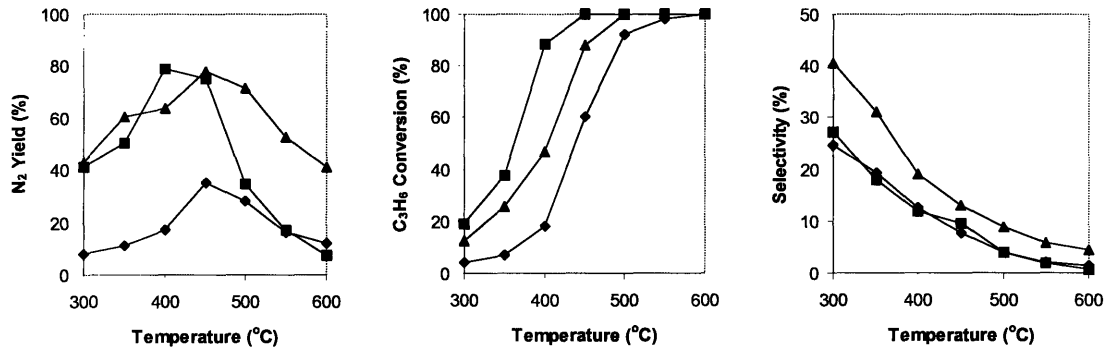

Figure 2.2. N_2 yield, propene conversion and selectivity for NO reduction by propene over the optimal (♦) Ga_2O_3/Al_2O_3 (I) catalyst (8 wt% Ga), (■) Ga_2O_3/Al_2O_3 (S) catalyst (40 wt% Ga) and (▲) Ga_2O_3/Al_2O_3 (C) catalyst (10 wt% Ga). The reactions were run at a space velocity of 30,000 h^{-1} with 0.1% NO, 0.1% C_3H_6, and 15% O_2.

Unlike the optimal Ga_2O_3/Al_2O_3 (I) catalyst, the optimal Ga_2O_3/Al_2O_3 (S) and Ga_2O_3/Al_2O_3 (C) catalysts showed no distinct XRD peaks associated with the Ga_2O_3 phase (see Figure 2.3). This indicated that the Ga species were well dispersed over the latter two catalysts, which exhibited high NO reduction activities. This was consistent with the XANES and EXAFS findings of Shimizu *et al.* [12], which concluded that Ga atoms located at the tetrahedrally coordinated surface cation sites in the form of highly dispersed GaO_4 were responsible for the high activity of Ga_2O_3/Al_2O_3 catalyst. As Ga_2O_3 content increased, the fraction of tetrahedral Ga species would decrease, which could explain the reduction in selectivity of catalysts with high Ga loadings.

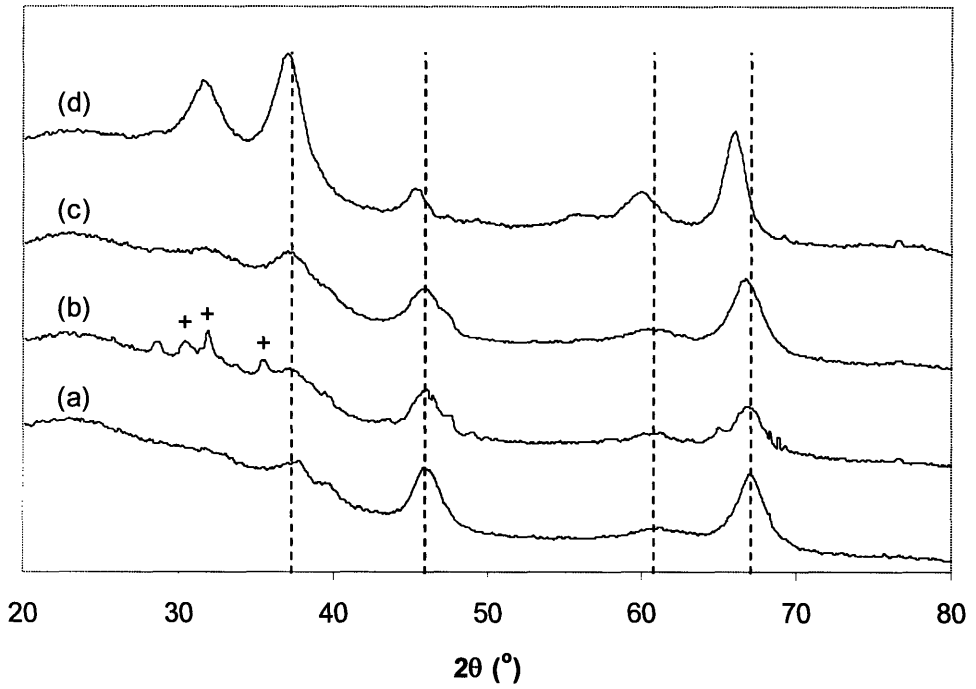

Figure 2.3. XRD patterns of (a) γ-Al_2O_3, and the optimal (b) Ga_2O_3/Al_2O_3 (I) catalyst, (c) Ga_2O_3/Al_2O_3 (C) catalyst and (d) Ga_2O_3/Al_2O_3 (S) catalyst. Phases present included (I) γ-Al_2O_3 and (+) Ga_2O_3.

The main difference between the sol-gel synthesis and the sequential precipitation technique was that the latter preferentially deposited Ga around the pre-formed $Al(OH)_3$ particles instead of incorporating Ga into the Al_2O_3 lattice to form Ga-O-Al bonds during the gelation process. Upon calcination, a larger fraction of Ga would be doped within the Al_2O_3 lattice in the sol-gel derived material, leading to the less effective usage of Ga. The presence of this Ga doping caused the significant shift in the γ-Al_2O_3 XRD peaks in Ga_2O_3/Al_2O_3 (S) (see Figure 2.3(d)).

Table 2.1 shows that the surface area and pore volume of Ga_2O_3/Al_2O_3 (I) were lower than that of γ-Al_2O_3 due to blockage of the support's pores by the impregnated Ga_2O_3. Significant incorporation of Ga into the γ-Al_2O_3 lattice led to the low surface area of 140 m^2/g in Ga_2O_3/Al_2O_3 (S). In contrast, Ga_2O_3/Al_2O_3 (C) possessed a higher surface area and pore volume than γ-Al_2O_3, probably because its highly dispersed Ga_2O_3 coating reduced the agglomeration and grain growth of the γ-Al_2O_3 support during calcination.

These results indicated that the sequential precipitation route could be used to prepare catalysts with high Ga_2O_3 dispersion and excellent surface area.

Table 2.1. BET surface area, pore volume and average pore diameter of γ-Al_2O_3 and the optimal Ga_2O_3/Al_2O_3 catalysts prepared by different methods.

Catalyst	Ga Loading (wt%)	Surface Area (m^2/g)	Pore Volume (cm^3/g)	Pore Diameter (nm)
Al_2O_3	–	200	0.50	7.2
Ga_2O_3/Al_2O_3 (I)	8	153	0.40	8.4
Ga_2O_3/Al_2O_3 (S)	40	140	0.51	11.4
Ga_2O_3/Al_2O_3 (C)	10	210	0.62	8.8

2.3.3. Metal Oxide-Coated Al_2O_3 Nanocomposites

Of all the metal oxide-coated catalysts examined, Ga_2O_3/Al_2O_3 with 10 wt% Ga exhibited the best N_2 yield of ~ 80% in the absence of water at 450°C. However, the activity of this catalyst was lowered to 60% when 10% water was introduced into the feed stream. Such inhibition effect could be attributed to the competitive adsorption between water and one or more of the reactants [4]. Figure 2.4 illustrates that the presence of water caused a significant decrease in propene conversion along with an increase in selectivity, suggesting that the amount of propene on the surface was reduced.

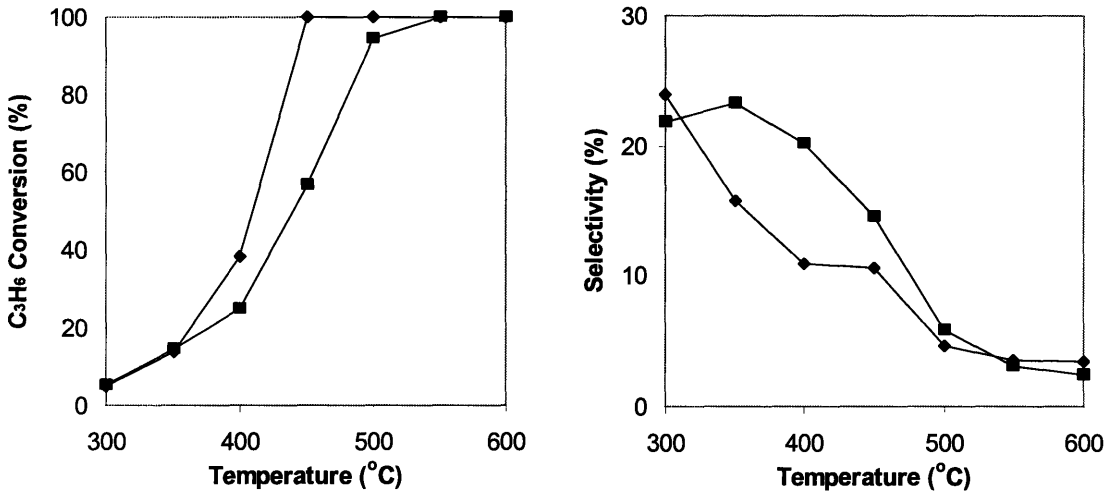

Figure 2.4. Propene conversion and selectivity for NO reduction by propene over Ga_2O_3/Al_2O_3 (C) catalyst with 10 wt% Ga. The reactions were run at a space velocity of 30,000 h^{-1} with 0.1% NO, 0.1% C_3H_6, 15% O_2, and (♦) 0% or (■) 10% H_2O.

Table 2.2 shows that pure Al_2O_3 has a higher selectivity for NO reduction by propene than Ga_2O_3/Al_2O_3 (C) and In_2O_3/Al_2O_3 (C). However, the introduction of Ga_2O_3 coating improved the yield of Al_2O_3 by enhancing the propene conversion, without much compromise in catalytic selectivity. In contrast, SnO_2- and In_2O_3-coated Al_2O_3 displayed high N_2 yields due to high propene conversions despite their relatively low selectivities. Recent studies have proposed that the role of SnO_2/Al_2O_3 and In_2O_3/Al_2O_3 in the SCR of NO was to selectively oxidize propene to acrolein, which further reacted on Al_2O_3 to form nitrogen [18,23,24].

Table 2.2. Catalytic activities of pure γ-Al_2O_3 and metal oxide-coated Al_2O_3 catalysts with 10 wt% metal loadings.[a]

Catalyst	C_3H_6 conversion (%)	Selectivity (%)	N_2 Yield (%)
Al_2O_3	51	15.0	49
Ga_2O_3/Al_2O_3	57	14.5	60
SnO_2/Al_2O_3	77	8.3	42
In_2O_3/Al_2O_3	83	8.2	59

[a] The reactions were run at a space velocity of 30,000 h^{-1} at 450°C with 0.1% NO, 0.1% C_3H_6, 15% O_2, and 10% H_2O.

To take advantage of the good propene selectivity offered by Ga_2O_3/Al_2O_3 and the high propene conversions associated with SnO_2/Al_2O_3 and In_2O_3/Al_2O_3, various Al_2O_3-based nanocomposites with Ga and Sn or In were synthesized with a total metal loading of 10 wt%. Figure 2.5 compares the catalytic activities of the Al_2O_3-based nanocomposites containing 10 wt% Ga, 4 wt% Sn and 6 wt% Ga, and 4 wt% In and 6 wt% Ga. It illustrates that the introduction of Sn and In in addition to Ga led to improvements in propene conversion in the presence of water, giving rise to greater N_2 yield. In particular, a combination of 4 wt% In and 6 wt% Ga led to an excellent yield of 80% at 450°C. Improvement in NO activity by addition of In_2O_3 and SnO_2 had also been reported by Haneda *et al.* in their studies on the effect of additives on the performance of sol-gel derived Ga_2O_3-Al_2O_3 [25]. In our case, the metal oxide-coated Al_2O_3 nanocomposites containing 10 wt% Ga, 4 wt% Sn and 6 wt% Ga, and 4 wt% In and 6 wt% Ga gave rise to selectivities of 14.5%, 13.5%, and 10.7%, respectively. Thus, the sequential precipitation approach provided for excellent synergism between the active components coated, so that substantial increase in propene conversions were realized without significant reduction in selectivities for the latter two catalysts.

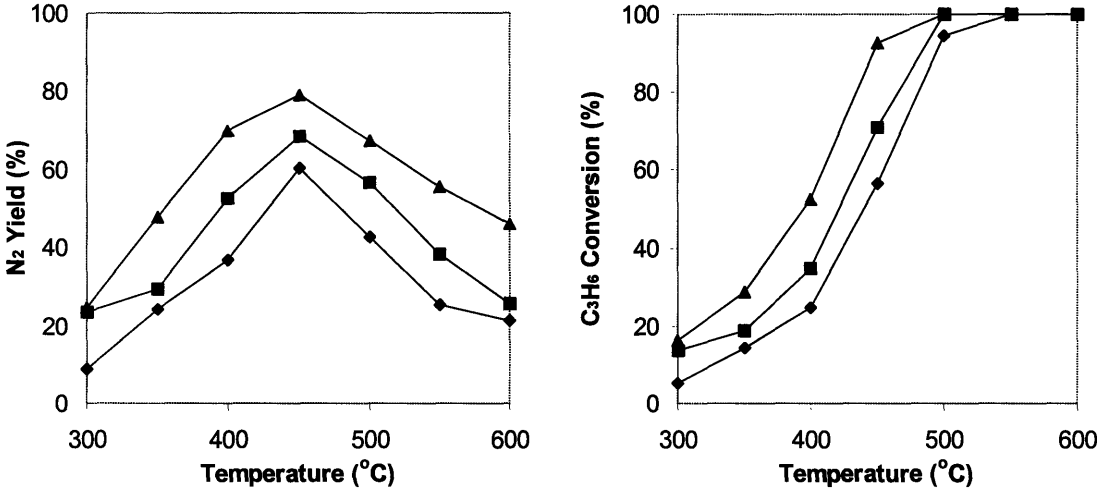

Figure 2.5. N_2 yield and propene conversion for NO reduction by propene over metal oxide-coated Al_2O_3 nanocomposites containing (♦) 10 wt% Ga, (■) 4 wt% Sn and 6 wt% Ga, and (▲) 4 wt% In and 6 wt% Ga. The reactions were run at a space velocity of 30,000 h^{-1} with 0.1% NO, 0.1% C_3H_6, 15% O_2, and 10% H_2O.

2.3.4. In_2O_3-Ga_2O_3/Al_2O_3 Nanocomposites

2.3.4.1. Catalyst Characterization

To optimize the characteristics of In_2O_3-Ga_2O_3/Al_2O_3 nanocomposite catalysts, various combinations of In and Ga loadings were prepared with a fixed total metal loading of 10 wt%. The XRD patterns of the In_2O_3-Ga_2O_3/Al_2O_3 nanocomposites are shown in Figure 2.6. At 10 wt% Ga loading, the only crystalline phase observed in the XRD pattern was that of γ-Al_2O_3. With the introduction of In, the high Ga dispersion over γ-Al_2O_3 was maintained. The In_2O_3 diffraction peaks were only detected at high In loadings of $\geq$ 8 wt%.

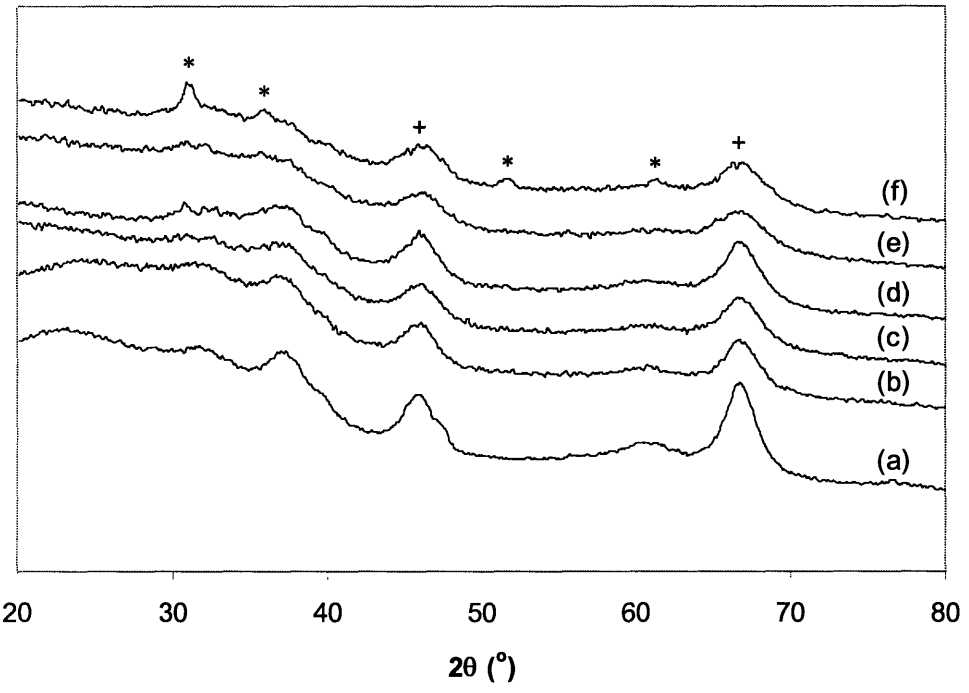

Figure 2.6. XRD patterns of In_2O_3-Ga_2O_3/Al_2O_3 nanocomposites containing a total metal loading of 10 wt%, with (a) 0 wt%, (b) 2 wt%, (c) 4 wt%, (d) 6 wt%, (e) 8 wt% and (f) 10 wt% In. Phases present included (+) γ-Al_2O_3 and (*) In_2O_3.

TEM micrograph of the In_2O_3-Ga_2O_3/Al_2O_3 nanocomposite with 2 wt% In and 8 wt% Ga shows that the catalyst was composed of ~ 5-nm crystallites loosely agglomerated into larger secondary particles (Figure 2.7(a)). High-resolution TEM micrograph (Figure 2.7(b)) illustrates that the crystallites have lattice fringes of ~ 0.19

nm in spacing, corresponding to the (400) plane of γ-Al_2O_3. The 5-nm Al_2O_3 crystallite size noted in Figure 2.7 was in good agreement with that obtained by Scherrer's analysis of the γ-Al_2O_3 XRD peaks in Figure 2.6(b). These crystallites were surrounded by amorphous coatings. No Ga_2O_3 or In_2O_3 crystallites were observed by TEM, while the STEM elemental mapping clearly indicated the presence of highly dispersed Ga and In species (Figure 2.8). The Ga and In contents in the nanocomposites were verified by EDX and ICP elemental analysis to be consistent with that used in catalyst preparation.

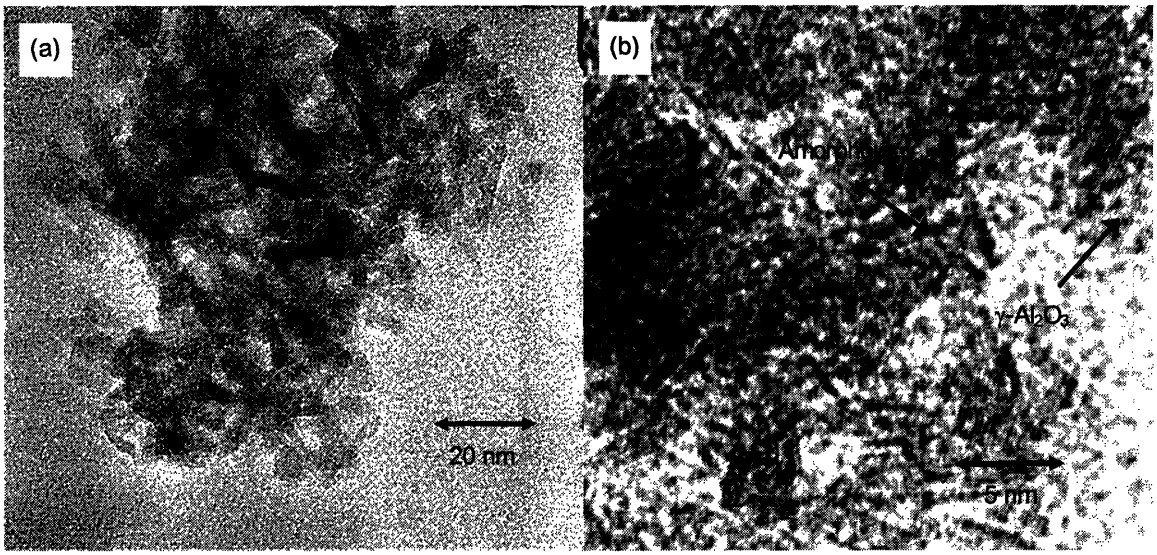

Figure 2.7. (a) TEM and (b) high-resolution TEM micrographs of In_2O_3-Ga_2O_3/Al_2O_3 nanocomposite with 2 wt% In and 8 wt% Ga.

Table 2.3 shows that the BET surface area, pore volume and average pore size of the In_2O_3-Ga_2O_3/Al_2O_3 nanocomposite increased with In loading. By preferentially coating In_2O_3 and Ga_2O_3 around the Al_2O_3 particles, catalysts with higher surface area than pure Al_2O_3 could be synthesized. The metal oxide coating could have acted as a diffusion barrier that prevented the grain growth and agglomeration of Al_2O_3 particles during calcination. With the addition of In, the transformation to the high-temperature α-Al_2O_3 phase was also suppressed upon calcination to 1100°C (see Figure 2.9), indicating that the presence of In enhanced the thermal stability of the nanocomposite catalyst.

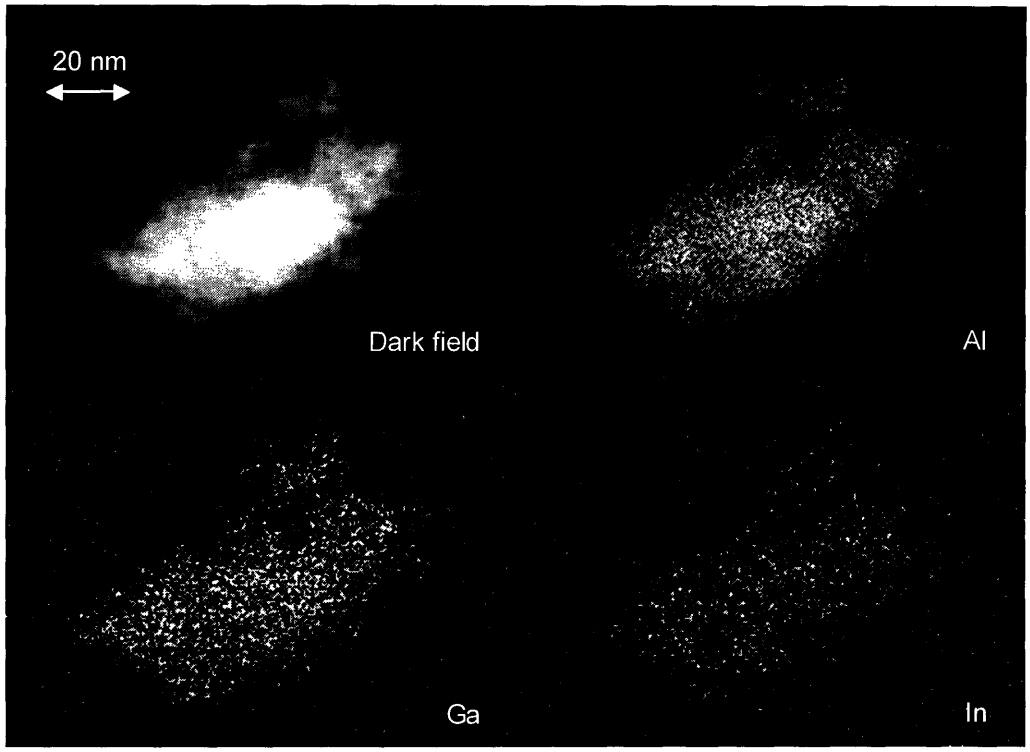

Figure 2.8. STEM image and elemental maps of In_2O_3-Ga_2O_3/Al_2O_3 nanocomposite with 2 wt% In and 8 wt% Ga.

Table 2.3. BET surface area, pore volume and average pore diameter of In_2O_3-Ga_2O_3/Al_2O_3 nanocomposites.

Ga loading (wt%)	In Loading (wt%)	Surface Area (m^2/g)	Pore Volume (cm^3/g)	Pore Diameter (nm)
10	0	210	0.62	8.8
8	2	223	0.84	10.8
6	4	243	0.98	11.8
4	6	285	1.05	10.8
2	8	312	1.22	12.0
0	10	298	1.15	12.6

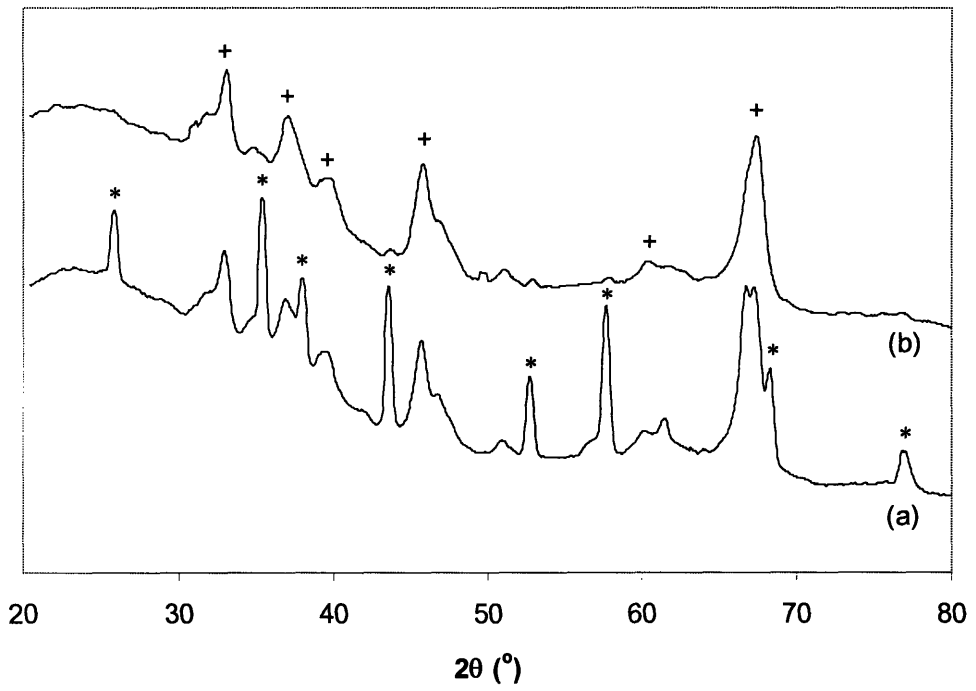

Figure 2.9. XRD patterns of 1100°C-calcined In_2O_3-Ga_2O_3/Al_2O_3 nanocomposites with (a) 10 wt% Ga, and (b) 2 wt% In and 8 wt% Ga. Phases present included (+) θ-Al_2O_3 and (*) α-Al_2O_3.

2.3.4.2. SCR of NO by Propene

To optimize the catalytic activities of In_2O_3-Ga_2O_3/Al_2O_3 nanocomposites, various combinations of In and Ga loadings were examined, while keeping the total metal loading constant at 10 wt%. Figure 2.10 shows that the propene conversion increased dramatically even with the introduction of only 2 wt% In. This gave rise to a reduction in the propene light-off temperature by 50°C, relative to that of the Ga_2O_3/Al_2O_3. Full conversion was achieved at 500°C for the nanocomposite containing 2 wt% In and 8 wt% Ga. Selectivity was found to gradually decrease with increasing In loading. Thus, the optimal yield was obtained with the nanocomposite catalysts with 2-4 wt% In and 8-6 wt% Ga. At 450°C, these optimal catalysts converted over 80% of NO to N_2, representing the most active catalysts reported for the SCR of NO by propene under high partial pressures of water and oxygen at a high space velocity.

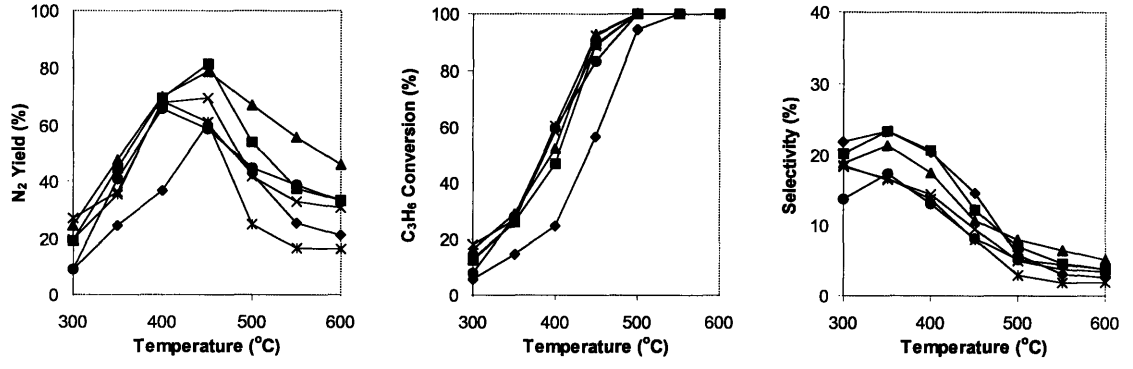

Figure 2.10. N_2 yield, propene conversion and selectivity for NO reduction by propene over In_2O_3-Ga_2O_3/Al_2O_3 nanocomposites containing a total metal loading of 10 wt%, with (♦) 0 wt%, (■) 2 wt%, (▲) 4 wt%, (×) 6 wt%, (*) 8 wt% and (●) 10 wt% In. The reactions were run at a space velocity of 30,000 h^{-1} with 0.1% NO, 0.1% C_3H_6, 15% O_2, and 10% H_2O.

Although the N_2 yield of the In_2O_3-Ga_2O_3/Al_2O_3 nanocomposite with 2 wt% In and 8 wt% Ga decreased with increasing space velocity, the catalyst still maintained relatively high N_2 yields of 68% and 43% at 450°C at space velocities of 60,000 h^{-1} and 120,000 h^{-1}, respectively (Figure 2.11). Since this decrease in catalytic yield was mainly caused by lower propene conversion, the effect was much more pronounced at low temperatures where incomplete propene conversion was observed. Since the selectivity of the catalyst was not significantly affected by space velocity, the decrease in catalytic yield at high space velocities could be overcome by the use of a larger quantity of catalyst. Large changes in the space velocity, nevertheless, could bring about significant changes in the conversions of both NO and propene, which would ultimately affect the selectivity (see Figure 2.12). At low space velocity where propene conversion and N_2 yield were high, the selectivity of the catalyst was low since the quantities of both propene and NO that were available for reaction were very small relative to O_2.

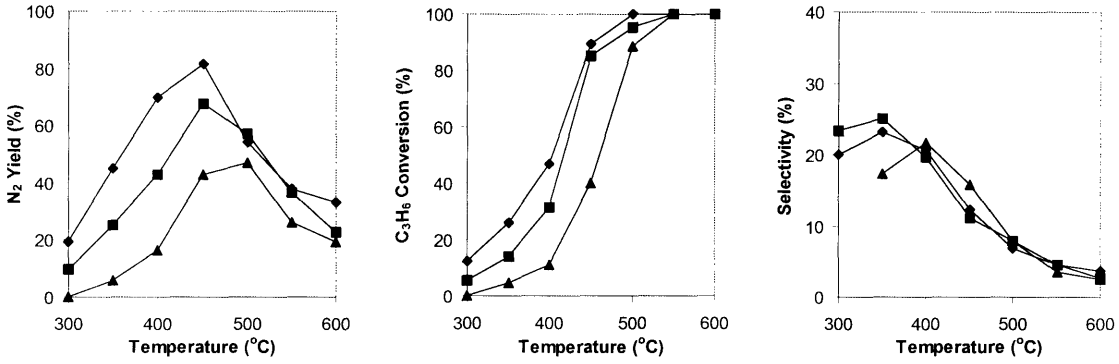

Figure 2.11. Effect of space velocity on the N_2 yield, propene conversion and selectivity for NO reduction by propene over the In_2O_3-Ga_2O_3/Al_2O_3 nanocomposite with 2 wt% In and 8 wt% Ga. The reactions were run at a space velocity of (♦) 30,000 h^{-1}, (■) 60,000 h^{-1}, and (▲) 120,000 h^{-1} with 0.1% NO, 0.1% C_3H_6, 15% O_2, and 10% H_2O.

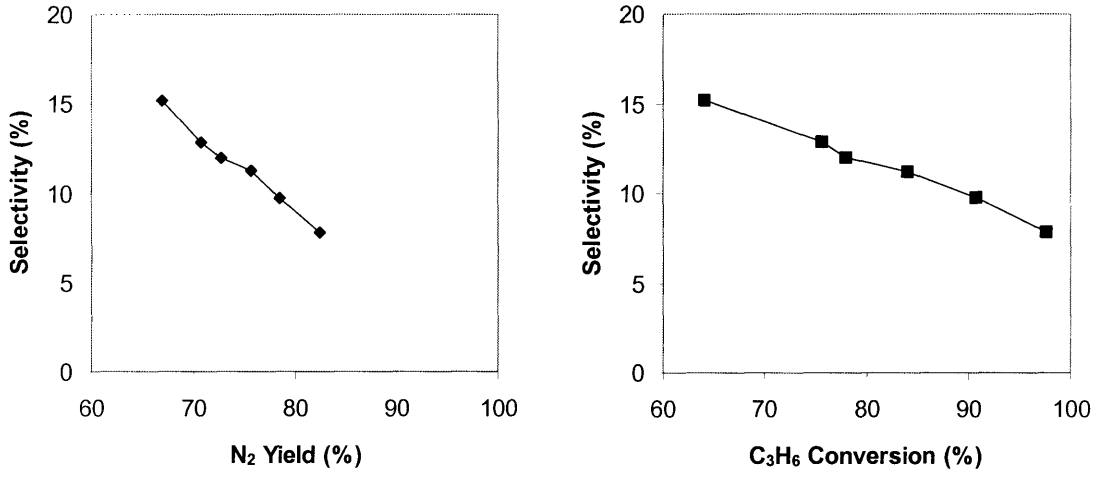

Figure 2.12. Selectivity vs. N_2 yield and propene conversion for NO reduction by propene over the In_2O_3-Ga_2O_3/Al_2O_3 nanocomposite with 2 wt% In and 8 wt% Ga. The reactions were run at space velocities of 12,000–96,000 h^{-1} with 0.1% NO, 0.1% C_3H_6, 15% O_2, and 10% H_2O at 450°C.

2.3.4.3. Effect of Oxygen Concentration

Since the SCR activities of the In_2O_3-Ga_2O_3/Al_2O_3 nanocomposites were dictated by their propene conversion and selectivity, the amount of oxygen present in the feed was expected to play an important role. Figure 2.13 shows that as the oxygen in the feed stream was increased from 3 to 20 mol%, the propene conversion was increased at the

expense of selectivity because there was more oxygen to compete with NO for reaction with propene. A N_2 yield of > 90% was observed with an optimal O_2 feed concentration of 5 mol%. The presence of a small amount of oxygen was necessary to maintain the good SCR performance of the catalyst because it helped to convert propene into the partially oxidized hydrocarbon intermediate. Even though 40% of propene could be converted by the catalyst in the absence of O_2, this propene conversion was largely a result of propene decomposition as indicated by the preferential production of CH_4 over CO and CO_2. The formation of N_2 in such case was therefore attributed to the direct decomposition of NO into N_2 and O_2 [2,3].

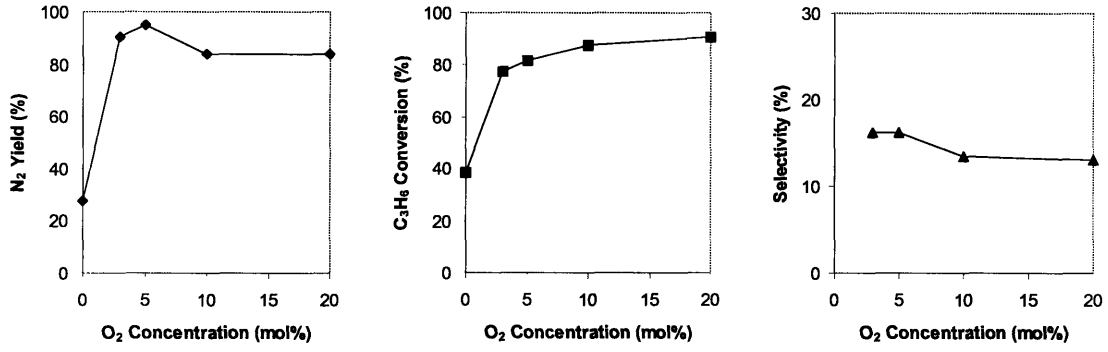

Figure 2.13. Effect of oxygen concentration on the N_2 yield, propene conversion and selectivity for NO reduction by propene over the In_2O_3-Ga_2O_3/Al_2O_3 nanocomposite with 2 wt% In and 8 wt% Ga. The reactions were run at a space velocity of 30,000 h^{-1} with 0.1% NO, 0.1% C_3H_6, 3–20% O_2, and 10% H_2O at 450°C.

2.3.4.4. Effect of Water Vapor

Figure 2.14 shows that increasing water content in the feed stream led to a reduction in propene conversion over the In_2O_3-Ga_2O_3/Al_2O_3 nanocomposite, although this inhibitory effect was much smaller than that found over Ga_2O_3/Al_2O_3. As the selectivity of the nanocomposite catalyst above 400°C was improved with the addition of water, the maximum N_2 yield was not significantly affected by the concentration of water vapor. In fact, additional water actually gave rise to enhanced N_2 yields at temperatures above 400°C. The increase in the efficiency of hydrocarbon utilization through the suppression of undesired propene combustion by water had been reported by researchers who worked with In_2O_3/Al_2O_3 [20,26]. The positive role of water in such catalyst was

proposed to be the removal of carbonaceous materials that covered the catalytically active sites [26,27].

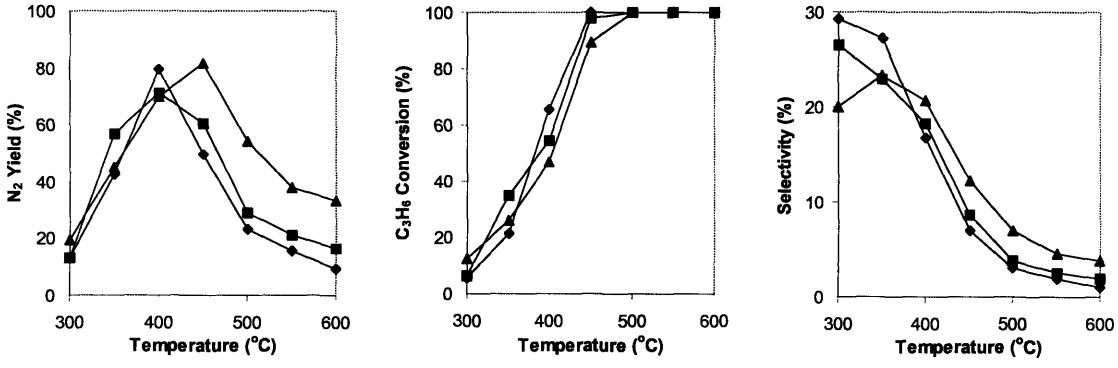

Figure 2.14. Effect of water vapor concentration on the N_2 yield, propene conversion and selectivity for NO reduction by propene over the In_2O_3-Ga_2O_3/Al_2O_3 nanocomposite with 2 wt% In and 8 wt% Ga. The reactions were run at a space velocity of 30,000 h^{-1} with 0.1% NO, 0.1% C_3H_6, 15% O_2, and (♦) 2%, (■) 5% or (▲) 10% H_2O.

The activity of the In_2O_3-Ga_2O_3/Al_2O_3 nanocomposite was stable over 100 hours in the presence of 10% water vapor at 450°C and a space velocity of 60,000 h^{-1}. Furthermore, there was negligible loss in surface area, indicating that this catalyst was hydrothermally stable under these reaction conditions.

2.3.4.5. Effect of Sulfur Dioxide

The resistance of the In_2O_3-Ga_2O_3/Al_2O_3 nanocomposite against SO_2 poisoning was examined at 450°C in the presence of 100 ppm SO_2. Figure 2.15 shows that the N_2 yield fell over 10 hours from ~ 80% to 60% upon exposure to SO_2. The yield appeared to stabilize at 60% over the next 10 hours. The reduction in N_2 yield could be attributed to decreases in both propene conversion and selectivity as a result of SO_2 adsorption and sulfate formation on the catalyst surface. The presence of sulfate species has been shown to reduce nitrate formation over Ga_2O_3-Al_2O_3 catalyst due to competitive adsorption between the two species on the basic oxygen sites [28]. Thus, the quantity of adsorbed NO_x species over our nanocomposite catalyst was expected to decrease when SO_2 was added to the feed stream. This poisoning of NO_x adsorption sites together with the creation of Brønsted acid sites by SO_2 adsorption over the propene activation sites

[28,29] could cause the selectivity to decrease. However, upon the removal of SO_2 from the feed stream after 24 hours of exposure, 85% of the original N_2 yield was recovered within 5 hours, and ~ 90% of the original yield was obtained after 24 hours. This was due to the high degree of recovery in propene conversion, despite some loss in catalyst selectivity.

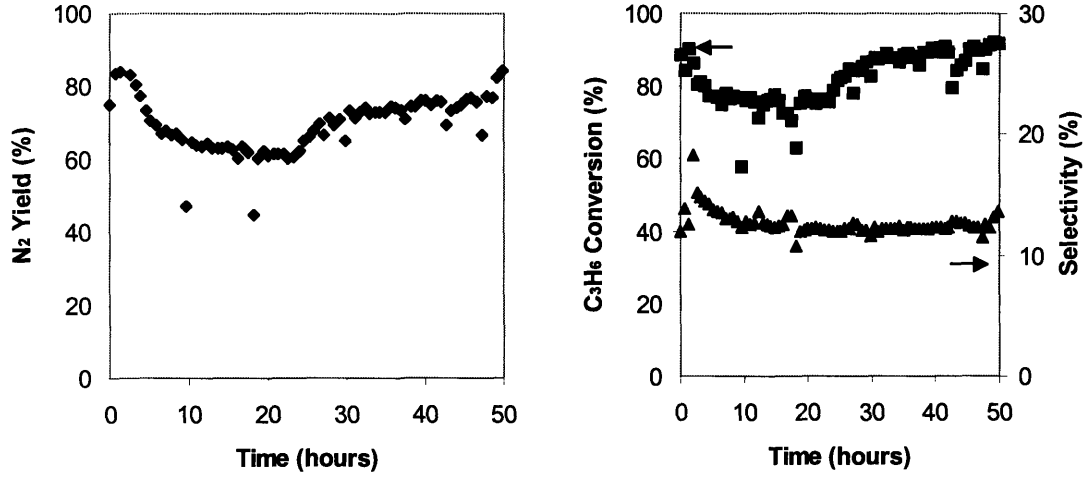

Figure 2.15. Effect of SO_2 on the (♦) N_2 yield, (■) propene conversion and (▲) selectivity for NO reduction by propene over the In_2O_3-Ga_2O_3/Al_2O_3 nanocomposite with 2 wt% In and 8 wt% Ga. The reactions were run at a space velocity of 30,000 h^{-1} with 0.1% NO, 0.1% C_3H_6, 15% O_2, and 10% H_2O at 450°C. SO_2 was introduced in the feed stream for the first 24 hours.

2.3.4.6. Effect of NO_x Species

The SCR of NO by hydrocarbons over many types of catalysts was commonly believed to proceed through the reaction of hydrocarbons with surface nitrates formed via adsorption of NO_2, which was produced in the reaction between NO and O_2 [2-4]. This proposition came from the observation that the rate of N_2 formation over many catalysts increased when NO was replaced by NO_2. As a result, strategies to promote the oxidation of NO to NO_2 (e.g. through the use of non-thermal plasma [30,31] and various pre-oxidation catalysts such as Pt/Al_2O_3) had been proposed to improve the de-NO_x performance of various SCR catalysts. Figure 2.16 shows that the maximum N_2 yield over the In_2O_3-Ga_2O_3/Al_2O_3 nanocomposite catalyst was improved substantially when NO_2 was used instead of NO with propane as the reducing agent. This was due to an increase in hydrocarbon conversion. When propene was used as the reducing agent, NO_2

did not give rise to distinct benefits over NO. The difference in the relative reactivity of propane and propene towards the two types of NO_x species could be attributed to the differences in their SCR mechanisms as reported in the literature [32,33].

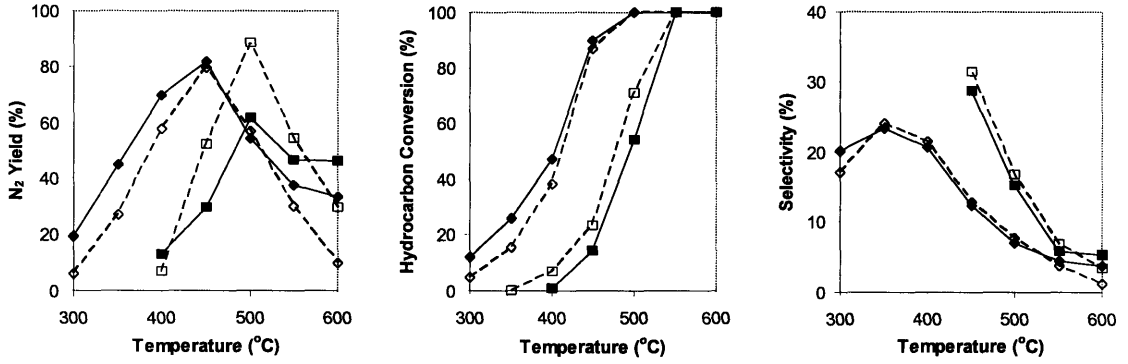

Figure 2.16. N_2 yield, propene conversion and selectivity for (♦,■) NO and (◊,□) NO_2 reduction by (♦,◊) propene and (■,□) propane over the In_2O_3-Ga_2O_3/Al_2O_3 nanocomposite with 2 wt% In and 8 wt% Ga. The reactions were run at a space velocity of 30,000 h^{-1} with 0.1% NO, 0.1% C_3H_6 or C_3H_8, 15% O_2, and 10% H_2O.

Park *et al.* had shown that while the role of In_2O_3 in In_2O_3/Al_2O_3 catalyst was to promote the activation of propene to acrolein, which subsequently reacted on Al_2O_3 to produce N_2, In_2O_3 did not promote the NO_x reduction over pure Al_2O_3 when propane was used as a reductant [18]. This indicated that the activation of propene and propane occurred on different active sites. The different behavior of propene and propane was also observed over our In_2O_3-Ga_2O_3/Al_2O_3 nanocomposites. While In addition clearly improved the propene conversion over these catalysts (Figure 2.10), it had only a minor effect on the propane conversion in SCR of NO (see Figure 2.17). Study on SCR of NO over Ag/Al_2O_3 had also shown that the catalyst activity was adversely affected by the presence of SO_2 when propane was used, while this was not the case with propene [29]. This finding had led to the conclusion that the SCR of NO_x by propane took place on the support, which was easily poisoned by SO_2, while the SCR of NO_x by propene occurred on the Ag particles [29].

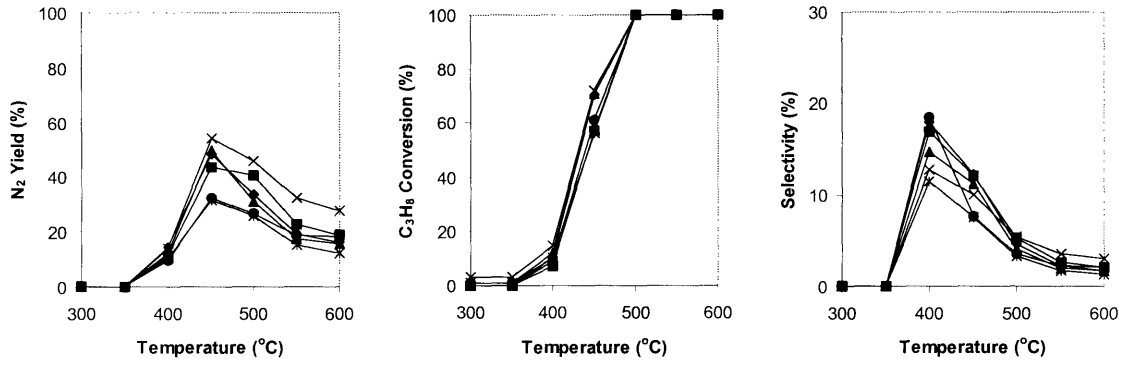

Figure 2.17. N_2 yield, propane conversion and selectivity for NO reduction by propane over In_2O_3-Ga_2O_3/Al_2O_3 nanocomposites containing a total metal loading of 10 wt%, with (♦) 0 wt%, (■) 2 wt%, (▲) 4 wt%, (×) 6 wt%, (*) 8 wt% and (●) 10 wt% In. The reactions were run at a space velocity of 30,000 h^{-1} with 0.1% NO, 0.1% C_3H_8, 15% O_2, and 10% H_2O.

According to the scheme proposed by Haneda *et al.* for Ga_2O_3/Al_2O_3 [26,34,35], the SCR of NO_x by propene over our In_2O_3-Ga_2O_3/Al_2O_3 nanocomposite catalyst would be expected to proceed via the reaction of partially oxidized propene species with the adsorbed nitrates to form various R-NO_x on In_2O_3-Ga_2O_3, followed by the migration of these species to the Al_2O_3 support where N_2 formation would take place. In contrast, the SCR of NO_x by propane would occur on the Al_2O_3 support itself. The use of NO_2 instead of NO could possibly enhance the formation of nitrates on Al_2O_3, leading to an increase in the SCR rate over the support when propane was used, and a decrease in the SCR rate when propene was used due to the competitive adsorption between R-NO_x and nitrates on Al_2O_3.

On the other hand, given a particular reductant, the use of NO_2 had little impact on the catalyst selectivity as calculated on an all-NO basis, which would indicate that the choice of NO_x species had no significant effect on the reaction mechanism. The above results suggested that the SCR activity over this type of material could potentially benefit from the pre-oxidation of NO to NO_2, although such effect was expected to be small in comparison to the effect of the hydrocarbon composition in the exhaust.

2.3.5. NO TPD Studies

Studies on the formation and reaction of surface nitrates by Haneda *et al.* [22], Meunier *et al.* [15] and Shimizu *et al.* [14] showed that adsorbed NO_x species over alumina-based catalysts were highly reactive towards hydrocarbons. Upon exposure to reductants, these species would react to form N_2 at rates similar to those found in steady-state NO reduction, suggesting that these surface nitrates played an important role in the SCR process. To quantify the amount of NO_x adsorbed on the surface of our nanocomposites, TPD experiments were performed to obtain the NO and O_2 desorption profiles (see Figure 2.18). Two desorption peaks due to nitrate decomposition were observed in all nanocomposites examined – NO desorption at 120°C, and a simultaneous desorption of NO and O_2 at 400°C. The amounts of nitrate species desorbed over the high-temperature region where the SCR of NO_x occurred are shown in Table 2.4.

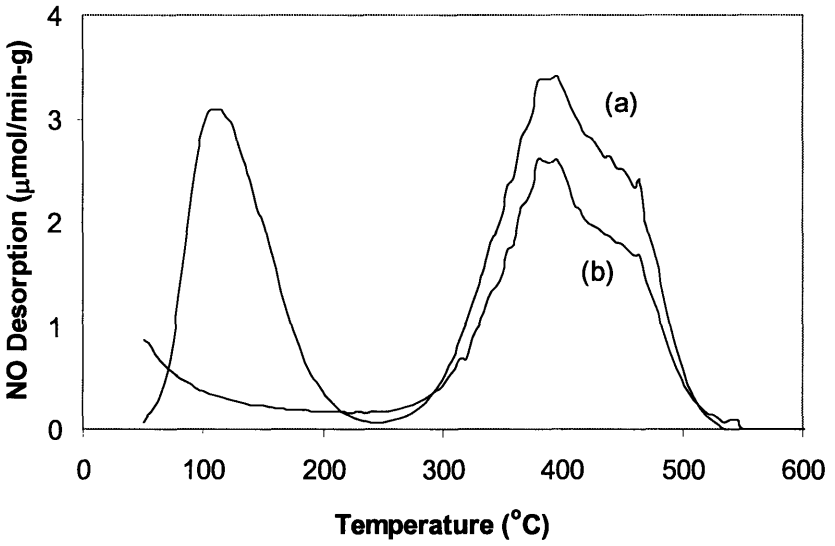

Figure 2.18. TPD profiles of (a) NO and (b) O_2 for In_2O_3-Ga_2O_3/Al_2O_3 nanocomposite with 2 wt% In and 8 wt% Ga. 0.2 g of the sample was pretreated in a flow of 15% O_2 in He at 600°C for 2 hours, followed by NO adsorption in 0.1% NO and 15% O_2 at 50°C for 2 hours. Desorption was performed at a heating rate of 2°C/min in a He flow of 60 cm^3/min.

Table 2.4. Amount of NO desorbed at 200–600°C from In_2O_3-Ga_2O_3/Al_2O_3 nanocomposites.

Ga Loading (wt%)	In Loading (wt%)	NO Desorbed (μmol NO/g)	NO Desorbed (μmol NO/m^2)
0	0	130	0.67
10	0	190	0.92
8	2	230	1.02
6	4	250	1.03
4	6	290	1.08
2	8	285	1.00
0	10	220	0.86

Coating of either Ga_2O_3 or In_2O_3 increased the amount of NO desorbed from the Al_2O_3-based catalyst, but the most significant increases in NO desorbed were associated with the nanocomposites that contained both Ga_2O_3 and In_2O_3. These findings indicated that the number of NO_x adsorption sites was increased with the presence of Ga_2O_3 or In_2O_3 coatings. The coexistence of Ga and In species also appeared to lead to a synergistic effect, creating an even greater number of NO_x adsorption sites in the nanocomposite catalysts. The addition of In species might have improved the dispersion of Ga species, besides increasing the BET surface area of the catalyst.

2.3.6. Kinetic Studies of NO Reduction by Propene

To examine the effect of water on the reaction mechanism of NO reduction by propene, the apparent kinetic rate orders at 375°C and the activation energies for N_2 formation over Ga_2O_3/Al_2O_3 were measured and summarized in Table 2.5. In the absence of water, the rate of N_2 formation increased with the increase in NO concentration, but was unaffected by the amount of propene, which suggested that the surface of the catalyst was largely covered by chemisorbed propene species. Our results contradicted with those of Haneda *et al.*, where the reaction order with respect to NO on Ga_2O_3-Al_2O_3 was reported to be zero [13], but this difference could be due to the higher reaction temperature of 450°C for their experiments. At higher temperatures, the propene

conversion was higher, and therefore less propene and relatively more NO_x would be present on the surface. As the surface coverage of adsorbed propene species decreased from 1, the rate order for propene should increase while that of NO should decrease due to the availability of active sites. This suggested that the SCR of NO_x over our nanocomposites could be viewed as a competitive adsorption between NO and propene in the framework of Langmuir-type mechanism as proposed by Toops *et al.* [36].

Table 2.5. Kinetic parameters for the N_2 formation over Ga_2O_3/Al_2O_3 (C) with 10 wt% Ga.

Water (mol%)	Reaction Order [a]			Activation Energy[b] (kJ/mol)
	NO	C_3H_6	O_2	
0	0.8	0.0	0.5	35
10	0.9	0.5	0.6	53

[a] The reactions were run at space velocities of 60,000–120,000 h^{-1} at 375°C with 0.02–0.2% NO, 0.02–0.2% C_3H_6, 3–20% O_2, and 0% or 10% H_2O.
[b] Activation energies were estimated at a space velocity of 30,000 h^{-1} between 350°C and 450°C with 0.1% NO, 0.1% C_3H_6, 15% O_2, and 0% or 10% H_2O.

The presence of water in the feed caused the reaction orders for all the reactants to increase, indicating that both NO adsorption and propene adsorption were inhibited by water molecules. This effect was more pronounced on the rate order of propene than on the rate order of NO, which was in agreement with the experimental observations that the presence of water reduced propene conversion and increased catalyst selectivity.

The effect of In content on the rate orders for NO, propene and oxygen over In_2O_3-Ga_2O_3/Al_2O_3 nanocomposites is shown in Table 2.6. For N_2 formation, the rate orders with respect to NO and oxygen decreased with increasing In loading, while the reverse was true for propene rate order. Similar trends in the NO and propene rate orders were also observed for the CO_x formation reaction, suggesting that the adsorption of propene relative to NO on the catalyst surface decreased as a result of In addition. This conclusion was consistent with the idea that In promoted the SCR of NO_x by increasing the propene conversion over the catalyst. However, as previously noted, this improvement came at the expense of catalyst selectivity as a result of higher propene

combustion, which was evident from the decrease in NO rate order for the CO_x formation reaction in the presence of In.

Table 2.6. Kinetic parameters for the formations of N_2 and CO_x over In_2O_3-Ga_2O_3/Al_2O_3 nanocomposites with a total metal loading of 10 wt%.

Reaction	In Loading (wt%)	Reaction Order with Respect to[a]			Activation Energy[b] (kJ/mol)
		NO	C_3H_6	O_2	
NO to N_2	0	0.9	0.5	0.6	53
	2	0.7	0.6	0.5	51
	4	0.7	1.0	0.4	51
C_3H_6 to CO_x	0	0.7	0.5	0.7	73
	2	0.3	0.6	0.5	46
	4	0.4	0.9	0.7	44

[a] The reactions were run at space velocities of 60,000–120,000 h^{-1} at 375°C with 0.02–0.2% NO, 0.02–0.2% C_3H_6, 3–20% O_2, and 10% H_2O.
[b] Activation energies were estimated at a space velocity of 30,000 h^{-1} between 350°C and 450°C with 0.1% NO, 0.1% C_3H_6, 15% O_2, and 10% H_2O.

The activation energy for N_2 formation remained at ~ 50 kJ/mol when In was added, indicating that the rate-limiting step of the SCR process was not altered. In contrast, the activation energy for CO_x formation was lowered significantly in the presence of In, possibly due to new pathways for propene conversion.

2.4. Summary

Nanocrystalline Al_2O_3-supported catalysts active for the SCR of NO by propene were synthesized by a novel sequential precipitation technique. The Ga_2O_3/Al_2O_3 catalyst prepared by this method exhibited excellent NO reduction activity compared with those produced by the impregnation and sol-gel methods due to its higher surface area and superior dispersion of Ga species. However, the activity of this catalyst was lowered in the presence of 10% H_2O due to reduced propene conversion. By introducing a combination of metal oxide coatings of Ga_2O_3, SnO_2 and In_2O_3 on Al_2O_3, excellent catalyst activity could be achieved in the presence of water vapor despite some decrease in propene selectivity. In fact, high N_2 yields of ~ 80% were achieved over In_2O_3-

Ga_2O_3/Al_2O_3 nanocomposites at 450°C. The improved activity was attributed to better propene activation by In and improved NO_x adsorption. The In_2O_3-Ga_2O_3/Al_2O_3 nanocomposites remained active even in the presence SO_2, where only a temporary reduction in N_2 yield was observed. Propene was found to be more reactive than propane at NO reduction over these nanocomposite catalysts. The catalyst activity also improved when NO_x was introduced in the form of NO_2 instead of NO.

Kinetic rate orders for NO and propene over In_2O_3-Ga_2O_3/Al_2O_3 nanocomposites were found to depend on the coating composition. In the presence of water, the propene rate order increased with increasing In loading, indicating a decrease in the relative surface coverage of propene, consistent with greater propene combustion observed in reactor studies.

2.5. References

[1] B.I. Bertelsen, Top. Catal. 16/17 (2001) 15.

[2] M. Amiridis, T. Zhang, R.J. Farrauto, Appl. Catal. B 10 (1996) 203.

[3] A. Fritz, V. Pitchon, Appl. Catal. B 13 (1997) 1.

[4] R. Burch, J.P. Breen, F.C. Meunier, Appl. Catal. B 39 (2002) 283.

[5] H.H. Kung, M.C. Kung, Catal. Today 30 (1996) 5.

[6] M. Iwamoto, H. Yahiro, Y. Yu-u, S. Shundo, N. Mizuno, Shikubai 32 (1990) 430.

[7] W. Held, A. Koenig, T. Richter, L. Puppe, SAE Paper 900496 (1990).

[8] P.W. Park, H.H. Kung, D.-W. Kim, M.C. Kung, J. Catal. 184 (1999) 440.

[9] J.Y. Yan, M.C. Kung, W.M.H. Sachtler, H.H. Kung, J. Catal. 172 (1997) 178.

[10] N. Bogdanchikova, F.C. Meunier, M. Avalos-Borja, J.P. Breen, A. Pestryakov, Appl. Catal. B 36 (2002) 287.

[11] K. Shimizu, J. Shibata, H. Yoshida, A. Satsuma, T. Hattori, Appl. Catal. B 30 (2001) 151.

[12] K. Shimizu, M. Takamatsu, K. Nishi, H. Yoshida, A. Satsuma, T. Tanaka, S. Yoshida, T. Hattori, J. Phys. Chem. B 103 (1999) 1542.

[13] M. Haneda, Y. Kintaichi, H. Shimada, H. Hamada, J. Catal. 192 (2000) 137.

[14] K. Shimizu, H. Kawabata, A. Satsuma, T. Hattori, J. Phys. Chem. B 103 (1999) 5240.

[15] F.C. Meunier, J.P. Breen, V. Zuzaniuk, M. Olsson, J.R.H. Ross, J. Catal. 187 (1999) 493.

[16] Y. Chi, S.S.C. Chuang, J. Catal. 190 (2000) 75.

[17] T. Maunula, J. Ahola, H. Hamada, Appl. Catal. B 26 (2000) 173.

[18] P.W. Park, S.C. Ragle, C.L. Boyer, M.L. Balmer, M. Engelhard, D. McCready, J. Catal. 210 (2002) 97.

[19] T. Maunula, Y. Kintaichi, M. Inaba, M. Haneda, K. Sato, H. Hamada, Appl. Catal. B 15 (1998) 291.

[20] T. Miyadera, K. Yoshida, Chem. Lett. (1993) 1483.

[21] K. Maeda, F. Mizukami, S. Niwa, M. Toba, M. Watanabe, K. Masuda, J. Chem. Soc. Faraday Trans. 88 (1992) 97.

[22] M. Haneda, Y. Kintaichi, T. Mizushima, N. Kakuta, H. Hamada, Appl. Catal. B 31 (2001) 81.

[23] A. Yezerets, Y. Zhang, P.W. Park, M.C. Kung, H.H. Kung, Stud. Surf. Sci. Catal. 130 (2000) 629.

[24] J.-H. Lee, A. Yezerets, M.C. Kung, H.H. Kung, Chem. Commun. (2001) 1404.

[25] M. Haneda, Y. Kintaichi, H. Hamada, Catal. Today 54 (1999) 391.

[26] M. Haneda, Y. Kintaichi, N. Bion, H. Hamada, Appl. Catal. B 42 (2003) 57.

[27] M. Haneda, Y. Kintaichi, H. Hamada, Catal. Lett. 55 (1998) 47.

[28] M. Haneda, Y. Kintaichi, H. Hamada, Appl. Catal. B 31 (2001) 251.

[29] T.N. Angelidis, S. Christoforou, A. Bongiovanni, N. Kruse, Appl. Catal. B 39 (2002) 197.

[30] H. Miessner, K.P. Francke, R. Rudolph, Appl. Catal. B 36 (2002) 53.

[31] R.G. Tonkyn, S.E. Barlow, J.W. Hoard, Appl. Catal. B 40 (2003) 207.

[32] R. Burch, T.C. Watling, in: N. Kruse, A. Frennet, J.-M. Bastin (Eds.), Studies in Surface Science and Catalysis: Catalysis and Automotive Pollution Control IV, Vol. 116, Elsevier, Amsterdam, 1998, p. 199.

[33] S.-K. Park, Y.-K. Park, S.-E. Park, L. Kevan, Phys. Chem. Chem. Phys. 2 (2000) 5500.

[34] M. Haneda, E. Joubert, J.-C. Ménézo, D. Duprez, J. Barbier, N. Bion, M. Daturi, J. Saussey, J.-C. Lavalley, H. Hamada, J. Mol. Catal. A 175 (2001) 179.

[35] M. Haneda, N. Bion, M. Daturi, J. Saussey, J.-C. Lavalley, D. Duprez, H. Hamada, J. Catal. 206 (2002) 114.

[36] T.J. Toops, A.B. Walters, M.A. Vannice, Appl. Catal. B 38 (2002) 183.

Chapter 3 – Metal Oxide Nanocomposites as SO_2 Storage Materials

3.1. Introduction

Over the past few years, increase in environmental concern has led to demands for more effective technologies towards engine pollution control. New EPA regulations on automotive emissions of nitrogen oxides (NO_x) are due to take effect in 2004 [1]. However, the removal of NO_x from lean-burn and diesel engines operating under an oxygen-rich atmosphere presents significant challenges as the conventional three-way catalysts are ineffective in this environment [2-4]. Moreover, the wide range of temperatures typically encountered in real engine operation and the chemical complexity of gasoline and diesel fuels make implementations of the direct reduction catalysts difficult [4,5]. To address this issue, NO_x storage-reduction (NSR) catalysts have been developed to store NO_x in the form of metal nitrates [6-8] under fuel-lean condition. The nitrates were then released and reduced to nitrogen during the fuel-rich period. However, as the NO_x storage components of the NSR systems were typically alkaline or alkaline earth metal oxides, such as BaO [9-13], such sorbents were easily poisoned by the SO_2 present in the fuel exhaust with the blockage of storage sites by sulfate formation [14-17]. One possible solution was to develop materials capable of trapping SO_2 upstream of the NO_x bed in an oxygen-rich environment in the form of metal sulfates, and releasing SO_2 under the reducing atmosphere [18,19]. To prevent sulfur poisoning of the noble metals on the NSR catalyst during the fuel-rich period [20], regeneration of the traps could be done in the reverse order, starting with the NO_x bed, followed by the SO_x bed.

Recently, the development of regenerative sorbents for the simultaneous removal of SO_2 and NO_x from the flue gas desulfurization process has attracted substantial interest. Amongst the materials studied, CuO/Al_2O_3 [21-25] showed the most promise for practical applications as it readily adsorbed SO_2 in the presence of oxygen to form $CuSO_4$ at 300–500°C, and could be regenerated under reducing conditions at the same temperatures using gases such as hydrogen, methane, and carbon monoxide. However, further improvements in the SO_2 adsorption capacity and low-temperature regenerability are necessary for these sorbents to be used as SO_x trap for the NSR system, which has to operate at the low temperatures of the exhaust stream with limited reduction potential.

In this chapter, various noble metal-loaded CuO/Al_2O_3 nanocomposites were synthesized and examined for SO_2 entrapment. The effects of the preparation method and nanocomposite composition on the performance of these sorbents were evaluated according to their SO_2 adsorption capacity and regenerability by CO.

3.2. Experimental

3.2.1. Sorbent Preparation

To achieve high surface area materials with good dispersion of active components, nanocrystalline CuO/Al_2O_3 (C) sorbents were prepared using a sequential chemical precipitation technique. An aqueous solution of aluminum nitrate was first added to a solution of tetraethylammonium hydroxide to yield an aluminum hydroxide precipitate. After aging for 24 hours, a selected amount of copper nitrate solution was then added to the precipitate, and stirred for 24 hours. The resulting precipitate was centrifuged, washed, dried, and calcined at 500°C in air for 6 hours.

To study the effect of synthesis technique, CuO/Al_2O_3 (I) was prepared by impregnation. In this case, the aluminum hydroxide precipitate described earlier was centrifuged, washed, dried, and calcined at 500°C in air for 6 hours. Cu was then impregnated onto the calcined alumina support using an aqueous solution of copper nitrate. The resulting material was dried and calcined at 500°C in air for 6 hours.

Noble metals were impregnated onto the calcined CuO/Al_2O_3 using mixtures of dihydrogen hexachloroplatinate (IV), tetraamineplatinum (II) hydroxide and rhodium (II) nitrate solutions. The resulting materials were calcined at 500°C in air for 3 hours to yield the noble metal-loaded CuO/Al_2O_3 sorbents.

3.2.2. Sorbent Characterization

Sorbent surface area and pore size distribution were calculated from the nitrogen adsorption isotherm (Micromeritics ASAP 2000) using the BET and BJH methods, respectively. Phase identification was achieved by X-ray diffraction (XRD) with a Siemens D5000 diffractometer using Cu Kα radiation at 45 kV and 40 mA. Scherrer's analysis of X-ray peak broadening was employed to determine crystallite size.

3.2.3. SO_2 Adsorption and Regeneration

SO_2 adsorption and regeneration activities of the sorbents were studied in a quartz tube fixed-bed reactor under alternate oxidizing and reducing atmospheres. A feed gas mixture that contained 300 ppm SO_2 and either 0.5% O_2 or 1% CO with He as a balance was fed to 0.04 g of sorbent at a total flow rate of 100 cm^3/min, which corresponded to a contact time of 0.024 g·s/cm^3 or a space velocity of ~ 80,000 h^{-1}. The feed compositions as well as the durations of O_2 and CO pulses were controlled using the National Instruments Lab View, in conjunction with solenoid valves to switch between O_2 and CO. The reactor effluent was analyzed with a VG Gas Lab 300 mass spectrometer. Masses of 28 (CO), 32 (O_2), 40 (Ar), 44 (CO_2), and 64 (SO_2) were continuously monitored with a constant feed of 0.18% Ar as internal reference. A HP 6890 Plus gas chromatograph equipped with a Chromosil 310 column was also used to allow oxygen/carbon monoxide, carbon dioxide, carbonyl sulfide, hydrogen sulfide, carbon disulfide and sulfur dioxide to be separated and quantified. No COS, H_2S or CS_2 were detected in this work.

3.2.4. Temperature-Programmed Desorption (TPD)

In a typical TPD experiment, SO_2 adsorption was performed by exposing 0.04 g of sorbent to a flow of 1% SO_2 and 2% O_2 in He at 400°C for 2 hours. After subsequent cooling to 200°C, desorption of adsorbed species was performed at a ramp rate of 2°C/min in a 100 cm^3/min flow of 1% CO in He with 0.25% Ar as internal standard. The reactor effluent was analyzed using a HP 6890 Plus gas chromatograph equipped with a HP 5972A mass selective detector.

3.3. Results and Discussion

3.3.1. Effect of Preparation Method

CuO/Al_2O_3 sorbents with various Cu loadings were prepared using both the wet-impregnation method (I) and the sequential precipitation method (C). The SO_2 outlet concentrations detected downstream of these sorbents with 30 wt% Cu during the second isothermal adsorption cycle at 400°C are shown in Figure 3.1. The SO_2 adsorption

analyses were performed after the materials had been subjected to one complete adsorption/desorption cycle under the test condition to ensure that only the regenerable portion of the adsorption capacity was measured. In fact, the amounts of SO_2 adsorbed during the first adsorption cycle were typically much larger since the aluminum sulfate formed in the reaction between SO_3 and the alumina support was stable at 400°C under the reducing atmosphere. These profiles illustrated the breakthrough capacity, which was defined as the amount of SO_2 retained by the sorbent before the SO_2 concentration in the exhaust stream reached 15 ppm. Figure 3.1 shows that the sequentially precipitated sorbent has a considerably higher breakthrough capacity than the impregnated sorbent. At breakthrough, over 50 mg of SO_2 could be adsorbed per gram of CuO/Al_2O_3 (C) with 30 wt% Cu. This represented a 17% conversion of CuO to $CuSO_4$, and marked the operational limit of the material before regeneration became necessary.

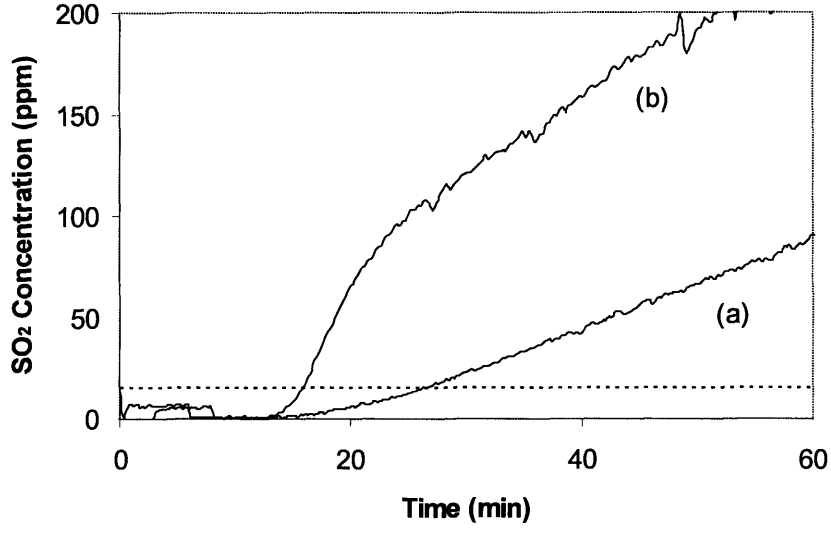

Figure 3.1. SO_2 concentration downstream of (a) CuO/Al_2O_3 (C) and (b) CuO/Al_2O_3 (I) sorbents with 30 wt% Cu during the second isothermal adsorption cycle at 400°C. The reactions were run at a space velocity of 80,000 h^{-1} with 300 ppm SO_2 and 0.5% O_2 for adsorption, and with 300 ppm SO_2 and 1% CO for desorption.

After 3 hours, CuO/Al_2O_3 (C) with 30 wt% Cu reached the saturation capacity of 172 mg SO_2/g sorbent despite an incomplete CuO conversion of 57%, indicating the presence of a diffusion barrier in the SO_2 adsorption process. To verify the effect of this

diffusion process, an analysis of sulfate penetration depth at breakthrough was performed on Cu/Al_2O_3 (I) and Cu/Al_2O_3 (C) with 30 wt% Cu. This analysis was simplified by assuming that the CuO particles were spherical and that their initial radius, r_o, could be estimated from Scherrer's analysis of the XRD peak width. Therefore, for a given CuO conversion, X, the unreacted radius, r_u, was given by:

$$r_u = (1 - X)^{1/3} r_o \tag{3.1}$$

The penetration depth, which was the difference between r_o and r_u, was obtained for the two sorbents (see Table 3.1).

Table 3.1. Surface area, CuO grain size and penetration depth of CuO/Al_2O_3 sorbents with 30 wt% Cu.

Sorbent	Surface Area[a] (m^2/g)	CuO Grain Size[a] (nm)	Penetration Depth (nm)
CuO/Al_2O_3 (I)	149	25	0.4
CuO/Al_2O_3 (C)	246	16	0.5

[a] The surface areas and CuO grain sizes were measured prior to SO_2 adsorption experiments.

With the penetration depth estimated at 0.4–0.5 nm for the two materials, the SO_2 adsorption process over CuO/Al_2O_3 at breakthrough appeared to be diffusion-controlled. As breakthrough occurred when the rate of diffusion, which decreased with increasing CuO conversion, dropped below the rate at which SO_2 was fed into the reactor, the breakthrough capacity was expected to depend on material characteristics as well as the operating parameters such as temperature, space velocity and SO_2 concentration. CuO/Al_2O_3 (C) achieved a higher breakthrough capacity than CuO/Al_2O_3 (I) because of its smaller CuO grain size. By coating freshly precipitated aluminum hydroxide particles with CuO in the sequential precipitation process, the growth of Al_2O_3 grains was suppressed during calcination, allowing a sorbent with higher surface area and superior CuO dispersion to be synthesized.

The transient SO_2 adsorption/desorption characteristics of CuO/Al_2O_3 with 30 wt% Cu over 20-min lean/rich cycles at 400°C are shown in Figure 3.2. Unlike CuO/Al_2O_3 (I), CuO/Al_2O_3 (C) demonstrated almost complete SO_2 adsorption over the first 15 cycles with minimal SO_2 slip. However, as the SO_2 outlet concentration at the

end of each desorption cycle only fell to ~ 400 ppm, the sorbent regeneration process was not complete. This resulted in the net accumulation of SO_2 on the sorbent, which reduced the SO_2 adsorption activity in subsequent cycles.

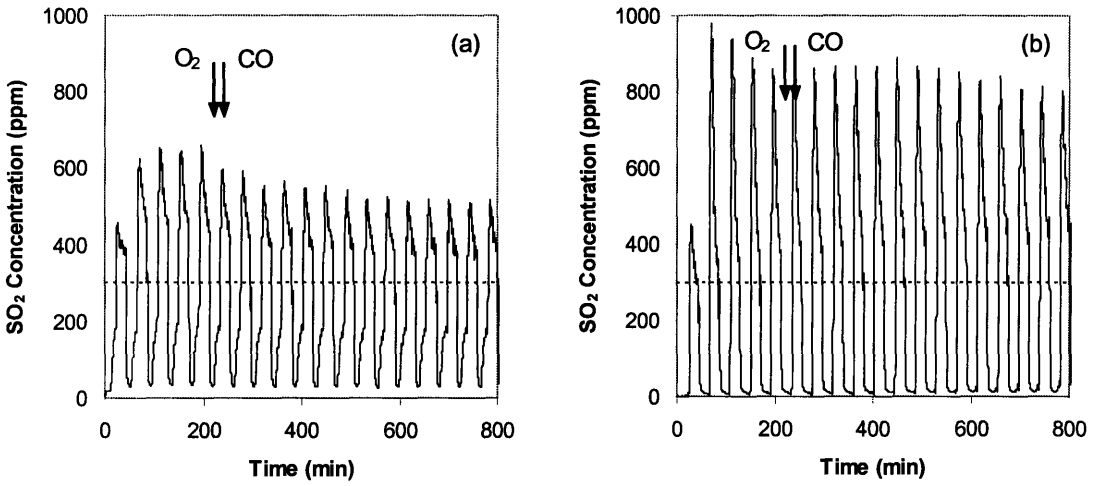

Figure 3.2. SO_2 adsorption/desorption profile of (a) CuO/Al_2O_3 (I) and (b) CuO/Al_2O_3 (C) with 30 wt% Cu at 400°C. The reactions were run at a space velocity of 80,000 h^{-1} with 300 ppm SO_2, and alternating pulses of 0.5% O_2 for 20 min and 1% CO for 20 min.

CuO/Al_2O_3 did not give rise to undesired decomposition of surface sulfate species into elemental sulfur, since no SO_2 desorption was observed at the beginning of each adsorption cycle when O_2 was introduced. Sulfur formation under reducing atmosphere was common amongst the other materials with low sulfate decomposition temperature, such as those containing Cr, Fe and Co [18].

3.3.2. CuO/Al_2O_3 Nanocomposites

3.3.2.1. Effect of Cu Loading

The effect of Cu loading on CuO/Al_2O_3 (C) sorbent's SO_2 adsorption activities during the second cycle is shown in Figure 3.3. Dramatic enhancements in the breakthrough capacity and the total adsorption capacity of the sorbent were observed with moderate addition of CuO. Increasing Cu loading beyond 40 wt%, however, led to reductions in the breakthrough capacity and the total adsorption capacity of the sorbents.

Figure 3.4 shows that while over 100 mg of SO_2 was retained by a gram of CuO/Al_2O_3 (C) with 40 wt% Cu before breakthrough, pure CuO demonstrated almost no reversible SO_2 adsorption capacity. The reduction in the breakthrough capacity at higher Cu loadings could be associated with lower sorbent surface area and larger CuO grain size (see Table 3.2).

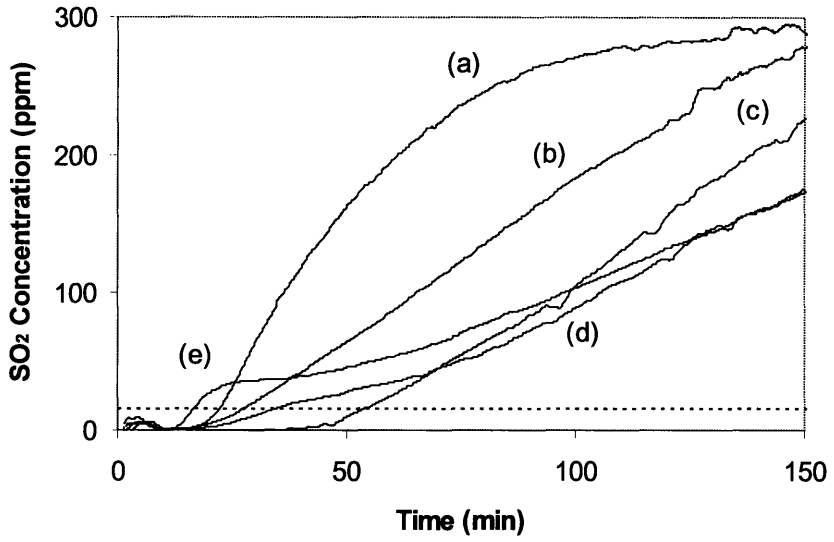

Figure 3.3. SO_2 concentration downstream of CuO/Al_2O_3 (C) sorbents with (a) 20 wt%, (b) 30 wt%, (c) 40 wt%, (d) 50 wt% and (e) 60 wt% Cu during the second isothermal adsorption cycle at 400°C. The reactions were run at a space velocity of 80,000 h^{-1} with 300 ppm SO_2 and 0.5% O_2 for adsorption, and with 300 ppm SO_2 and 1% CO for desorption.

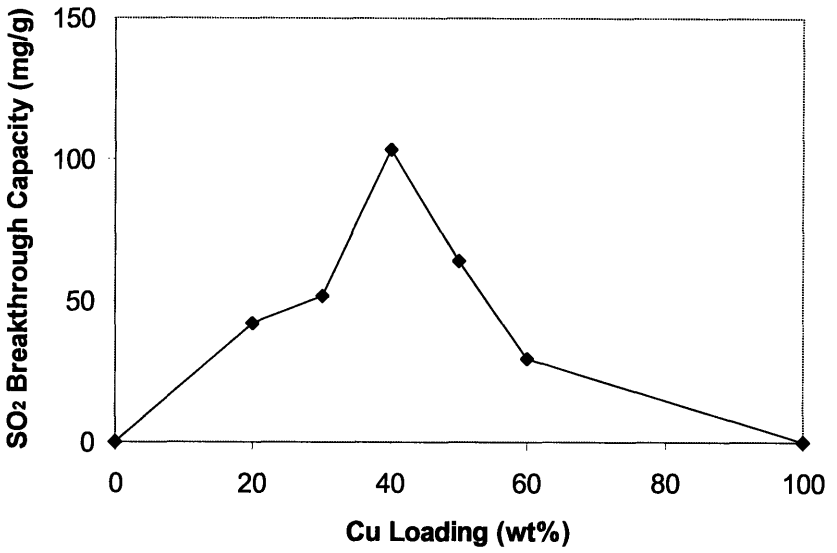

Figure 3.4. The effect of Cu loading on the SO_2 breakthrough capacity of CuO/Al_2O_3 (C) sorbents in the second isothermal adsorption cycle at 400°C. The reactions were run at a space velocity of 80,000 h^{-1} with 300 ppm SO_2 and 0.5% O_2 for adsorption, and with 300 ppm SO_2 and 1% CO for desorption.

Table 3.2. Surface area, pore volume, mean pore diameter and CuO grain size of CuO/Al_2O_3 (C) sorbents with various Cu loadings.

Cu Loading (wt%)	Surface Area (m^2/g)	Pore Volume (cm^3/g)	Pore Diameter (nm)	CuO Grain Size (nm)
0	340	0.71	6.6	N/A
20	298	0.91	11.0	16
30	246	1.04	13.0	16
40	162	0.73	14.2	18
50	125	0.64	17.8	18
60	70	0.23	10.6	20
100	6	N/A	N/A	29

To fully evaluate the sorbent's suitability as SO_x trap, the regeneration efficiency was also examined. Comparison was made between the SO_2 desorption rates of the SO_x-loaded sorbents with different Cu loadings by measuring the transient SO_2 adsorption/desorption characteristics over lean/rich cycles of 20-min O_2 pulses and 40-min CO pulses at 400°C. The SO_2 concentrations detected downstream from the

CuO/Al_2O_3 (C) sorbents with 30 wt% and 40 wt% Cu were shown in Figure 3.5. The cumulative SO_2 release profiles and average SO_2 desorption rates of these sorbents are shown in Figure 3.6. The results suggested that the Cu loading and the initial CuO grain size had little effects on the SO_2 desorption characteristic of the sorbents. This was not unexpected considering the fact that only ~ 10% of the CuO present was converted into $CuSO_4$ over any given adsorption cycle. Therefore, the size of the $CuSO_4$ particles should be small relative to that of the original CuO grains, regardless of the Cu loading. As a result, at a low SO_x loading, the SO_2 desorption rate should be independent of the sorbent's Cu loading.

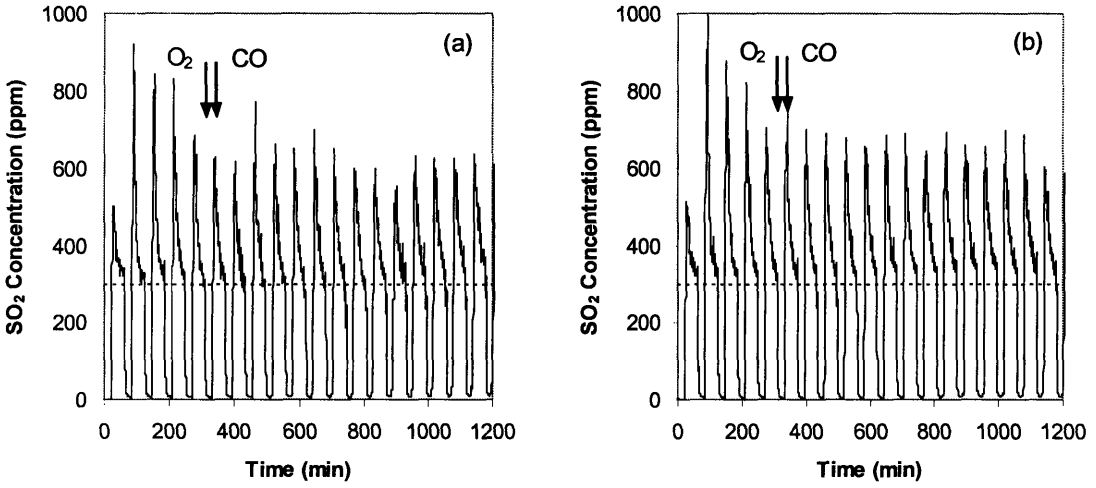

Figure 3.5. SO_2 adsorption/desorption profile of CuO/Al_2O_3 (C) sorbents with (a) 30 wt% and (b) 40 wt% Cu at 400°C. The reactions were run at a space velocity of 80,000 h^{-1} with 300 ppm SO_2, and alternating pulses of 0.5% O_2 for 20 min and 1% CO for 40 min.

Despite the low CuO conversion, the sorbent regeneration process was slow and inefficient as over 40 min were needed to completely regenerate the sorbent. In a typical desorption cycle, the SO_2 desorption rate quickly rose to a maximum at 2 mg/min·g, which represented 3% conversion of CO, before it gradually declined. On average, only 1.5% CO conversion was obtained over the entire desorption cycle. Therefore, the regeneration rate appeared to be controlled by the available quantity of adsorbed CO for reaction with $CuSO_4$, as indicated by the profile of SO_2 desorption rate normalized by the quantity of remaining sulfate in Figure 3.7.

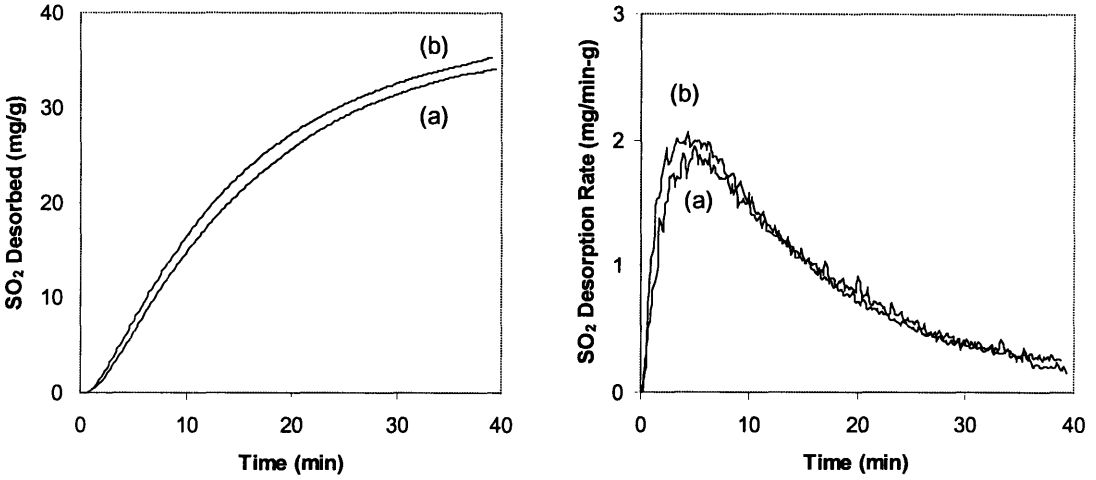

Figure 3.6. Cumulative SO_2 release profile and average SO_2 desorption rate of CuO/Al_2O_3 (C) sorbents with (a) 30 wt% and (b) 40 wt% Cu at 400°C.

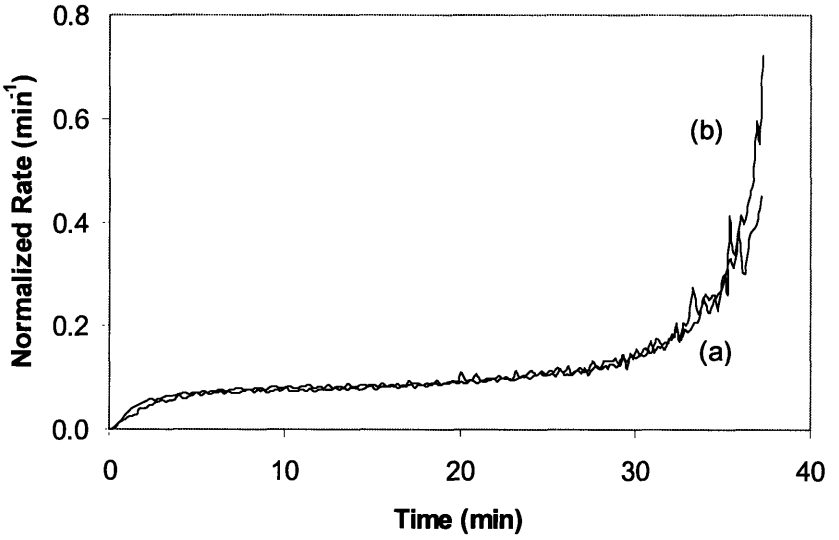

Figure 3.7. Average SO_2 desorption rate normalized by the remaining amount of adsorbed sulfate for CuO/Al_2O_3 (C) sorbents with (a) 30 wt% and (b) 40 wt% Cu at 400°C. The reactions were run at a space velocity of 80,000 h^{-1} with 300 ppm SO_2, and alternating pulses of 0.5% O_2 for 20 min and 1% CO for 40 min.

3.3.2.2. Effect of CO Concentration

To study the effect of CO concentration on the efficiency of the sorbent regeneration process, the transient SO_2 adsorption/desorption activities of CuO/Al_2O_3 (C)

with 30 wt% Cu were measured over lean/rich cycles with 20-min O_2 pulses and 40-min CO pulses at 400°C under various CO partial pressures. Figure 3.8 shows that the sorbent regeneration process was completed in 20 min and 16 min with 3.3% and 6.7% CO, respectively. The improvement in sulfate removal due to faster SO_2 desorption enabled more SO_2 to be adsorbed during the oxygen-rich part of the cycle. Thus, a better sorbent performance resulted with an average SO_2 concentration of ~ 13 ppm downstream of this SO_x trap over 24 hours of operation when higher CO concentrations of 3.3% and 6.7% were used. In contrast, performance deterioration was noted after the 14th cycle with 1% CO in the feed stream (see Figure 3.9). Most of the SO_2 in the exhaust was due to SO_2 slip that occurred at the beginning of each adsorption cycle, possibly as a result of slow re-oxidation of metallic Cu to CuO due to the limited amount of oxygen present in the feed stream. With higher oxygen concentration, this re-oxidation step could be shortened, thereby reducing the sorbent's initial SO_2 slip. The similarity in the sorbent performance when 3.3% and 6.7% CO were used also indicated that complete sulfate decomposition was necessary to maintain the sorbent's SO_2 capacity, and that sufficient regeneration could be achieved with 3.3% CO at a lean/rich cycle time ratio of 1 when 300 ppm SO_2 were present in the exhaust.

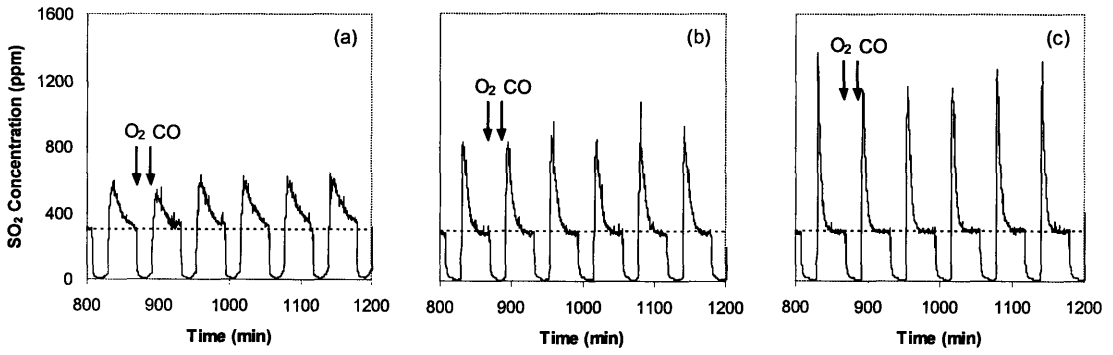

Figure 3.8. Effect of CO concentration on the SO_2 adsorption/desorption profile of CuO/Al_2O_3 (C) sorbent with 30 wt% Cu at 400°C. The reactions were run at a space velocity of 80,000 h^{-1} with 300 ppm SO_2, and alternating pulses of 0.5% O_2 for 20 min and (a) 1%, (b) 3.3% and (c) 6.7% CO for 40 min.

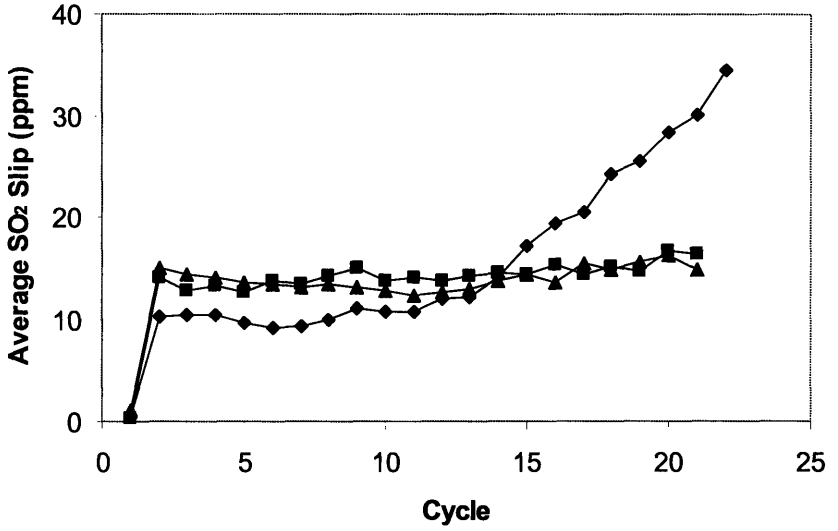

Figure 3.9. Average SO_2 concentration detected downstream of CuO/Al_2O_3 (C) sorbent with 30 wt% Cu during the adsorption cycle at 400°C. The reactions were run at a space velocity of 80,000 h^{-1} with 300 ppm SO_2, and alternating pulses of 0.5% O_2 for 20 min and (♦) 1%, (■) 3.3% and (▲) 6.7% CO for 40 min.

3.3.2.3. Effect of Operating Temperature

The effect of operating temperature on the breakthrough capacity and regenerability of CuO/Al_2O_3 (C) sorbent with 30 wt% Cu was examined by measuring the SO_2 outlet concentrations over the first and second isothermal adsorption/desorption cycles at temperatures ranging from 350°C to 450°C. Figure 3.10 shows that the initial period where all SO_2 was trapped was lengthened at higher operating temperatures. This increase in the breakthrough capacity with temperature could be attributed to an increase in SO_2 penetration depth from a higher diffusion rate. Figure 3.11 shows that the total adsorption capacity of the sorbent (as measured by the amount of SO_2 desorbed) also increased with the operating temperature, since a larger portion of the sulfate formed could be decomposed by CO.

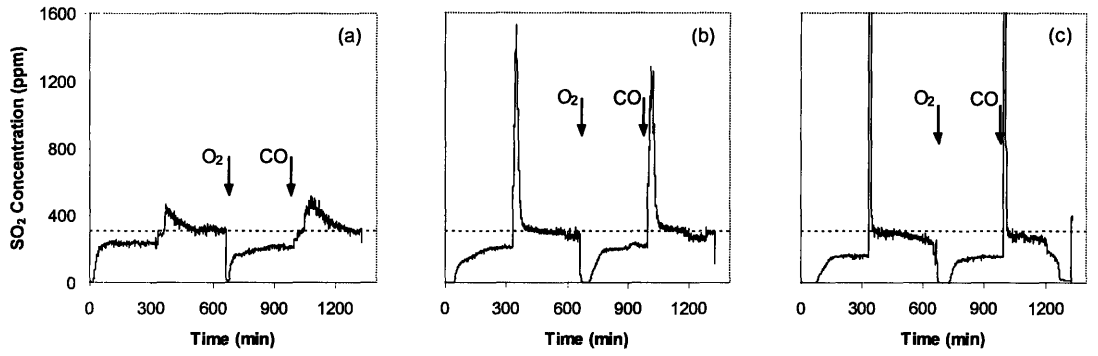

Figure 3.10. SO_2 adsorption/desorption profile of CuO/Al_2O_3 (C) sorbent with 30 wt% Cu during the first and second isothermal cycles at (a) 350°C, (b) 400°C and (c) 450°C. The reactions were run at a space velocity of 80,000 h^{-1} with 300 ppm SO_2, and alternating pulses of 0.5% O_2 for 20 min and 1% CO for 40 min.

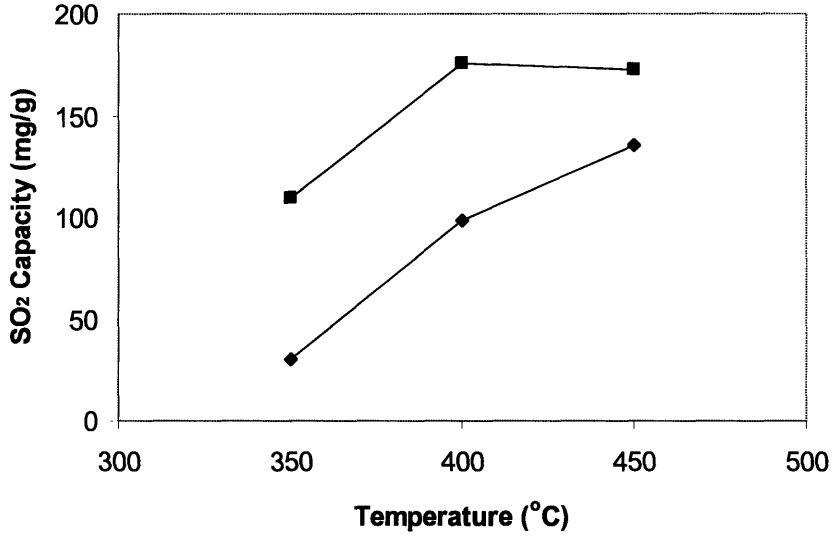

Figure 3.11. SO_2 (♦) breakthrough capacity and (■) total adsorption capacity for CuO/Al_2O_3 (C) sorbent with 30 wt% Cu measured during the second isothermal adsorption cycle at the operating temperature noted. The reactions were run at a space velocity of 80,000 h^{-1} with 300 ppm SO_2 and 0.5% O_2 for adsorption, and with 300 ppm SO_2 and 1% CO for desorption.

After the breakthrough capacity was reached, the SO_2 outlet concentration would gradually increase up to a point of saturation where a steady-state conversion of SO_2 to SO_3 was observed. The SO_3 formation increased from 12% at 350°C to 18% at 400°C, and 35% at 450°C. These values were significantly lower than their theoretical

thermodynamic equilibrium values where complete SO_2 oxidation were predicted, indicating that the adsorbed SO_x species formed on the sorbent were fairly stable under the oxidizing environment over this range of temperatures. As SO_3 formation occurred via the oxidation of SO_2 to produce intermediate surface sulfate species, the SO_x desorption rate likely depended on the decomposition rate of the sulfate accumulated [24-26]. Therefore, the SO_3 concentration downstream of the SO_x trap was expected to increase with the amount of SO_x loaded onto the sorbent, and the sulfur slip in the form of SO_3 before the breakthrough capacity was reached should be minimal.

Higher operating temperatures also improved the efficiency of the sorbent regeneration process by increasing the sulfate decomposition rate. Complete sorbent regeneration was achieved within 40 min and 70 min at 450°C and 400°C, respectively. In contrast, almost 4 hours were required to remove all the adsorbed SO_x at 350°C. These results were consistent with the SO_2 TPD measurements over CuO/Al_2O_3, which estimated the $CuSO_4$ decomposition temperature to be 420°C. The use of high regeneration temperature, however, would cause undesirable decomposition of surface sulfate into elemental sulfur, as indicated by the presence of SO_2 desorption peak during each adsorption cycle as a result of sulfur re-oxidation.

3.3.3. Pt-Loaded CuO/Al_2O_3

One way to improve the regeneration efficiency of the sorbent was to increase the amount of CO chemisorbed on its surface through the introduction of metals, such as Rh, Pd and Pt, which displayed strong affinity for CO. Pt was the most appealing of these metals because it would not form a stable sulfate species even in the oxidizing environment.

3.3.3.1. Effect of Pt Precursor

To examine the role of Pt precursors on the SO_2 trapping performance of Pt-loaded CuO/Al_2O_3 (C) nanocomposites, sorbents with 1 wt% Pt and 30 wt% Cu were prepared using dihydrogen hexachloroplatinate (IV) and tetraamineplatinum (II) hydroxide solutions. Their SO_2 adsorption/desorption characteristics over lean/rich

cycles with 20-min O_2 pulses and 40-min CO pulses at 400°C are shown in Figure 3.12. The nanocomposite prepared from dihydrogen hexachloroplatinate (IV) precursor exhibited a better and more stable SO_2 trapping ability over many cycles with lower levels of SO_2 slip. The average SO_2 concentrations measured downstream of the Pt-loaded CuO/Al_2O_3 (C) nanocomposites prepared with dihydrogen hexachloroplatinate (IV) and tetraamineplatinum (II) hydroxide precursors over the lean part of cycles #10–19 were 8 ppm and 13 ppm, respectively, which were significantly lower than the 17 ppm achieved by CuO/Al_2O_3 (C). Figure 3.13 shows that the superior SO_2 adsorption performance exhibited by the Pt-loaded nanocomposites were due to improved initial SO_2 desorption rate during the regeneration process, consistent with the idea that Pt enhanced the CO adsorption. The high desorption rate of ~ 4 mg/min·g achieved with the nanocomposite prepared with dihydrogen hexachloroplatinate (IV) precursor allowed the sorbent regeneration to be completed in just 30 min, slightly faster than that obtained by the sorbent prepared with tetraamineplatinum (II) hydroxide. The difference in the initial regeneration rates between the two materials could be attributed to better copper sulfate dispersion as a result of enhanced alumina surface wetting by chloride [27]. Figure 3.14 also shows that the initial SO_2 desorption rate from CuO/Al_2O_3 (C) increased with the impregnation of HCl. In fact, 1 wt% Pt-loaded CuO/Al_2O_3 (C) prepared by dihydrogen hexachloroplatinate (IV) precursor was similar in performance to that prepared from a mixture of tetraamineplatinum (II) hydroxide with an appropriate amount of HCl.

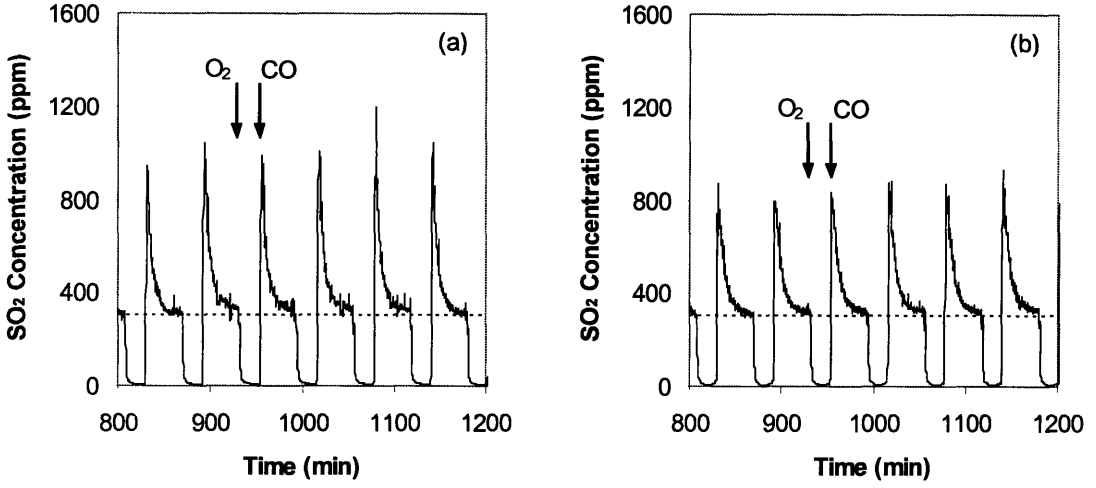

Figure 3.12. SO_2 adsorption/desorption profile of 1 wt% Pt-loaded CuO/Al_2O_3 (C) sorbents with 30 wt% Cu prepared with (a) dihydrogen hexachloroplatinate (IV) and (b) tetraamineplatinum (II) hydroxide precursors. The reactions were run at 400°C and a space velocity of 80,000 h^{-1} with 300 ppm SO_2, and alternating pulses of 0.5% O_2 for 20 min and 1% CO for 40 min.

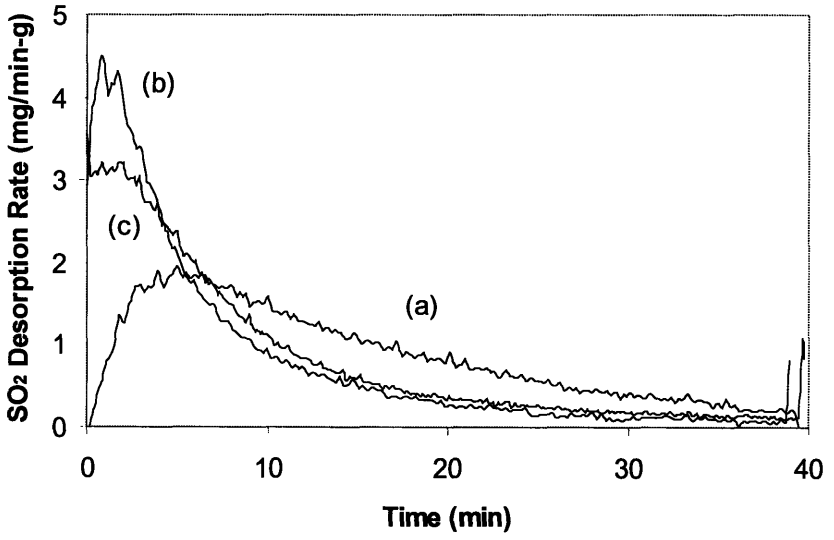

Figure 3.13. Average SO_2 desorption rate from CuO/Al_2O_3 (C) sorbents with 30 wt% Cu and (a) 0 wt% and (b,c) 1 wt% Pt, prepared with (b) dihydrogen hexachloroplatinate (IV) and (c) tetraamineplatinum (II) hydroxide precursors. The reactions were run at 400°C and a space velocity of 80,000 h^{-1} with 300 ppm SO_2, and alternating pulses of 0.5% O_2 for 20 min and 1% CO for 40 min.

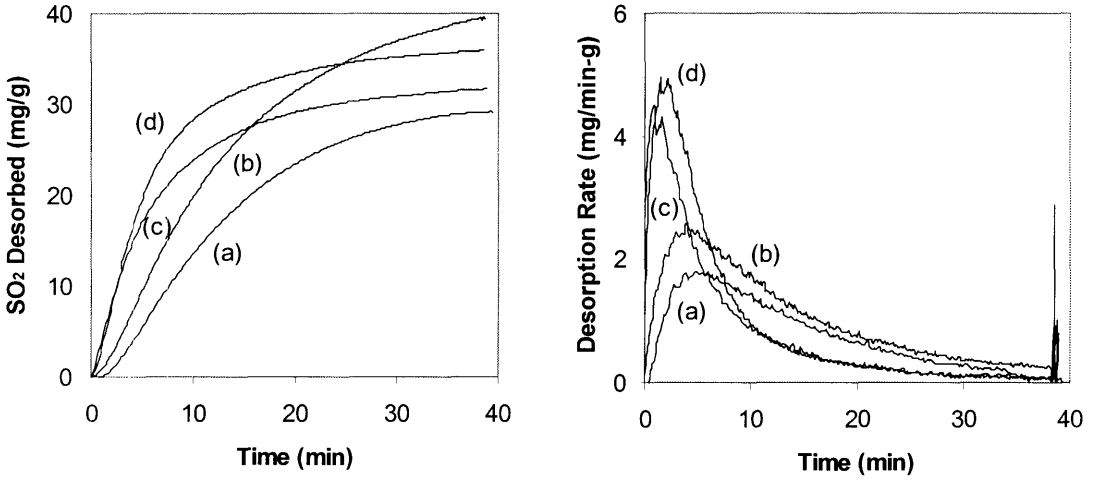

Figure 3.14. The cumulative SO_2 release profile and the average SO_2 desorption rate from CuO/Al_2O_3 (C) sorbents with 30 wt% Cu and (a) no HCl or Pt, (b) HCl, (c) 1 wt% Pt (using dihydrogen hexachloroplatinate (IV) precursor), and (d) HCl and 1 wt% Pt (using tetraamineplatinum (II) hydroxide precursor). The reactions were run at 400°C and a space velocity of 80,000 h^{-1} with 300 ppm SO_2, and alternating pulses of 0.5% O_2 for 20 min and 1% CO for 40 min.

3.3.3.2. Effect of Pt Loading

Using dihydrogen hexachloroplatinate (IV) precursor, the effect of Pt loading on CuO/Al_2O_3 (C) sorbents with 30 wt% Cu was examined. Figures 3.15–3.18 showed that Pt addition generally led to increased breakthrough capacity and total adsorption capacity. These trends, as summarized in Figure 3.19, were due to improved sorbent regeneration efficiency, especially at lower temperatures where sulfate decomposition would have been more challenging. The increase in SO_2 desorption rate with Pt loading also allowed for faster completion of the sorbent regeneration process. At 400°C, over 70 min were required to regenerate CuO/Al_2O_3 (C), while only 30 min and 20 min were needed to regenerate sorbents loaded with 0.1 wt% and 1 wt% Pt, respectively (see Figure 3.20). In fact, at a higher Pt loading of 5 wt%, the sulfate removal process was so efficient that the sorbent could be operated as a SO_x trap at temperatures as low as 350°C.

The addition of Pt, however, led to increased rate of SO_2 oxidation to SO_3 during the adsorption part of the cycle. At a Pt loading of 0.1 wt%, a steady-state SO_2 to SO_3 conversion of 40% was observed at 400°C; whereas almost complete SO_2 oxidation

could be obtained with 1 wt% of Pt loading. Since the SO_3 formation rate increased with SO_x coverage, minimal SO_3 slip would be expected before the sorbent's breakthrough capacity was reached. As a result, SO_2 concentration measured downstream of the SO_x traps during the second adsorption cycle would rise to a maximum value before gradually falling down to the steady-state value.

During the regeneration process, the presence of Pt also promoted the direct SO_2 reduction by CO over CuO/Al_2O_3 (C) at 450°C. This reaction resulted in the deposition of elemental sulfur, which could be easily converted back to SO_2 with oxygen during the initial part of the adsorption cycle, thereby causing undesirable SO_2 slip. Complete SO_2 reduction was observed at 450°C over all nanocomposites with > 1 wt% Pt.

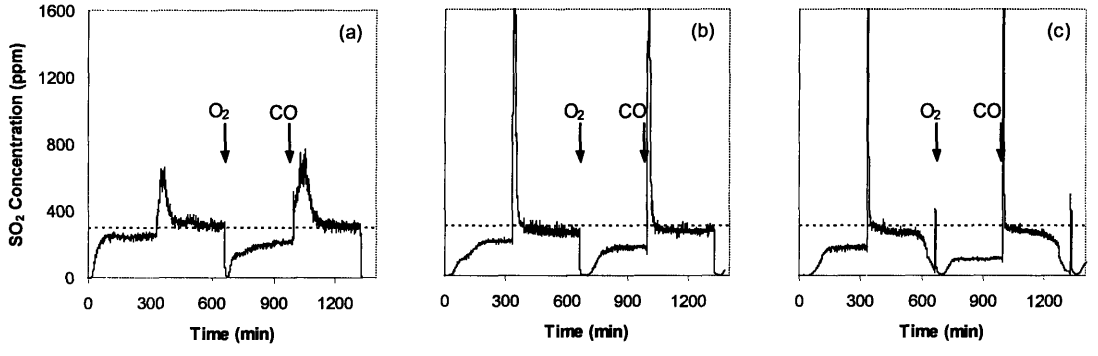

Figure 3.15. SO_2 concentration downstream of CuO/Al_2O_3 (C) sorbent with 30 wt% Cu and 0.1 wt% Pt during the first and second isothermal cycles at (a) 350°C, (b) 400°C and (c) 450°C. The reactions were run at a space velocity of 80,000 h^{-1} with 300 ppm SO_2, and alternating pulses of 0.5% O_2 for adsorption and 1% CO for desorption.

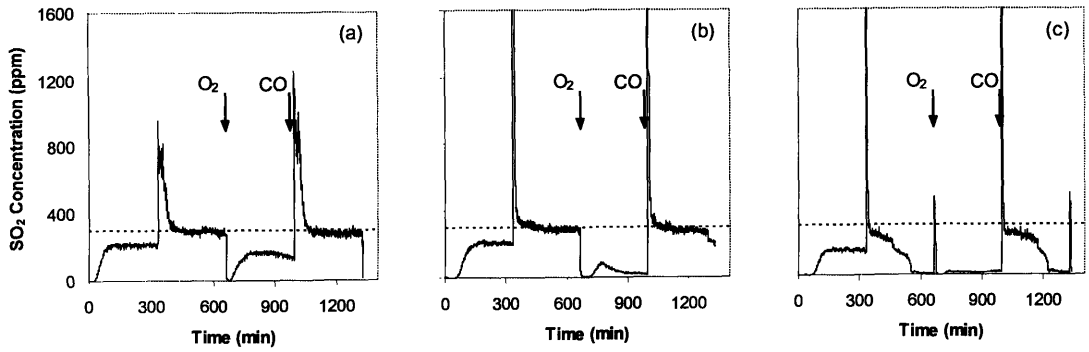

Figure 3.16. SO_2 concentration downstream of CuO/Al_2O_3 (C) sorbent with 30 wt% Cu and 1 wt% Pt during the first and second isothermal cycles at (a) 350°C, (b) 400°C and (c) 450°C. The reactions were run at a space velocity of 80,000 h^{-1} with 300 ppm SO_2, and alternating pulses of 0.5% O_2 for adsorption and 1% CO for desorption.

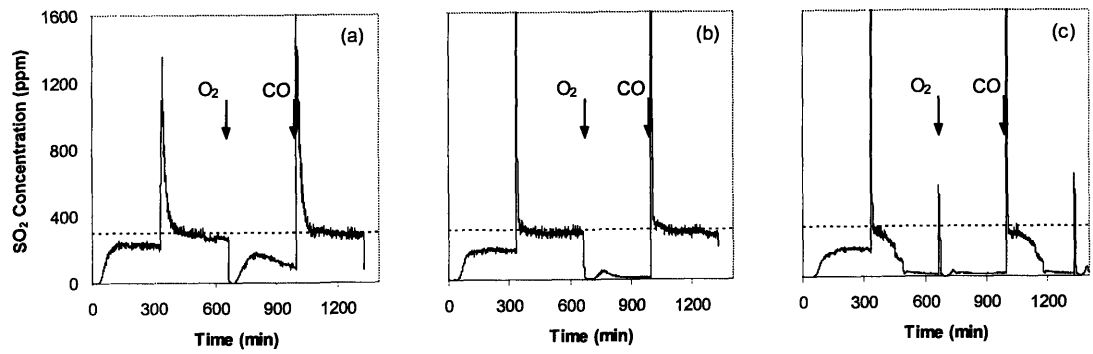

Figure 3.17. SO_2 concentration downstream of CuO/Al_2O_3 (C) sorbent with 30 wt% Cu and 2 wt% Pt during the first and second isothermal cycles at (a) 350°C, (b) 400°C and (c) 450°C. The reactions were run at a space velocity of 80,000 h^{-1} with 300 ppm SO_2, and alternating pulses of 0.5% O_2 for adsorption and 1% CO for desorption.

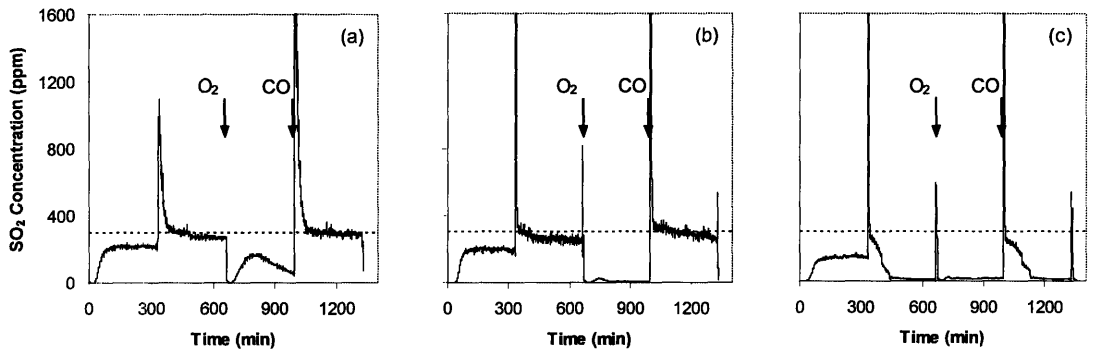

Figure 3.18. SO_2 concentration downstream of CuO/Al_2O_3 (C) sorbent with 30 wt% Cu and 5 wt% Pt during the first and second isothermal cycles at (a) 350°C, (b) 400°C and (c) 450°C. The reactions were run at a space velocity of 80,000 h^{-1} with 300 ppm SO_2, and alternating pulses of 0.5% O_2 for adsorption and 1% CO for desorption.

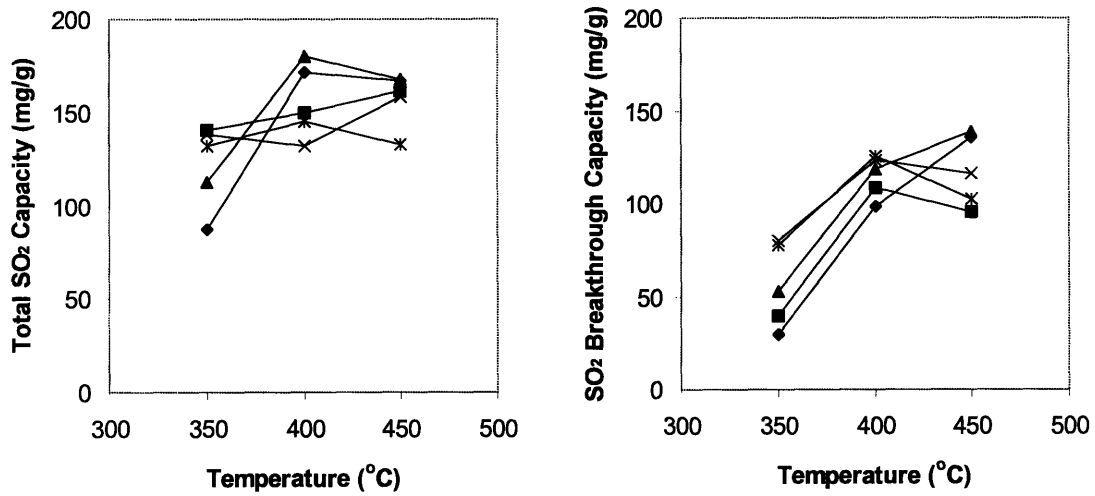

Figure 3.19. SO_2 breakthrough capacity and total adsorption capacity of CuO/Al_2O_3 (C) sorbents with 30 wt% Cu and (♦) 0 wt%, (■) 0.1 wt%, (▲) 1 wt%, (×) 2 wt% and (*) 5 wt% Pt during the second isothermal adsorption cycle at 400°C. The reactions were run at a space velocity of 80,000 h^{-1} with 300 ppm SO_2, and 0.5% O_2 for adsorption and 1% CO for desorption.

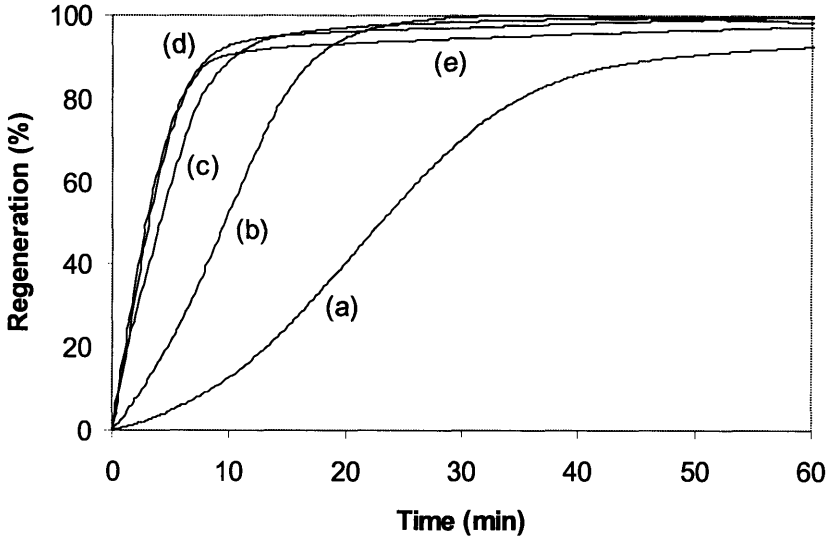

Figure 3.20. Regeneration efficiency of CuO/Al_2O_3 (C) sorbents with 30 wt% Cu and (a) 0 wt%, (b) 0.1 wt%, (c) 1 wt%, (d) 2 wt% and (e) 5 wt% Pt during the second isothermal adsorption cycle at 400°C. The reactions were run at a space velocity of 80,000 h^{-1} with 300 ppm SO_2, and 0.5% O_2 for adsorption and 1% CO for desorption.

3.3.3.3. Transient SO_2 Adsorption/Desorption

The transient SO_2 adsorption/desorption activities of CuO/Al_2O_3 with 30 wt% Cu and various Pt loadings were measured over periodic lean/rich cycles with 20-min O_2 pulses and 40-min CO pulses at 400°C. Figure 3.21 showed that a small addition of Pt could bring about dramatic improvement in the performance of the SO_x trap. In fact, the presence of only 0.1 wt% Pt was sufficient to allow the SO_x-loaded CuO/Al_2O_3 sorbent to be completely regenerated under the operating conditions, which kept the CuO conversion below 15% (Figure 3.22). Figure 3.23 further illustrates that the average SO_2 concentrations measured downstream of the various Pt-loaded SO_x traps were all stable over 23 adsorption cycles. Faster sorbent regeneration could be achieved with higher Pt loadings, despite some increases in the formation of SO_3 and sulfur. However, prolonged exposure to SO_2 under reducing condition led to deterioration of the sorbent performance. Figure 3.24 shows that longer CO pretreatment brought about faster deactivation of the Pt-loaded CuO/Al_2O_3, possibly as a result of sulfide formation [20,28]. Therefore, the optimal sorbent composition should provide a balance between efficient regeneration and minimal side-reactions. The optimal sorbent performance would also depend on the rate

of SO_2 introduction, as well as the composition and operating temperature of the exhaust stream.

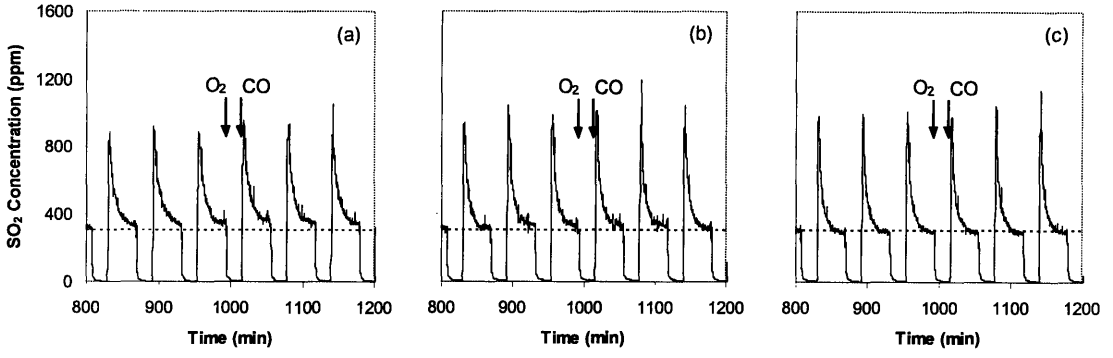

Figure 3.21. SO_2 adsorption/desorption profile of CuO/Al_2O_3 sorbents with 30 wt% Cu and (a) 0.1 wt%, (b) 1 wt% and (c) 5 wt% Pt at 400°C. The reactions were run at a space velocity of 80,000 h^{-1} with 300 ppm SO_2, and alternating pulses of 0.5% O_2 for 20 min and 1% CO for 40 min.

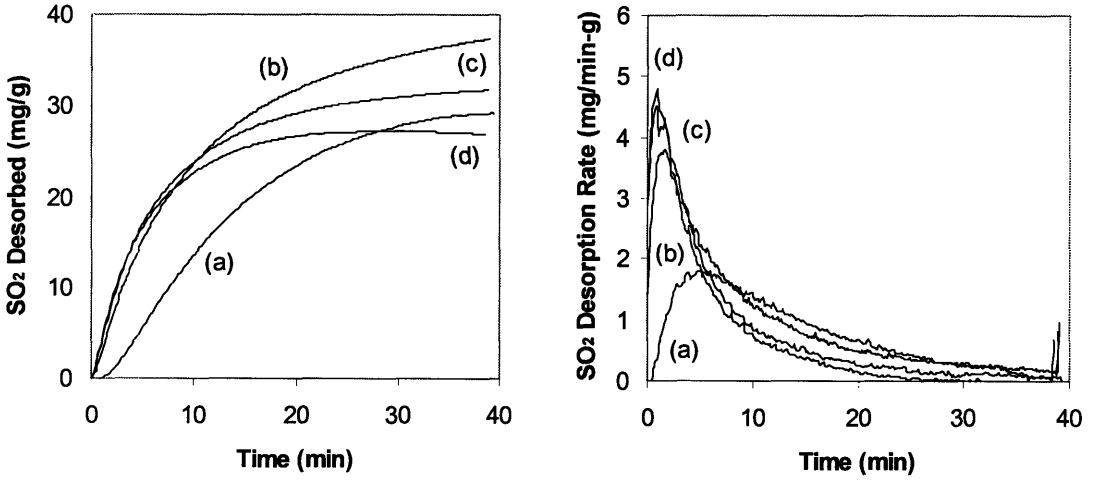

Figure 3.22. Cumulative SO_2 release profile and average SO_2 desorption rate of CuO/Al_2O_3 sorbents with 30 wt% Cu and (a) 0 wt%, (b) 0.1 wt%, (c) 1 wt% and (d) 5 wt% Pt at 400°C. The reactions were run at a space velocity of 80,000 h^{-1} with 300 ppm SO_2, and alternating pulses of 0.5% O_2 for 20 min and 1% CO for 40 min.

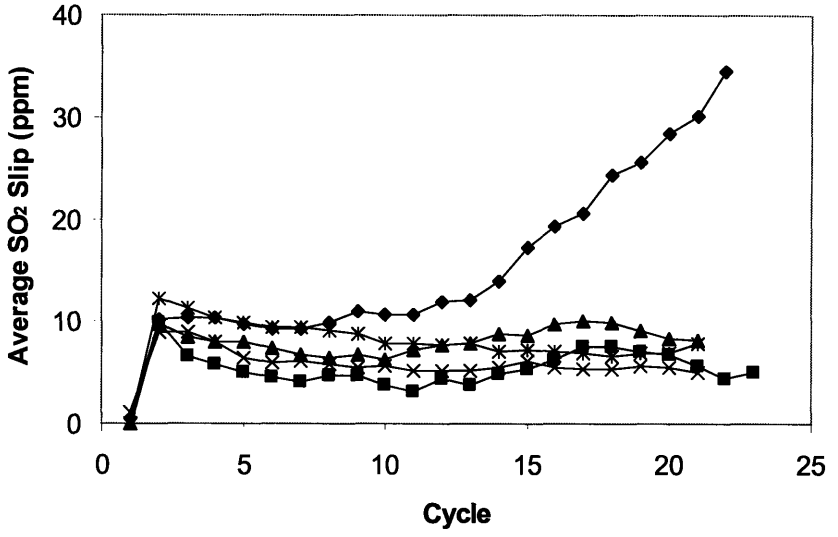

Figure 3.23. Average SO_2 concentration detected downstream of CuO/Al_2O_3 sorbents with 30 wt% Cu and (♦) 0 wt%, (■) 0.1 wt%, (▲) 1 wt%, (×) 2 wt% and (*) 5 wt% Pt during the adsorption cycle at 400°C. The reactions were run at a space velocity of 80,000 h^{-1} with 300 ppm SO_2, and alternating pulses of 0.5% O_2 for 20 min and 1% CO for 40 min.

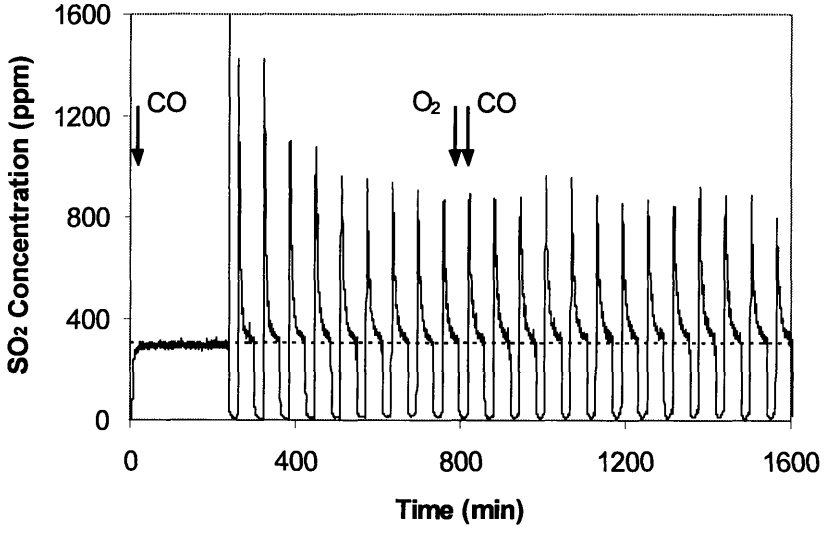

Figure 3.24. SO_2 concentration downstream of CuO/Al_2O_3 sorbent with 30 wt% Cu and 1 wt% Pt at 400°C. The reactions were run at a space velocity of 80,000 h^{-1} with 300 ppm SO_2; following 4 hours of CO treatment, alternating pulses of 0.5% O_2 for 20 min and 1% CO for 40 min were introduced.

3.3.4. Kinetic Studies of Sorbent Regeneration

To examine the role of Pt on the sulfate decomposition by CO, the apparent kinetic rate orders at 400°C and the SO_2 desorption activation energies were measured for the Pt-loaded CuO/Al_2O_3 sorbents (see Table 3.3). In the absence of Pt, the initial rate of SO_2 desorption increased with increasing CO concentration, but was unaffected by the amount of SO_2 loaded, suggesting that the sorbent surface was largely covered by chemisorbed sulfate species. With Pt loading, a significantly higher reaction order with respect to adsorbed SO_2 was noted together with a slight increase in the CO rate order, indicating an increase in CO adsorption relative to SO_2 adsorption. The activation energy for SO_2 desorption remained at ~ 100 kJ/mol when Pt was introduced into the nanocomposite, illustrating that the rate-limiting step of this sorbent regeneration process was not significantly altered by the presence of a small amount of Pt. This was consistent with the idea that Pt promoted the SO_2 desorption by providing sites for CO adsorption, thereby increasing the concentration of adsorbed CO on the sorbent surface.

Table 3.3. Kinetic parameters for SO_2 desorption over Pt-loaded CuO/Al_2O_3 sorbents with 30 wt% Cu.

Pt Loading (wt%)	Reaction Order with Respect to SO_4^{2-} [a]	Reaction Order with Respect to CO [b]	Activation Energy [c] (kJ/mol)
0.0	0.0	0.6	105
0.1	0.5	0.7	102
1.0	0.5	0.8	94

[a] The reactions were run at a space velocity of 80,000 h^{-1} at 400°C with 300 ppm SO_2, and alternating pulses of 0.5% O_2 for 10–30 min and 1% CO at a lean/rich cycle ratio = 0.5.
[b] The reactions were run at a space velocity of 80,000 h^{-1} at 400°C with 300 ppm SO_2, and alternating pulses of 0.5% O_2 for 20 min and 1–6.7% CO for 40 min.
[c] Activation energies were estimated at a space velocity of 80,000 h^{-1} and 350–450°C with 300 ppm SO_2, and alternating pulses of 0.5% O_2 for 330 min and 1% CO for 330 min.

3.3.5. SO_2 TPD Studies

Apart from studying the rates of SO_2 desorption, it is also of practical importance to examine the stability of adsorbed sulfate species on the Pt-loaded CuO/Al_2O_3 nanocomposites. This would allow us to identify the optimal temperature range of

operation, whereby the adsorbed sulfate would decompose sufficiently fast to facilitate the sorbent regeneration process, and yet be stable enough to prevent formation of elemental sulfur. The sulfate decomposition temperatures over the Pt-loaded sorbents were measured in the TPD experiments with CO as the reducing agent. Figure 3.25 shows that the SO_2 desorption temperature was lowered from 420°C for CuO/Al_2O_3 to 350°C for the 5 wt% Pt-loaded sorbent. Since this decrease in desorption temperature coincided with the appearance of a Cu-Pt mixed phase (see Figure 3.26), the incorporation of Pt into the CuO lattice was proposed to be responsible for reducing the stability of adsorbed sulfate species. We further noted that the onset of the SO_2 TPD profiles was consistent with the efficient sorbent regeneration observed in Figures 3.15–3.18. Also, the temperature that corresponded to a complete desorption process seemed to match the onset temperature for sulfur formation. Thus, Pt addition could be used to alter the optimal operating temperature of the SO_x trap.

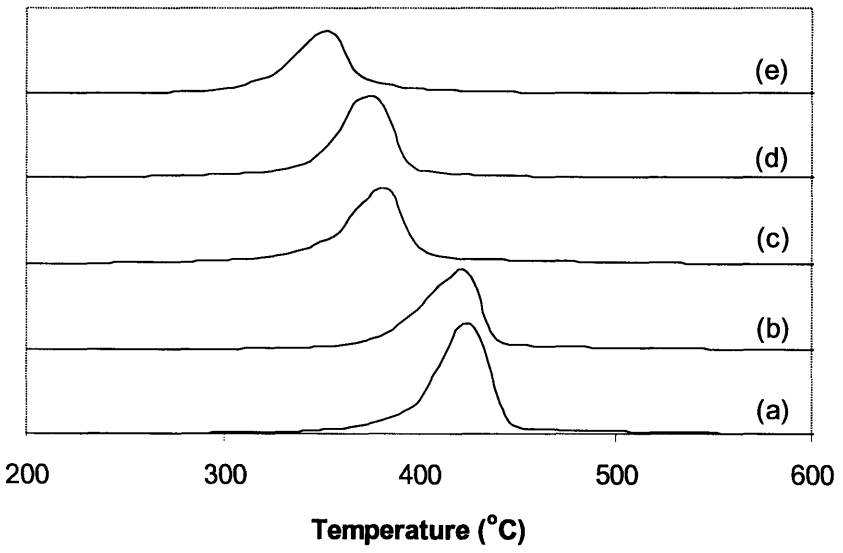

Figure 3.25. TPD profiles of SO_2 for CuO/Al_2O_3 sorbents with 30 wt% Cu and (a) 0 wt%, (b) 0.1 wt%, (c) 1 wt%, (d) 2 wt% and (e) 5 wt% Pt. 0.04 g of sorbent was pretreated in a flow of 1% SO_2 and 2% O_2 in He at 400°C for 2 hours. Desorption was performed at a heating rate of 2°C/min in a 100 cm^3/min flow of 1% CO in He, with 0.25% Ar as the internal standard.

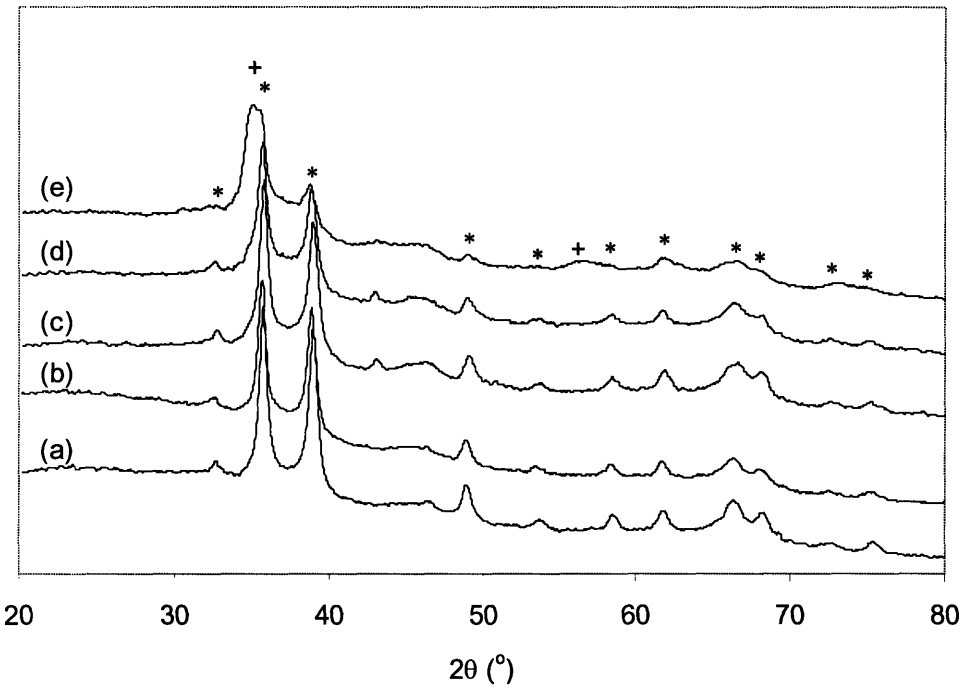

Figure 3.26. XRD patterns of CuO/Al_2O_3 sorbents with 30 wt% Cu and (a) 0 wt%, (b) 0.1 wt%, (c) 1 wt%, (d) 2 wt% and (e) 5 wt% Pt. Phases present included (*) CuO and (+) $Cu_{0.8}Pt_{0.2}O$.

3.3.6. Sorbent Characterization

The XRD patterns of Pt-loaded CuO/Al_2O_3 nanocomposites calcined to 500°C are shown in Figure 3.26. The CuO/Al_2O_3 sorbent with 0.1 wt% Pt only displayed CuO peaks, indicating that its Pt species were well dispersed. As the Pt loading was increased, the high Pt dispersion was maintained, and $Cu_{0.8}Pt_{0.2}O$ peaks were not noted except in the sample containing a high Pt loading of 5 wt%. Depending on the Pt content, the metal oxides present on the CuO/Al_2O_3 sorbent were expected to be converted into $CuSO_4$ during SO_2 adsorption, before subsequent reduction to Cu and Cu-Pt species upon CO exposure.

The sorbents' structural evolution through 1 hour of SO_2 adsorption, followed by 2 hours of CO reduction is illustrated in Figures 3.27 and 3.28, respectively; the grain sizes of various Cu species are summarized in Table 3.4. After SO_2 adsorption, no bulk $CuSO_4$ phase was observed, indicating that the sulfate was well distributed over the surface of all sorbents examined. The presence of Pt, however, led to the appearance of

CuS crystal in the oxidizing atmosphere. The formation of these phases could be avoided with the introduction of Rh (see Figure 3.29). During sorbent regeneration, these sulfides were reduced along with sulfate and unreacted CuO to Cu_2O and metallic species. Apart from SO_2 desorption, such phase transformation also brought about the growth of Cu grains as the surface Cu atoms were appreciably mobile at 400°C [29].

Table 3.5 shows that the BET surface areas of the Pt-loaded sorbents were much smaller than that of CuO/Al_2O_3 with 30 wt% Cu due to some pore blockage by Pt, which also decreased the pore size and volume of the sorbents.

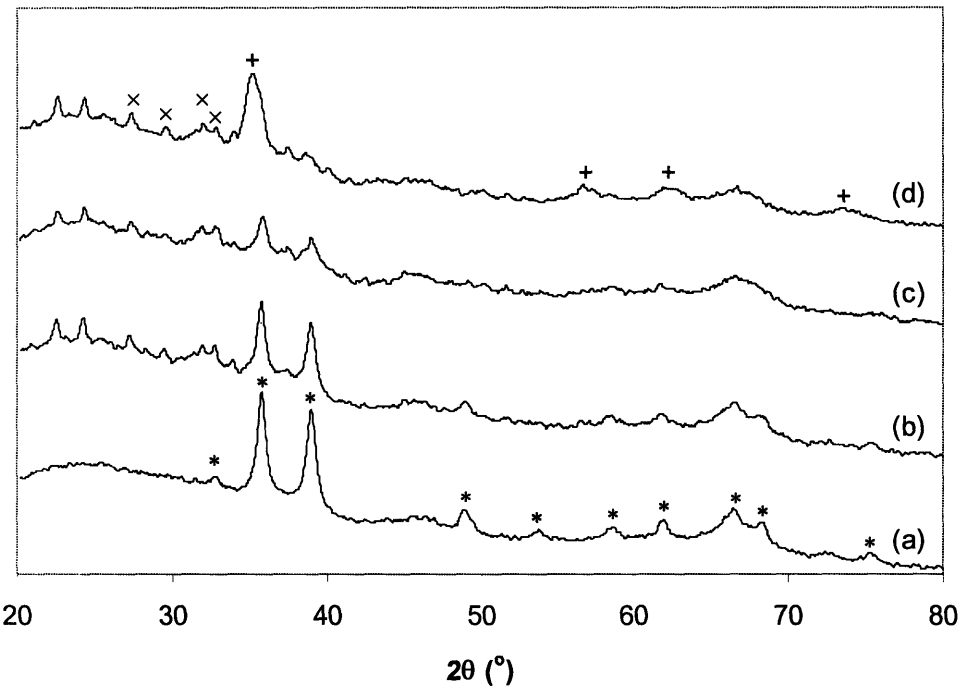

Figure 3.27. XRD patterns of CuO/Al_2O_3 sorbents with 30 wt% Cu and (a) 0 wt%, (b) 0.1 wt%, (c) 1 wt% and (d) 5 wt% Pt after 1 hour of SO_2 adsorption at 400°C. The reactions were run at a space velocity of 80,000 h^{-1} with 300 ppm SO_2 and 0.5% O_2. Phases present included (*) CuO, (+) $Cu_{0.8}Pt_{0.2}O$, and (×) CuS.

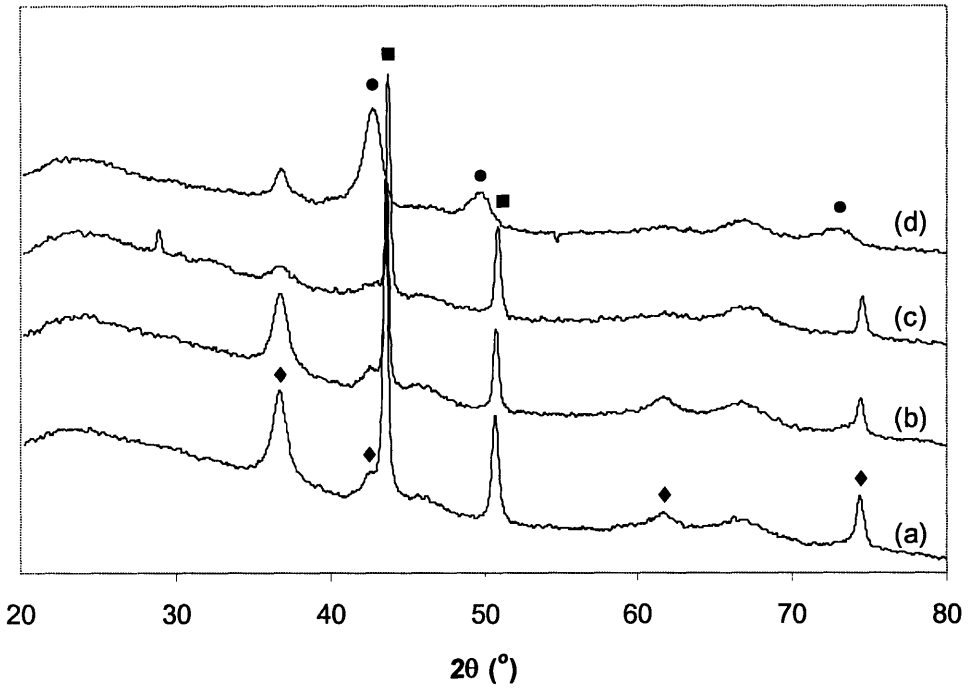

Figure 3.28. XRD patterns of CuO/Al_2O_3 sorbents with 30 wt% Cu and (a) 0 wt%, (b) 0.1 wt%, (c) 1 wt% and (d) 5 wt% Pt after 1 hour of SO_2 adsorption, followed by 2 hours of regeneration at 400°C. The reactions were run at a space velocity of 80,000 h^{-1} with 300 ppm SO_2 and 0.5% O_2 for adsorption, followed by 300 ppm SO_2 and 1% CO for desorption. Phases present included (♦) Cu_2O, (■) Cu, and (●) Cu_3Pt.

Table 3.4. Evolution of Cu species in the Pt-loaded CuO/Al_2O_3 sorbents with a fresh CuO grain size of 16 nm during SO_2 adsorption and regeneration.

Pt Loading (wt%)	Condition[a]	CuO Grain Size (nm)	Cu_2O Grain Size (nm)	Cu Grain Size (nm)
0.0	Aged	16		
	Regenerated		8	31
0.1	Aged	15		
	Regenerated		8	38
1.0	Aged	13		
	Regenerated		5	37

[a] The reactions were run at a space velocity of 80,000 h^{-1} at 400°C with 300 ppm SO_2 and 0.5% O_2 for 60 min for adsorption, followed by 300 ppm SO_2 and 1% CO for 120 min for regeneration.

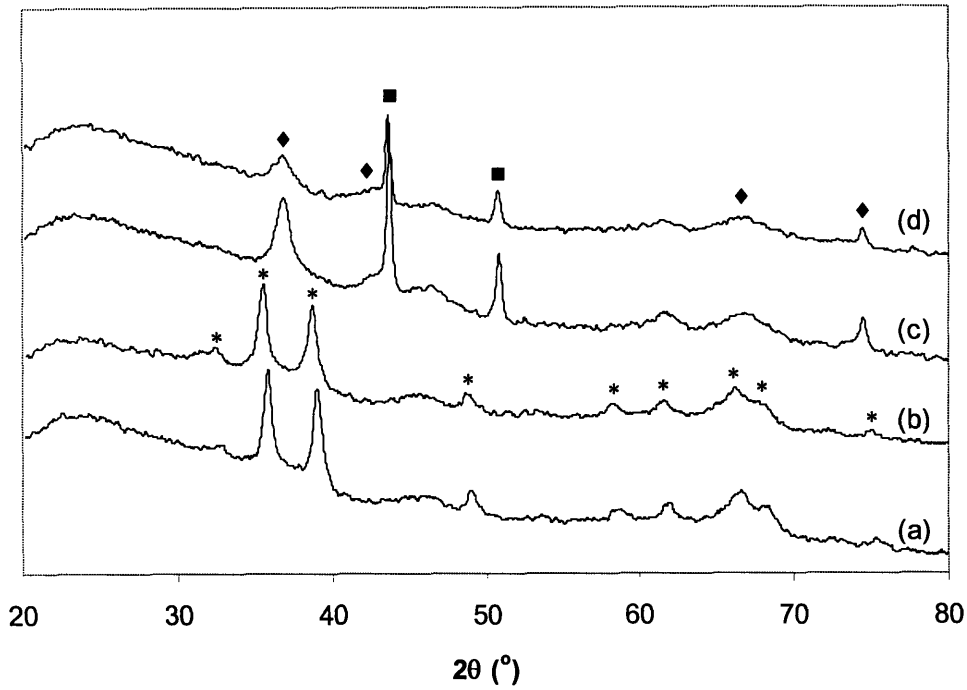

Figure 3.29. XRD patterns of CuO/Al_2O_3 sorbents with 30 wt% Cu, 1 wt% Rh, and (a,c) 0.1 wt% and (b,d) 1 wt% Pt: (a,b) after 1 hour of SO_2 adsorption, (c,d) followed by 2 hours of regeneration at 400°C. The reactions were run at a space velocity of 80,000 h^{-1} with 300 ppm SO_2 and 0.5% O_2 for adsorption, followed by 300 ppm SO_2 and 1% CO for desorption. Phases present included (*) CuO, (♦) Cu_2O, and (■) Cu.

Table 3.5. BET surface area, pore volume and pore diameter of the Pt-loaded CuO/Al_2O_3 sorbents with 30 wt% Cu.

Pt Loading (wt%)	Surface Area (m^2/g)	Pore Volume (cm^3/g)	Pore Diameter (nm)
0.0	238	1.04	13.0
0.1	171	0.60	10.4
1.0	171	0.48	8.7
2.0	152	0.54	10.0
5.0	138	0.46	10.2

3.3.7. Noble Metal-Loaded CuO/Al_2O_3 Nanocomposites

To study the effect of Rh addition on the transient SO_2 adsorption/desorption activities, the SO_2 concentration downstream of the noble metal-loaded CuO/Al_2O_3

sorbents was measured over periodic lean/rich cycles with 20-min O_2 pulses and 40-min CO pulses at 400°C. Comparing Figure 3.30 with Figure 3.21 showed that the incorporation of 1 wt% Rh into the Pt-loaded sorbents led to increased SO_2 desorption rates. In fact, initial desorption rates as high as ~ 8 mg/min·g were obtained over all sorbents regardless of their Pt loading (see Figure 3.31). This was surprising given that 0.1 wt% Rh loading by itself had a negligible impact on the regenerability of CuO/Al_2O_3 (see Figure 3.32). Therefore, the improved SO_2 desorption observed with higher Rh loading was unlikely associated with enhanced CO adsorption. The initial desorption rate increase in the presence of sufficient Rh might be due to the suppression of crystalline sulfides, which would otherwise be very difficult to reduce under CO. Other researchers have also reported that Rh improved the regenerability of NO_x catalysts in sulfur deactivation studies [20,28].

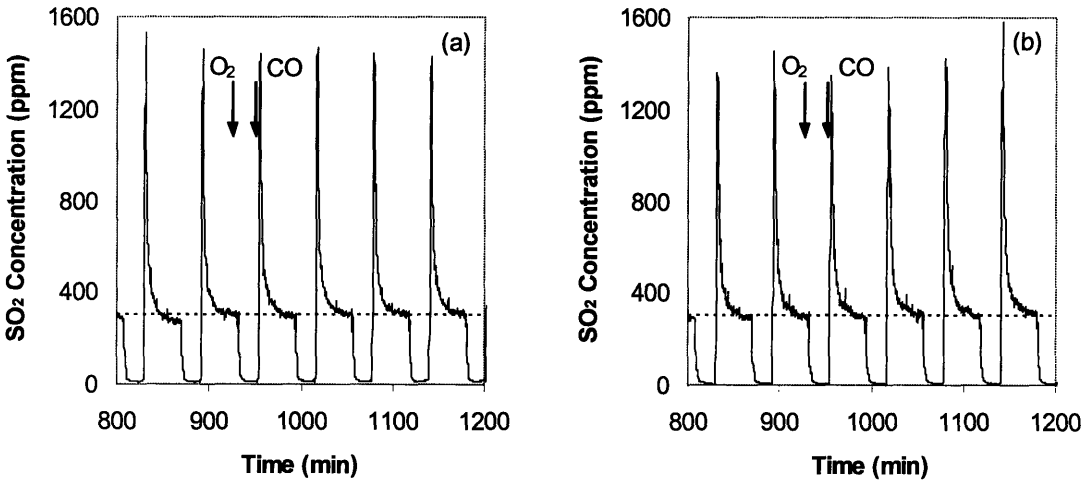

Figure 3.30. Effect of 1 wt% Rh addition on the SO_2 adsorption/desorption profiles of CuO/Al_2O_3 sorbents with 30 wt% Cu and (a) 0.1 wt% and (b) 1 wt% Pt at 400°C. The reactions were run at a space velocity of 80,000 h^{-1} with 300 ppm SO_2, and alternating pulses of 0.5% O_2 for 20 min and 1% CO for 40 min.

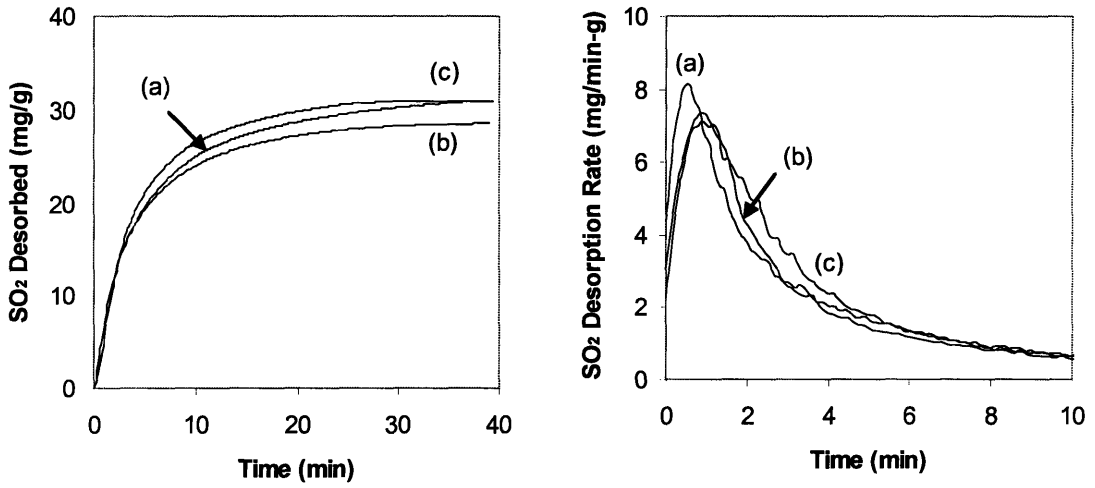

Figure 3.31. Effect of 1 wt% Rh addition on the cumulative SO_2 release profile and average SO_2 desorption rate for CuO/Al_2O_3 sorbents with 30 wt% Cu and (a) 0 wt%, (b) 0.1 wt% and (c) 1 wt% Pt at 400°C. The reactions were run at a space velocity of 80,000 h^{-1} with 300 ppm SO_2, and alternating pulses of 0.5% O_2 for 20 min and 1% CO for 40 min.

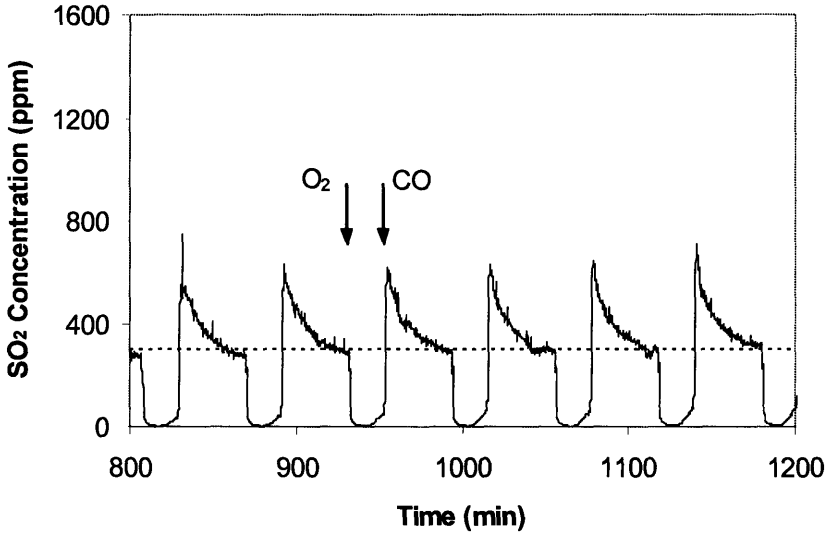

Figure 3.32. Effect of 0.1 wt% Rh addition on the SO_2 adsorption/desorption profile of CuO/Al_2O_3 sorbent with 30 wt% Cu at 400°C. The reactions were run at a space velocity of 80,000 h^{-1} with 300 ppm SO_2, and alternating pulses of 0.5% O_2 for 20 min and 1% CO for 40 min.

Addition of Rh also lowered the stability of sulfate stored in the sorbents and increased the sorbents' reducibility by CO, which further enhanced sulfate

decomposition. This was clearly illustrated in Figure 3.33, where SO_2 reduction to elemental sulfur was observed over the CuO/Al_2O_3 sorbent with 0.1 wt% Pt and 1 wt% Rh during 4 hours of operation under a reducing atmosphere at 400°C. In contrast, less SO_2 reduction to elemental sulfur was observed over the sorbent with 0.1 wt% Pt even at 450°C (Figure 3.15). With the co-loading of 0.1 wt% Pt and 1 wt% Rh, the CuO/Al_2O_3 sorbent maintained an average SO_2 slip of only 8 ppm over each adsorption cycle even after 4 hours of CO treatment. This demonstrated that Rh incorporation also improved the sorbent stability under transient studies.

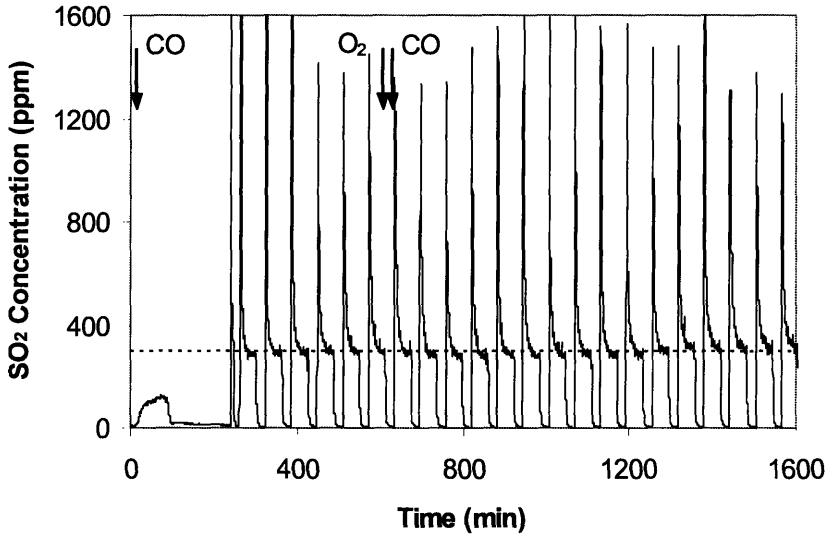

Figure 3.33. SO_2 concentration downstream of CuO/Al_2O_3 sorbent with 30 wt% Cu, 0.1 wt% Pt and 1 wt% Rh at 400°C. The reactions were run at a space velocity of 80,000 h^{-1} with 300 ppm SO_2; following 4 hours of CO treatment, alternating pulses of 0.5% O_2 for 20 min and 1% CO for 40 min were introduced.

Despite providing for rapid SO_2 desorption, Rh-loaded sorbents that did not contain Pt performed inadequately in transient adsorption/desorption studies due to their early SO_2 breakthrough. The extent of the SO_2 slip increased with the Rh loading (Figure 3.34). Since the reducibility of CuO/Al_2O_3 sorbent increased with Rh addition, the oxidation activity was expected to decrease. As sulfate formation proceeded via the reaction between SO_3 and the sorbent, this lowering of SO_2 oxidation activity could lead to poor SO_x adsorption and early SO_2 slip. Excessive sulfur formation could also give

rise to prematured saturation of the SO_x trap as this sulfur would be converted back into SO_2 at the next adsorption cycle. This lost of SO_2 capacity was evident in Figure 3.35 during the second adsorption cycle, whereby SO_2 production increased with Rh loading. Therefore, Pt was needed to maintain SO_2 adsorption capacity over a complete transient operation cycle. The complementary role of Rh and Pt had also been reported by Amberntsson *et al.* [20] in their study of Rh-Pt/BaO/Al_2O_3 catalyst. Under SO_2 exposure, Rh/BaO/Al_2O_3 lost its NO oxidation function but retained good NO_x reduction activity, while the opposite behavior was observed for the sample containing only Pt.

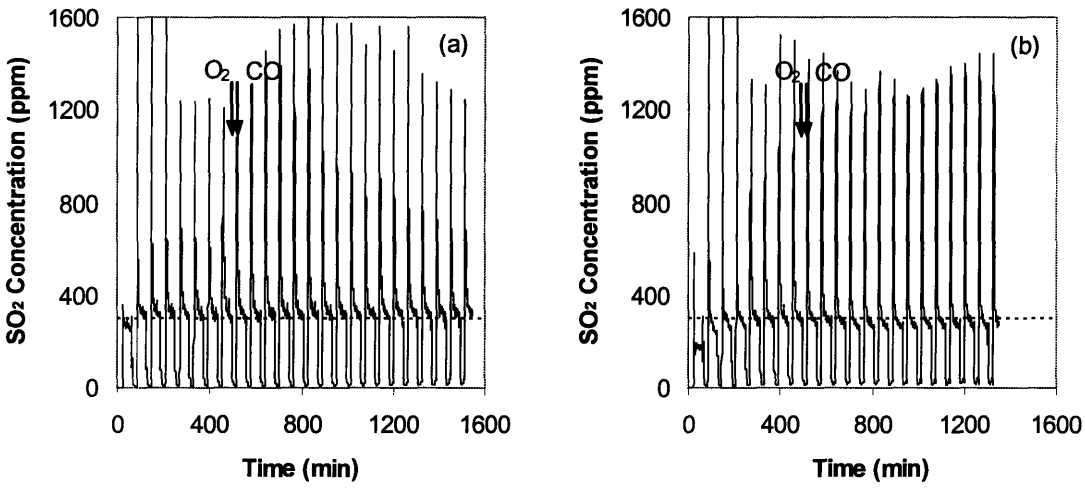

Figure 3.34. SO_2 adsorption/desorption profile of CuO/Al_2O_3 sorbents with 30 wt% Cu and (a) 1 wt% and (b) 5 wt% Rh at 400°C. The reactions were run at a space velocity of 80,000 h^{-1} with 300 ppm SO_2, and alternating pulses of 0.5% O_2 for 20 min and 1% CO for 40 min.

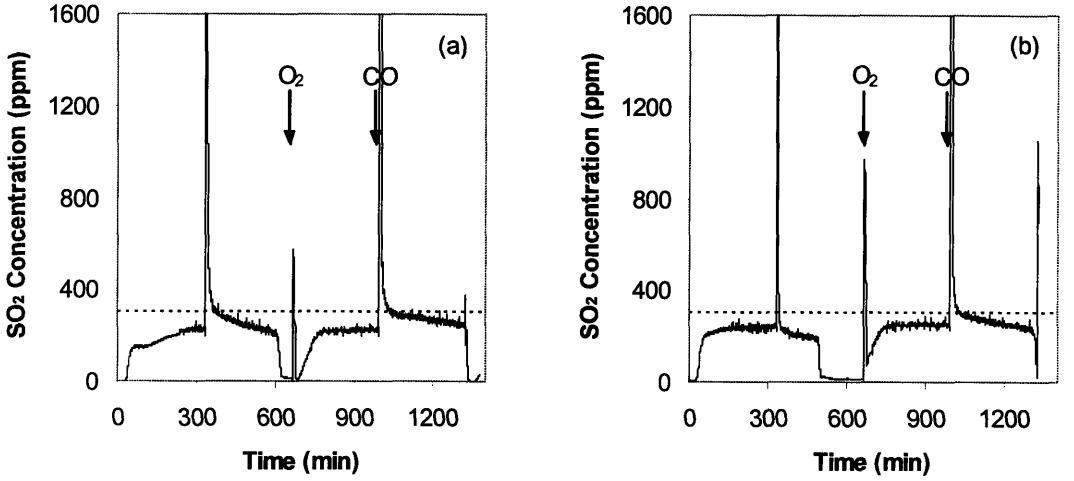

Figure 3.35. SO_2 concentration downstream of CuO/Al_2O_3 sorbents with 30 wt% Cu and (a) 1 wt% and (b) 5 wt% Rh during the first and second isothermal cycles at 400°C. The reactions were run at a space velocity of 80,000 h^{-1} with 300 ppm SO_2 and 0.5% O_2 for adsorption, followed by 300 ppm SO_2 and 1% CO for desorption.

3.4. Summary

Nanocrystalline CuO-based sorbents capable of adsorbing SO_2 in oxygen-rich environment as metal sulfates and releasing SO_2 in reducing atmosphere were successfully synthesized by sequential precipitation. The CuO/Al_2O_3 sorbents prepared by this method exhibited excellent SO_2 adsorption capacity and superior CO regenerability compared with those produced by the impregnation method, due to their higher surface area and better dispersion of Cu species. Over 50 mg of SO_2 could be adsorbed by 1 g of CuO/Al_2O_3 with 30 wt% Cu before SO_2 breakthrough was observed. However, the regeneration process of this sorbent at 400°C was slow and inefficient. The rate of SO_2 desorption from the sorbents could be improved by using either higher CO concentration or operating temperature. However, the use of high temperature led to the undesired decomposition of surface sulfate into elemental sulfur during regeneration, and excessive SO_3 formation in the oxidizing atmosphere.

Chemical enhancement of the SO_2 desorption rate could be achieved through the use of noble metals. With the addition of 0.1 wt% Pt, the CuO/Al_2O_3 sorbent with 30 wt% Cu could be regenerated twice as quickly. On the average, only 8 ppm of SO_2 were detected downstream of this SO_x trap over each adsorption cycle. This improvement in

sorbent regeneration was attributed to better CO adsorption and lower sulfate decomposition temperature as a result of Pt addition. The Pt-loaded CuO/Al_2O_3 nanocomposite remained active even after 24 hours of operation, whereby > 0.9 g of SO_2 had been adsorbed and desorbed from 1 g of sorbent with minimal loss of capacity. The nature of sulfur deactivation for these sorbents was highly dependent on the composition of noble metals used. Sorbents loaded with Pt deteriorated over prolonged exposure to SO_2 under reducing atmosphere, while those that contained only Rh lost their adsorption capacity in the oxygen-rich environment. By using both Rh and Pt, sorbent regeneration rate as well as sorbent stability could be optimized and maintained.

3.5. References

[1] B.I. Bertelsen, Top. Catal. 16/17 (2001) 15.

[2] M. Amiridis, T. Zhang, R.J. Farrauto, Appl. Catal. B 10 (1996) 203.

[3] A. Fritz, V. Pitchon, Appl. Catal. B 13 (1997) 1.

[4] R. Burch, J.P. Breen, F.C. Meunier, Appl. Catal. B 39 (2002) 283.

[5] A. Konig, G. Herding, B. Hupfeld, T. Richter, K. Weidmann, Top. Catal. 16/17 (2001) 23.

[6] B. Westerberg, E. Fridell, J. Mol. Catal. A 165 (2001) 249.

[7] F. Prinetto, G. Ghiotti, I. Nova, L. Lietti, E. Tronconi, P. Forzatti, J. Phys. Chem. B 105 (2001) 12732.

[8] C. Hess, J.H. Lunsford, J. Phys. Chem. B 106 (2002) 6358.

[9] S. Hodjati, P. Bernhardt, C. Petit, V. Pitchon, A. Kiennemann, Appl. Catal. B 19 (1998) 209.

[10] E. Fridell, M. Skoglundh, B. Westerberg, S. Johansson, G. Smedler, J. Catal. 183 (1999) 196.

[11] A. Amberntsson, H. Persson, P. Engstrom, B. Kasemo, Appl. Catal. B 31 (2001) 27.

[12] L. Lietti, P. Forzatti, I. Nova, E. Tranconi, J. Catal. 204 (2001) 175.

[13] N.W. Cant, M.J. Patterson, Catal. Today 73 (2002) 271.

[14] P. Engstrom, A. Amberntsson, M. Skoglundh, E. Fridell, G. Smedler, Appl. Catal. B 22 (1999) L241.

[15] H. Mahzoul, L. Limousy, J.F. Brilhac, P. Gilot, J. Anal. Appl. Pyrolysis 56 (2000) 179.

[16] A. Amberntsson, M. Skoglundh, M. Jonsson, E. Fridell, Catal. Today 73 (2002) 279.

[17] C. Courson, A. Khalfi, H. Mahzoul, S. Hodjati, N. Moral, A. Kiennemann, P. Gilot, Catal. Commun. 3 (2002) 471.

[18] J.T. Sweeney, Novel Metal Oxide Nanocomposites for Oxygen Storage, Sulfur Dioxide Adsorption and Hydrogen Sulfide Absorption, Ph.D. Thesis, Massachusetts Institute of Technology, Cambridge, MA, 2003.

[19] L. Limousy, H. Mahzoul, J.F. Brilhac, P. Gilot, F. Garin, G. Maire, Appl. Catal. B 42 (2003) 237.

[20] A. Amberntsson, M. Skoglundh, S. Ljungstrom, E. Fridell, J. Catal. 217 (2003) 253.

[21] S.G. Deng, Y.S. Lin, Ind. Eng. Chem. Res. 35 (1996) 1429.

[22] K.S. Yoo, S.M. Jeong, S.D. Kim, S.B. Park, Ind. Eng. Chem. Res. 35 (1996) 1543.

[23] S.M. Jeong, S.D. Kim, Ind. Eng. Chem. Res. 36 (1997) 5425.

[24] C. Macken, B.K. Hodnett, Ind. Eng. Chem. Res. 37 (1998) 2611.

[25] C. Macken, G. Paparatto, B.K. Hodnett, Ind. Eng. Chem. Res. 39 (2000) 3868.

[26] C. Orsenigo, L. Lietti, E. Tronconi, P. Forzatti, F. Bregani, Ind. Eng. Chem. Res. 37 (1998) 2350.

[27] S. Iretskaya, M.B. Mitchell, J. Phys. Chem. B 107 (2003) 4955.

[28] N. Shawal Nasri, J.M. Jones, V.A. Dupont, A. Williams, Energ. Fuel 12 (1998) 1130.

[29] C.N. Satterfield, Heterogeneous Catalysis in Industrial Practice, 2nd Edition, Krieger Publishing Company, Florida, 1986, p. 113.

Chapter 4 – Metal Oxide Nanocomposites as SO_x-Tolerant NO_x Traps

4.1. Introduction

Over the past few years, increasing research has been devoted towards developing more effective strategies for automotive nitrogen oxides (NO_x) emissions control to satisfy the new EPA standards due to take effect in 2004 [1]. In particular, NO_x removal from lean-burn and diesel engines presents significant challenges as conventional three-way catalysts are ineffective under an oxygen-rich atmosphere [2-4]. Moreover, the wide range of temperatures and the chemical complexity of gasoline and diesel fuels typically encountered in engine operations make implementation of direct reduction catalysts difficult [4,5].

To address this issue, NO_x storage-reduction (NSR) catalysts have been developed. They allow all the NO_x that have been stored in the form of metal nitrates [6-8] under fuel-lean condition to be released and reduced to nitrogen during the shorter fuel-rich period that follows. However, as the NO_x storage components of these NSR systems are typically alkaline or alkaline earth metal oxides, such as BaO [9-13], the sorbents are easily poisoned by the SO_2 present in the fuel exhaust due to blockage of storage sites with sulfate formation [14-17]. One possible solution is to develop materials that are capable of trapping NO_x and SO_x in an oxygen-rich environment in the form of nitrates and sulfates, and simultaneously releasing both N_2 and SO_2 under the reducing atmosphere, thus preventing the loss of NO_x sorption capacity from sulfur poisoning.

This chapter builds on our previous success in developing $Pt/CuO/Al_2O_3$ nanocomposites as SO_2 sorbents with low regeneration temperatures [18]. It focuses on the NO_x adsorption capability of this class of materials with the aim to create a SO_x-tolerant NO_x trap for automotive applications. Various noble metal-loaded CuO/Al_2O_3 nanocomposites were synthesized and examined for the entrapment of NO and SO_2. MgO was also introduced to the CuO/Al_2O_3 sorbents to improve their NO_x storage capacity. The effects of noble metals and MgO on the NO and SO_2 adsorption capacities and regeneration efficiencies were investigated.

4.2. Experimental

4.2.1. Sorbent Preparation

To achieve high surface area materials with good dispersion of active components, nanocrystalline CuO/Al_2O_3 sorbents were prepared by a sequential chemical precipitation technique. First, an aqueous solution of aluminum nitrate was added to a solution of tetraethylammonium hydroxide to yield an aluminum hydroxide precipitate. After aging for 24 hours, a required amount of copper nitrate solution was added. The suspension was stirred for 24 hours, and the precipitate was centrifuged, washed and dried. CuO/Al_2O_3 was obtained by calcining the powders in air at 500°C for 6 hours. Mixtures of dihydrogen hexachloroplatinate (IV) and rhodium (II) nitrate solutions were impregnated onto the calcined CuO/Al_2O_3. The impregnated materials were calcined at 500°C for 3 hours to produce the noble metal-loaded sorbents.

4.2.2. Sorbent Characterization

Sorbent surface area and pore size distribution were calculated from the nitrogen adsorption isotherm (Micromeritics ASAP 2000) using the BET and BJH methods, respectively. Phase identification was achieved by X-ray diffraction (XRD) with a Siemens D5000 diffractometer using Cu Kα radiation at 45 kV and 40 mA. Scherrer's analysis of X-ray peak broadening was employed to determine crystallite size.

4.2.3. NO Adsorption and Regeneration

The sorbents' NO adsorption and regeneration activities in the presence and absence of SO_2 were studied in a quartz tube fixed-bed reactor under alternate oxidizing and reducing atmospheres. The simulated fuel-lean exhaust consisted of 300 ppm NO, 7% O_2, and either 0 ppm or 60 ppm SO_2 with He as the balance; the fuel-rich exhaust contained 1% CO instead of O_2. With 0.1–0.2 g of sorbents and a total flow rate of 100 cm^3/min, the space velocities for both fuel-lean and fuel-rich streams were ~ 16,000–32,000 h^{-1}. The feed composition and the duration of O_2 and CO pulses were controlled using the National Instruments Lab View in conjunction with solenoid valves to switch between O_2 and CO. The reactor effluent was analyzed with a VG Gas Lab 300 mass

spectrometer. Masses of 28 (CO or N_2), 30 (NO), 32 (O_2), 40 (Ar), 44 (CO_2 or N_2O), 46 (NO_2) and 64 (SO_2) were continuously monitored with a constant feed of 0.18% Ar as the internal reference. A HP 6890 Plus gas chromatograph equipped with a Chromosil 310 column was also used to allow carbon dioxide, carbonyl sulfide, hydrogen sulfide, carbon disulfide and sulfur dioxide to be separated and quantified. No COS, H_2S or CS_2 were detected in this work.

4.2.4. NO Temperature-Programmed Desorption (TPD)

Prior to each NO_x TPD experiment, 0.1 g of catalyst sample was pretreated in a flow of 0.2% NO and 30% O_2 in He at 400°C for 2 hours. After cooling to 50°C, NO_x adsorption was performed by exposing the sample to 0.2% NO and 30% O_2 in He for 2 hours. Desorption of adsorbed species was then performed at a ramp rate of 2°C/min in a He flow of 50 cm^3/min with 0.5% Ar as the internal standard. The effluent gas was analyzed using a HP 6890 Plus gas chromatograph equipped with a HP 5972A mass selective detector.

4.2.5. SO_2 Temperature-Programmed Desorption (TPD)

In a typical SO_2 TPD experiment, adsorption was performed by exposing 0.04 g of sorbent to a flow of 1% SO_2 and 2% O_2 in He at 400°C for 2 hours. After cooling to 200°C, desorption of adsorbed species was performed at a ramp rate of 2°C/min in a 100 cm^3/min flow of 1% CO in He with 0.25% Ar as the internal standard. The reactor effluent was analyzed using a HP 6890 Plus gas chromatograph equipped with a HP 5972A mass selective detector.

4.3. Results and Discussion

4.3.1. Noble Metal-loaded CuO/Al_2O_3 as SO_x-Tolerant NO_x Traps

Nanocrystalline CuO-based sorbents capable of adsorbing SO_2 in oxygen-rich environment as metal sulfates and releasing SO_2 in reducing atmosphere were synthesized by sequential precipitation. As these sorbents exhibited excellent SO_2

adsorption capacity and CO regeneration efficiency at 400°C, they represented a good starting platform for the development of SO_x-tolerant NO_x traps.

To evaluate the potential of the NO_x/SO_x trap idea, it was of interest to compare the effect of SO_2 exposure on the NO_x storage capacity of noble metal-loaded Al_2O_3 with that of the noble metal-loaded CuO/Al_2O_3. In this experiment, the NO outlet concentration downstream of $Pt\text{-}Rh/Al_2O_3$ and $Pt\text{-}Rh/CuO/Al_2O_3$ was measured over periodic lean/rich cycles with 5-min O_2 pulses and 5-min CO pulses at 300°C and 16,000 h^{-1} (see Figures 4.1 and 4.2). The average NO conversion was observed to reduce over one complete cycle. Figure 4.3 shows that while the 1 wt% Pt, 1 wt% Rh/Al_2O_3 exhibited a high initial conversion of 97%, the NO conversion eventually declined to only ~ 60% after the introduction of SO_2 into the feed stream. Since most of the remaining NO conversion took place during the fuel-rich period, the $Pt\text{-}Rh/Al_2O_3$ sorbent was no longer active for NO_x storage in fuel-lean atmosphere. In contrast, the sorbent with 30 wt% Cu was able to maintain its NO conversion at ~ 70% even after 7 hours of operation. The incorporation of CuO facilitated the SO_2 desorption during the fuel-rich period, thus improving the SO_2 resistance of the NO_x trap.

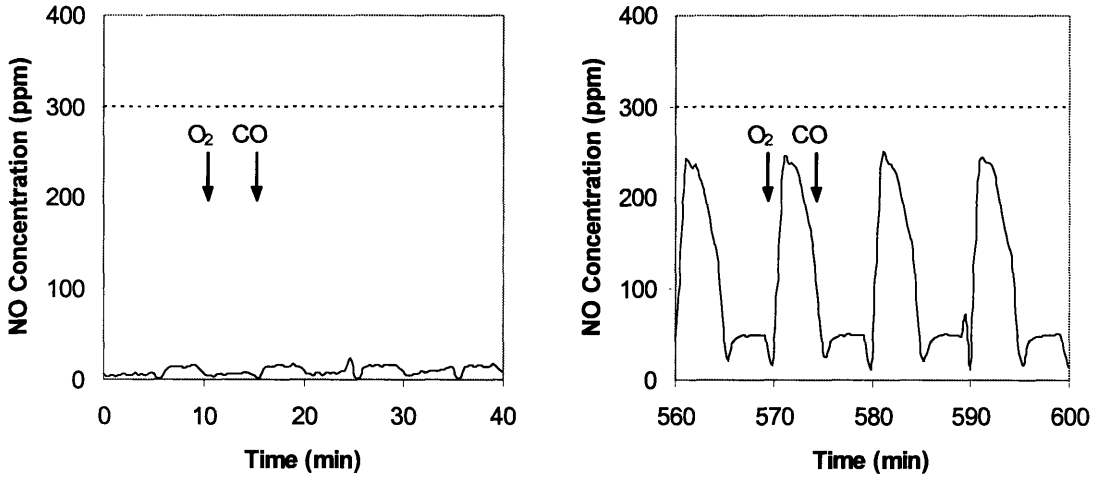

Figure 4.1. Effect of SO_2 exposure on the NO adsorption/desorption profile of the Al_2O_3 sorbent with 1 wt% Pt and 1 wt% Rh at 300°C. The reactions were run at a space velocity of 16,000 h^{-1} with 300 ppm NO, 60 ppm SO_2, and alternating pulses of 7% O_2 for 5 min and 1% CO for 5 min.

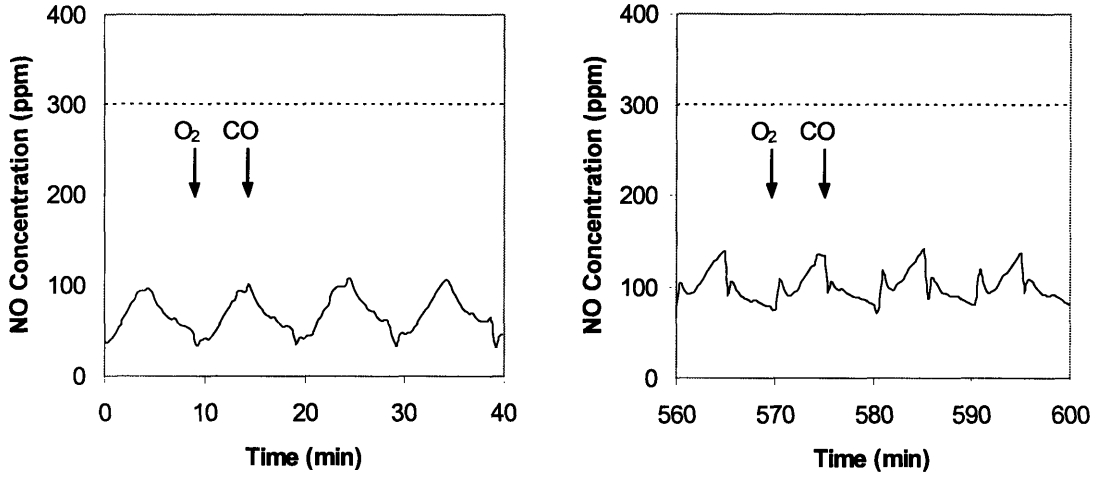

Figure 4.2. Effect of SO_2 exposure on the NO adsorption/desorption profile of CuO/Al_2O_3 sorbent with 30 wt% Cu, 1 wt% Pt and 1 wt% Rh at 300°C. The reactions were run at a space velocity of 16,000 h^{-1} with 300 ppm NO, 60 ppm SO_2, and alternating pulses of 7% O_2 for 5 min and 1% CO for 5 min.

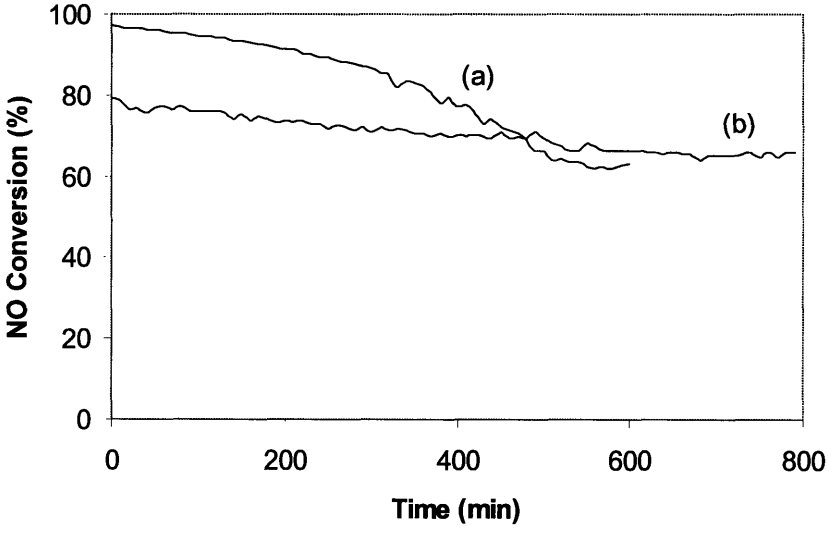

Figure 4.3. Average NO conversion over Al_2O_3 sorbents with (a) 0 wt% and (b) 30 wt% Cu, 1 wt% Pt and 1 wt% Rh during the adsorption/desorption cycles at 300°C. The reactions were run at a space velocity of 16,000 h^{-1} with 300 ppm NO, 60 ppm SO_2, and alternating pulses of 7% O_2 for 5 min and 1% CO for 5 min.

As shown in our previous work on SO_x trap in Chapter 3 [18], the sorbent's resistance against SO_2 poisoning depended on both the sulfate decomposition temperature and the SO_2 desorption rate during the CO regeneration process. Both of these properties

could be easily adjusted with a small addition of noble metals, such as Pt and Rh. For example, the incorporation of 0.1 wt% Pt in CuO/Al_2O_3 allowed the sorbent to be regenerated in half the time required. The improvement in SO_2 desorption with increasing Pt loading translated into more stable NSR performance. Figure 4.4 shows that the Pt-Rh/CuO/Al_2O_3 with 0.1 wt% Pt suffered a much greater loss in NO conversion upon exposure to SO_2 compared with that containing 1 wt% Pt. Despite a superior initial NO conversion of ~ 90%, the sorbent with 0.1 wt% Pt eventually became less active than the sorbent with 1 wt% Pt, which maintained a NO conversion of ~ 70%. The Pt addition could therefore be used to increase the resistance of the NO_x trap against SO_2 poisoning by accelerating the sorbent regeneration under a reducing atmosphere.

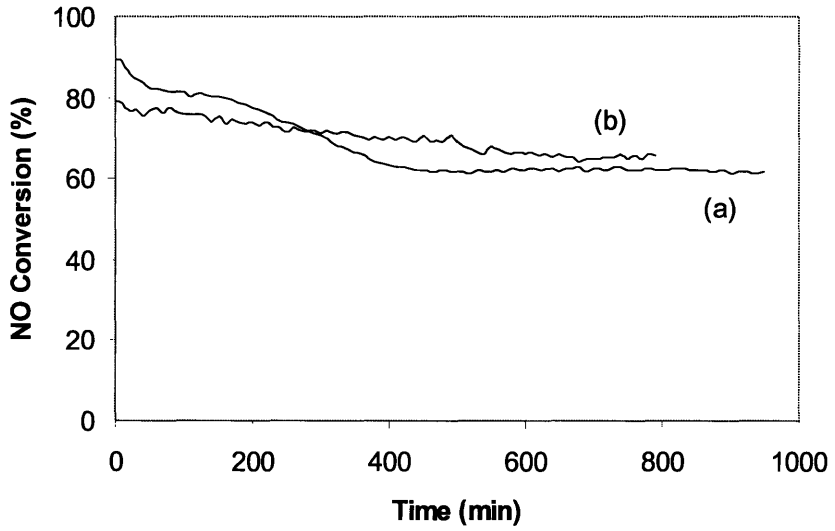

Figure 4.4. Average NO conversion over CuO/Al_2O_3 sorbents with 30 wt% Cu, 1 wt% Rh, and (a) 0.1 wt% and (b) 1 wt% Pt during the adsorption/desorption cycles at 300°C. The reactions were run at a space velocity of 16,000 h^{-1} with 300 ppm NO, 60 ppm SO_2, and alternating pulses of 7% O_2 for 5 min and 1% CO for 5 min.

While faster SO_2 desorption and lower sulfate decomposition temperature were valuable in promoting the SO_2 resistance of the NO_x trap, excessive lowering of the metal sulfate stability would often lead to reduction in the sulfur-free NSR activity of the sorbent. This arose from the decline in NO_x storage capacity at elevated temperatures, which usually accompanied the lowering of metal sulfate stability since most metal nitrates were less stable than their sulfate counterparts. For example, the addition of CuO not only dramatically increased the amount of SO_2 desorbed from Al_2O_3, the presence of

30 wt% Cu also reduced the NO desorption temperature from 400°C to 310°C (see Figure 4.5). This difference in the metal nitrate stability implied that the NO conversion of the noble metal-loaded Al_2O_3 ought to be higher than that of the sorbent loaded with noble metals and CuO. This expected trend in the sulfur-free NO_x performance was in agreement with the initial NSR activities shown in Figure 4.3. Therefore, in order to fully evaluate the sorbent's suitability as a NO_x trap, consideration must also be given to its intrinsic NSR performance, as well as its resistance against SO_2 poisoning.

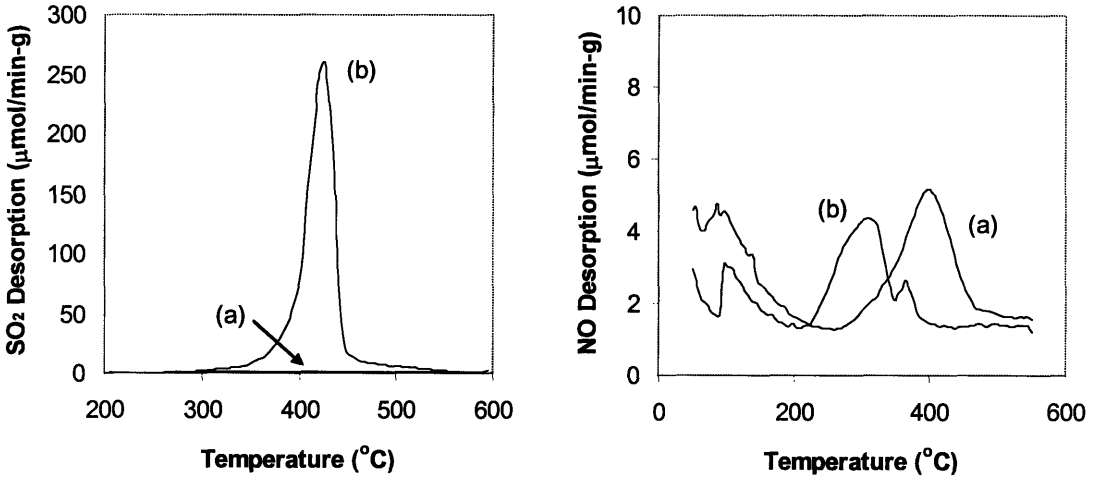

Figure 4.5. TPD profiles of SO_2 and NO for the Al_2O_3 sorbents with (a) 0 wt% and (b) 30 wt% Cu. See Sections 4.2.5 and 4.2.4 for details on SO_2 and NO TPD.

4.3.2. NO_x Storage-Reduction over CuO/Al_2O_3

Since the performance of a NO_x trap depended on both the NO_x storage capacity under oxidizing condition, and the NO reduction activity under reducing atmosphere, the sorbent's NSR activity was expected to depend on the adsorption and catalytic properties of a material. In addition, operating parameters, such as temperature, space velocity and NO concentration, would also affect the NSR performance.

4.3.2.1. Effect of Operating Temperature

The transient NO concentration downstream of CuO/Al_2O_3 with 30 wt% Cu was measured over periodic lean/rich cycles at various temperatures. Figure 4.6 shows that under oxidizing condition, negligible NO was removed from the feed stream at

temperatures above 300°C, indicating that CuO/Al_2O_3 was not an effective NO_x storage material at high temperatures. At lower operating temperatures, however, the initial period during which most NO was retained was longer as more NO_x were stored by the sorbent. This improvement in the NO_x storage capacity was attributed to an increase in metal nitrate stability below 300°C, which was consistent with the NO TPD findings. The stability of adsorbed nitrate species therefore set the upper limit on the operating temperature for the NO_x trap by affecting its NO_x storage capacity.

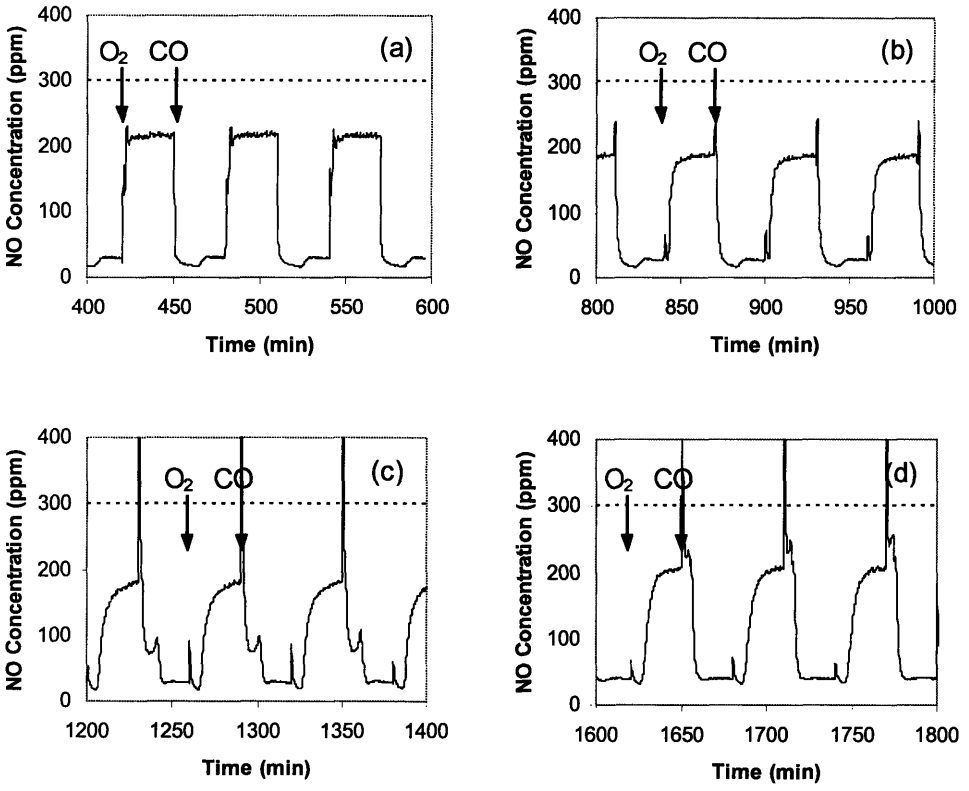

Figure 4.6. NO adsorption/desorption profile of the CuO/Al_2O_3 sorbent with 30 wt% Cu at (a) 350°C, (b) 300°C, (c) 250°C and (d) 200°C. The reactions were run at a space velocity of 16,000 h^{-1} with 300 ppm NO, and alternating pulses of 7% O_2 for 30 min and 1% CO for 30 min.

Once this storage capacity was reached, the NO concentration downstream of the sorbent would gradually increase up to a point of saturation. As this effluent NO concentration was only ~ 200 ppm at the end of each adsorption cycle, significant steady-state conversion of NO to NO_2 must have taken place over CuO/Al_2O_3 at 200–300°C. The NO_2 formation of ~ 33% was significantly lower than the theoretical thermodynamic

prediction of complete NO oxidation, indicating that the adsorbed NO_x species were fairly stable under the oxidizing environment over this range of temperatures.

In the reducing atmosphere, however, the metal nitrates were unstable and rapidly decomposed back to NO. The immediate release of NO_x that followed the introduction of CO allowed the sorbent to be regenerated quickly and efficiently, which further facilitated the long-term stability of the sorbent's NSR performance, even at a relatively low temperature of 200°C. At higher operating temperatures, faster regeneration was achieved due to the smaller amount of NO_x stored. Although this observed trend in the amount of NO desorbed with increasing temperature matched that of the stored NO_x, comparison between these two quantities was difficult as the released NO was constantly being reduced in the presence of CO. In fact, steady-state catalytic NO reduction with high conversions of ~ 90% was seen at all temperatures after the NO desorption from the sorbent. Figure 4.7 shows that the transition between these two regimes always coincided with the decline in CO consumption and CO_2 production. These changes in sorbent characteristics were therefore attributed to phase transformation of CuO to Cu_2O and metallic Cu through reaction with CO, which caused initially the release of adsorbed NO_x species, and eventually the catalytic reduction of NO over the reduced sorbent. This idea was consistent with many findings in the literature that connected the role of reduced Cu species with the catalytic activity for NO_x reduction by CO and hydrocarbons [19].

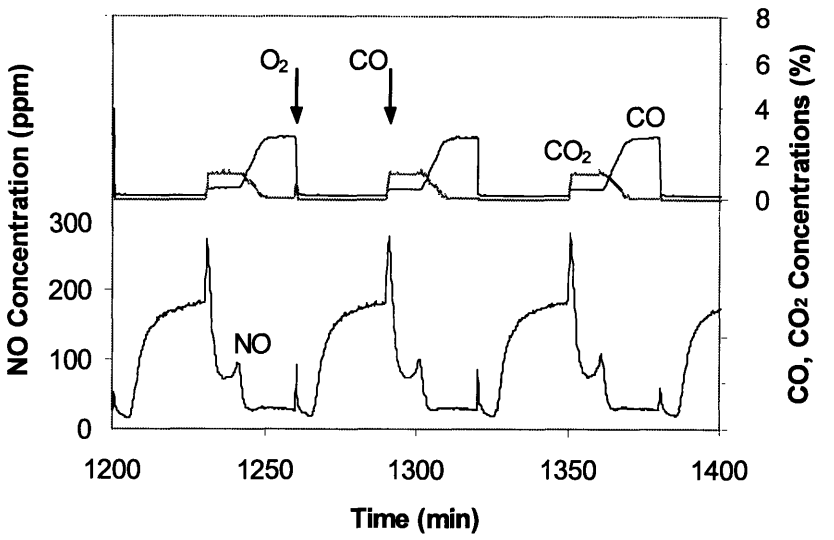

Figure 4.7. NO, CO and CO_2 concentrations downstream of the CuO/Al_2O_3 sorbent with 30 wt% Cu at 250°C. The reactions were run at a space velocity of 16,000 h^{-1} with 300 ppm NO, and alternating pulses of 7% O_2 for 30 min and 1% CO for 30 min.

4.3.2.2. Effect of Pt Addition

Since Pt incorporation in the CuO/Al_2O_3 sorbent was known to improve its SO_2 desorption efficiency by reducing the sulfate stability, Pt addition was expected to affect the stability of nitrates stored by the sorbent and lower the NO_x storage capacity. To study such effects on the sorbent's NSR activity, the transient NO concentration downstream of CuO/Al_2O_3 with 30 wt% Cu and 1 wt% Pt was measured over periodic lean/rich cycles at 300°C. Figure 4.8 shows that the presence of Pt decreased the amount of NO_x stored by the sorbent in the oxidizing atmosphere under two different O_2 concentrations. This was especially evident under 0.5% O_2 pulses, where minimal oxidation of NO to NO_2 occurred during the initial part of the NO_x adsorption cycle due to the lack of O_2 in the gas stream (since the available O_2 was used to re-oxidize the reduced Cu species back to CuO). With the higher O_2 concentration of 7%, complete re-oxidation process followed by steady-state NO conversion took place almost instantaneously, and no NO_x adsorption was observed. This reduction in NO_x storage was in agreement with the NO_x TPD results (Figure 4.9), which showed decreases in both the quantity of NO desorbed and the NO decomposition temperature with the addition of

Pt. Despite these drawbacks, the presence of Pt was nevertheless necessary in promoting the SO_2 resistance of the NO_x trap.

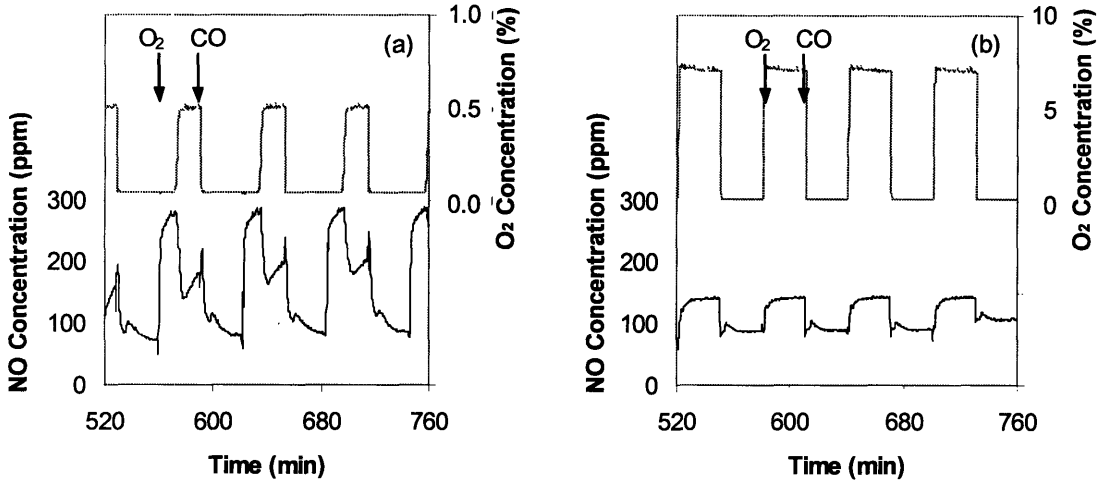

Figure 4.8. NO and O_2 concentrations downstream of the CuO/Al_2O_3 sorbent with 30 wt% Cu and 1 wt% Pt at 300°C. The reactions were run at a space velocity of 16,000 h^{-1} with 300 ppm NO, and alternating pulses of (a) 0.5% and (b) 7% O_2 for 30 min and 1% CO for 30 min.

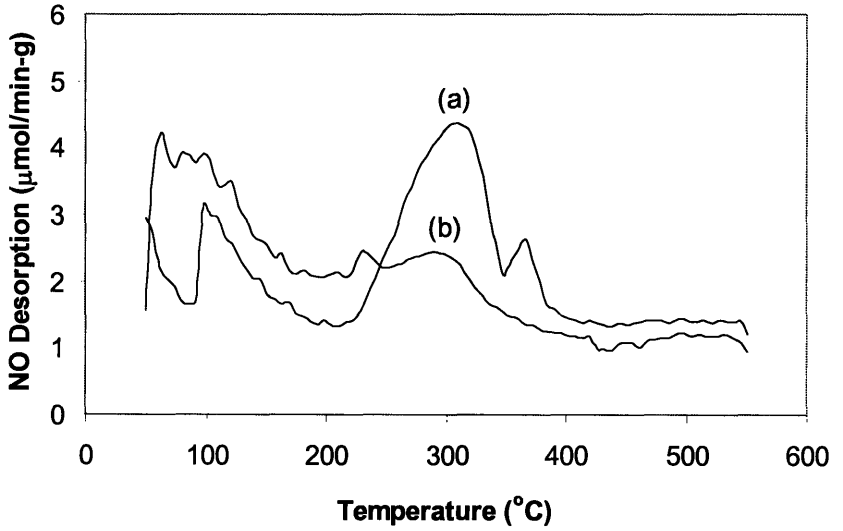

Figure 4.9. TPD profile of NO for the CuO/Al_2O_3 sorbents with 30 wt% Cu and (a) 0 wt% and (b) 1 wt% Pt. See Section 4.2.4 for details on NO TPD.

While the use of Pt produced some undesirable effects on NO_x storage capacity under the oxidizing environment, it improved the NO reduction activity of CuO/Al_2O_3 in the reducing atmosphere. High NO conversion of > 90% was achieved at 300°C with the loading of 1 wt% Pt. The incorporation of Pt was therefore beneficial to both the NO_x desorption and reduction processes.

4.3.2.3. Effect of Rh Addition

Like Pt, the presence of Rh in CuO/Al_2O_3 had also been shown to improve the SO_2 desorption characteristics of the SO_x trap. While the performance of CuO/Al_2O_3 sorbents loaded with only Pt deteriorated during prolonged exposure to SO_2 under reducing atmosphere, those that contained both Rh and Pt were able to maintain good regeneration efficiency and stability. Thus, Rh was also incorporated into the NO_x trap to enhance its NO conversion.

To study the effects of Rh on the sorbent's NSR activity, the transient NO concentration downstream of CuO/Al_2O_3 with 30 wt% Cu and 1 wt% Rh was measured over periodic lean/rich cycles at 300°C under two different O_2 concentrations. Figure 4.10 shows that the Rh addition significantly enhanced the removal of NO by the sorbent under the oxidizing atmosphere. In fact, these sorbents were able to remove almost all of the feed NO within the first 10 min of each adsorption cycle, regardless of the O_2 concentration. The mechanism for the NO removal process was, however, dependent on the O_2 concentration.

At a high O_2 concentration of 7%, Rh was expected to promote rapid NO oxidation and nitrate formation, which would result in the adsorption and storage of NO_x. In this conventional NO_x storage mechanism (typically observed over the noble metal/alkaline earth metal oxide-based catalysts), Pt and Rh have been proposed to increase the oxidation rates of NO to NO_2 and nitrite to nitrate [6-8], with Rh being more active than Pt [20]. This observation was in agreement with our NO_x TPD results. Figure 4.11 shows that even though the Rh addition led to a considerable decrease in the NO decomposition temperature, the $Rh/CuO/Al_2O_3$ sorbent was able to maintain a substantial portion of the original NO_x storage capacity exhibited by CuO/Al_2O_3, in comparison to the $Pt/CuO/Al_2O_3$ sorbent.

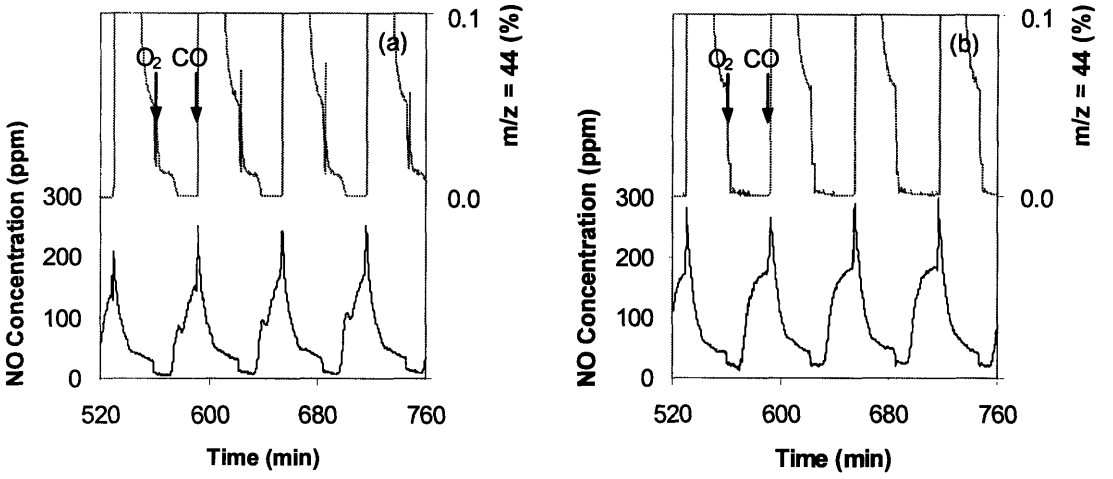

Figure 4.10. Concentrations of NO and m/z = 44 downstream of the CuO/Al_2O_3 sorbent with 30 wt% Cu and 1 wt% Rh at 300°C. The reactions were run at a space velocity of 16,000 h^{-1} with 300 ppm NO, and alternating pulses of (a) 0.5% and (b) 7% O_2 for 30 min and 1% CO for 30 min.

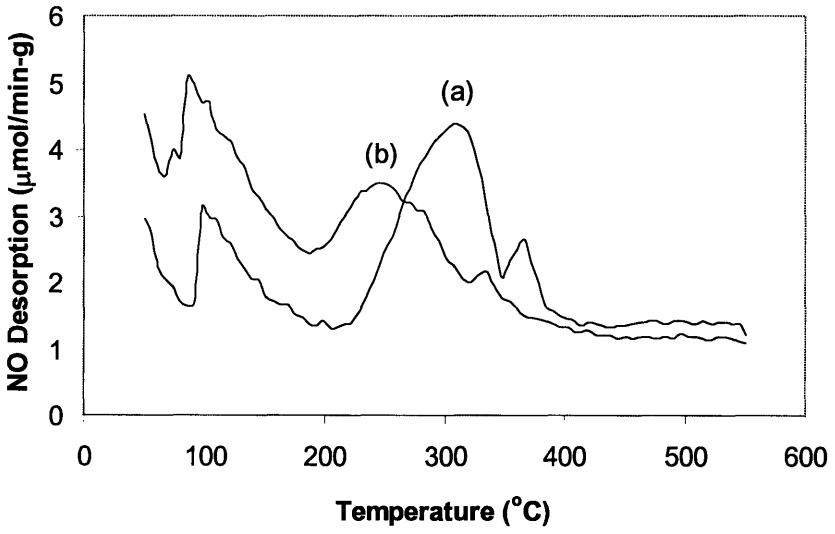

Figure 4.11. TPD profile of NO for the CuO/Al_2O_3 sorbents with 30 wt% Cu and (a) 0 wt% and (b) 1 wt% Rh. See Section 4.2.4 for details on NO TPD.

The NO removal at a lower O_2 concentration of 0.5% by $Rh/CuO/Al_2O_3$ sorbent was accompanied by the production of species with m/z = 44, which could be either CO_2 or N_2O. Since its quantity declined with the rise in NO and O_2 concentrations, this species appeared to be N_2O. During the initial part of each adsorption cycle when O_2 was

absent, the N_2O molecules were likely produced as a by-product from the direct decomposition of NO into N_2 and O_2 over the reduced Rh species. As the Rh-based catalysts were re-oxidized and the O_2 concentration was increased, the dissociation of NO was discontinued. This behavior had also been reported in the studies on NO_x reduction over Rh/β-zeolite under periodic lean/rich operations [21,22]. The direct NO dissociation was, however, unlikely to be an important path for NO_x removal over our Rh-based sorbents under the more realistic O_2 concentration of 7%.

Although Rh addition did not seem to enhance the NSR activity of the sorbent in the reducing environment, NO desorption and subsequent catalytic reduction with CO still took place fairly efficiently. Reasonably high NO conversion of ~ 80% was eventually attained at 300°C towards the end of each reduction cycle. The presence of Rh, therefore, brought about improvements in the overall performance of the NO_x trap by significantly increasing the amount of NO_x stored by the sorbent during the adsorption cycle.

4.3.3. NO_x Storage-Reduction over Pt-Rh/CuO/Al_2O_3

To take advantage of the good NO_x storage properties of Rh/CuO/Al_2O_3 and the high SO_2 regeneration efficiency of Pt/CuO/Al_2O_3, various CuO/Al_2O_3 sorbents loaded with both Pt and Rh were synthesized. To study the effect of Pt addition on the NSR activity, the transient NO concentration downstream of Rh/CuO/Al_2O_3 sorbents with different Pt loadings was measured over periodic lean/rich cycles at 200–400°C. Figure 4.12 shows that while the combined NO conversion below 300°C decreased with the incorporation of Pt, the opposite effect was observed at higher temperatures.

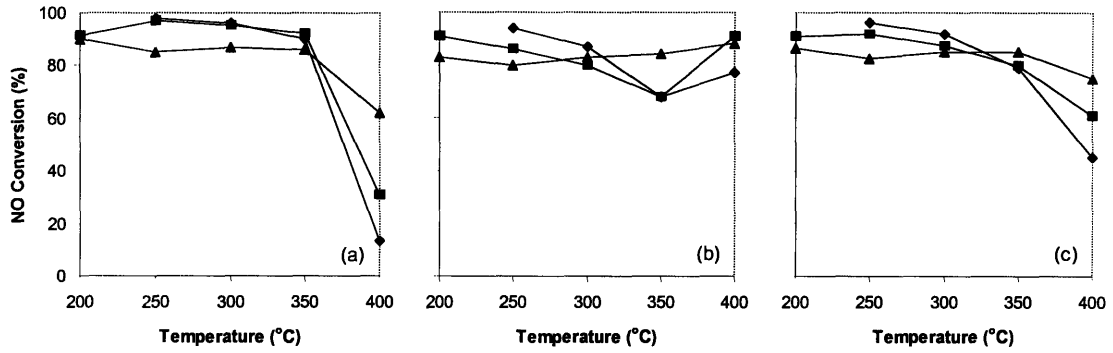

Figure 4.12. Average NO conversion over the CuO/Al_2O_3 sorbents with 30 wt% Cu, 1 wt% Rh, and (♦) 0 wt%, (■) 0.1 wt% and (▲) 1 wt% Pt during the (a) adsorption, (b) desorption and (c) combined adsorption-desorption cycle. The reactions were run at a space velocity of 16,000 h^{-1} with 300 ppm NO, and alternating pulses of 7% O_2 for 5 min and 1% CO for 5 min.

At low temperatures, the NO_x storage behavior under the oxidizing atmosphere was dominated by the presence of Rh, and the addition of Pt simply lowered the amount of NO_x stored. Pt loading also decreased the sorbent activity under the reducing atmosphere as Rh was more active than Pt in catalytic reduction of NO [23]. The addition of Pt, therefore, led to a reduction in the sorbent's NSR activity. At a higher temperature of 400°C, however, Rh was no longer an effective promoter of NO_x storage due to nitrate instability. The improvement in the NO conversion observed with increasing Pt loading was merely due to the oxidation of NO to NO_2 over Pt; it was not beneficial to the NSR performance of the sorbent.

Overall, the noble metal-loaded CuO/Al_2O_3 sorbents were very effective at NO_x storage-reduction with excellent NO conversion of 90% at 300°C. The NO conversion, however, would decrease to 60% in the presence of 60 ppm SO_2, despite all the improvements made in the SO_2 regeneration efficiency with the addition of Pt and Rh. To further improve the performance of these NO_x traps, the sorbents' NO_x storage capacity might be increased with the use of alkaline-earth metal oxides, such as MgO. Such enhancement in the SO_2-free storage capacity, however, might come at the expense of the sorbent's SO_2 resistance due to the stability of $MgSO_4$. The optimal NSR activity in the presence of SO_2 therefore depended on balancing between the NO_x storage capacity and the SO_2 regeneration efficiency of the sorbent.

4.3.4. Noble Metal-loaded CuO-MgO/Al_2O_3

4.3.4.1. NO and SO_2 TPD Studies

To study the effects of MgO addition on NO_x storage capacity and nitrate stability, TPD experiments were performed on CuO-MgO/Al_2O_3 sorbents with various Cu and Mg loadings. Figure 4.13 shows that the NO desorption temperature increased from 310°C for CuO/Al_2O_3 with 30 wt% Cu to 340°C for CuO-MgO/Al_2O_3 with 6 wt% Cu and 24 wt% Mg. However, the addition of Pt and Rh to the CuO-MgO/Al_2O_3 sorbents led to reductions in both the NO desorption temperature and the quantity of NO desorbed (see Figure 4.14). Despite this loss of NO_x capacity, NO_x adsorption at temperatures of interest was still possible over the sorbents with high Mg loadings.

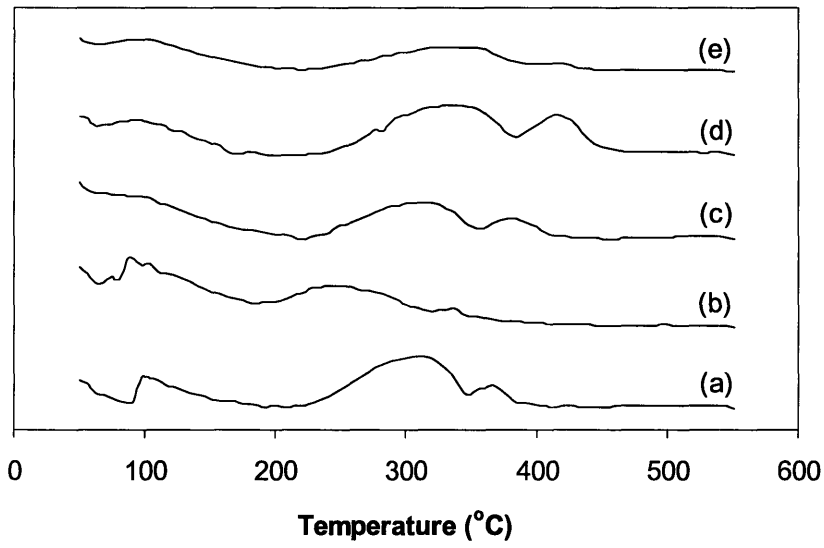

Figure 4.13. TPD profile of NO for CuO-MgO/Al_2O_3 sorbents with a total Cu + Mg loading of 30 wt% consisting of (a) 0 wt%, (b) 6 wt%, (c) 12 wt%, (d) 18 wt% and (e) 24 wt% Mg. See Section 4.2.4 for details on NO TPD.

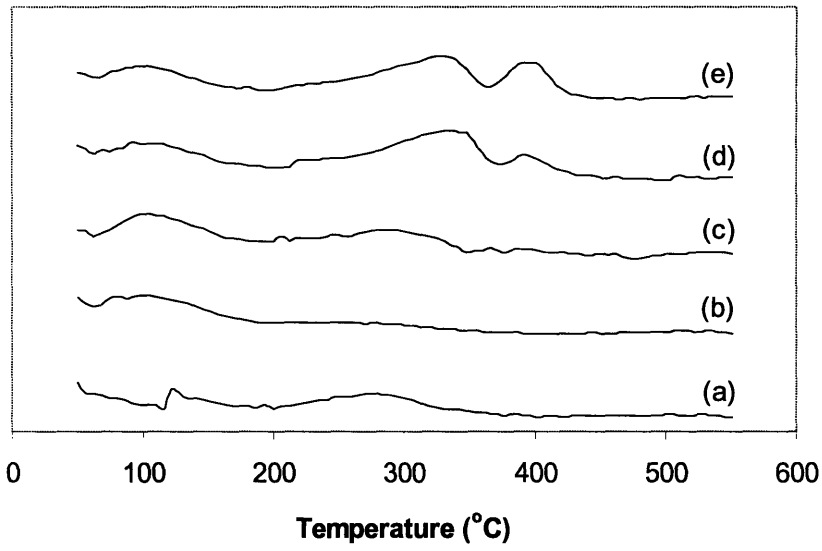

Figure 4.14. TPD profile of NO for CuO-MgO/Al_2O_3 sorbents with 1 wt% Pt, 1 wt% Rh, and a total Cu + Mg loading of 30 wt% consisting of (a) 0 wt%, (b) 6 wt%, (c) 12 wt%, (d) 18 wt% and (e) 24 wt% Mg. See Section 4.2.4 for details on NO TPD.

Although high Mg loading was desirable for good NO_x storage properties, excessive usage of Mg was expected to result in strong SO_2 adsorption, which could lead to permanent deactivation of the NO_x storage material. To explore this potential issue, SO_2 TPD experiments were performed on the CuO-MgO/Al_2O_3 sorbents. Figure 4.15 shows that the SO_2 desorption temperature increased from 420°C for CuO/Al_2O_3 with 30 wt% Cu to 530°C for CuO-MgO/Al_2O_3 with 6 wt% Cu and 24 wt% Mg. This increase in sulfate stability with Mg loading also reduced the quantity of SO_2 desorbed. The high SO_2 desorption temperatures could be lowered with the use of Pt and Rh, provided that the Mg loading was low (see Figure 4.16). For example, the sulfate decomposed from the Pt-Rh/CuO-MgO/Al_2O_3 sorbent with 18 wt% Cu and 12 wt% Mg at 390°C, which was ~ 90°C higher than the nitrate decomposition temperature. This relatively small difference in the sulfate and nitrate desorption temperatures might allow sorbents with moderate Cu and Mg loadings to function as SO_x-tolerant NO_x trap. In this type of materials, the NO_x storage capacity could be raised at the expense of the SO_2 resistance by using either more Mg or less Pt. This allowed the sorbent characteristics to be adjusted, and the optimal sorbent composition would depend on the operating conditions,

such as temperature, space velocity, CO concentration, and the amounts of NO and SO_2 in the feed stream.

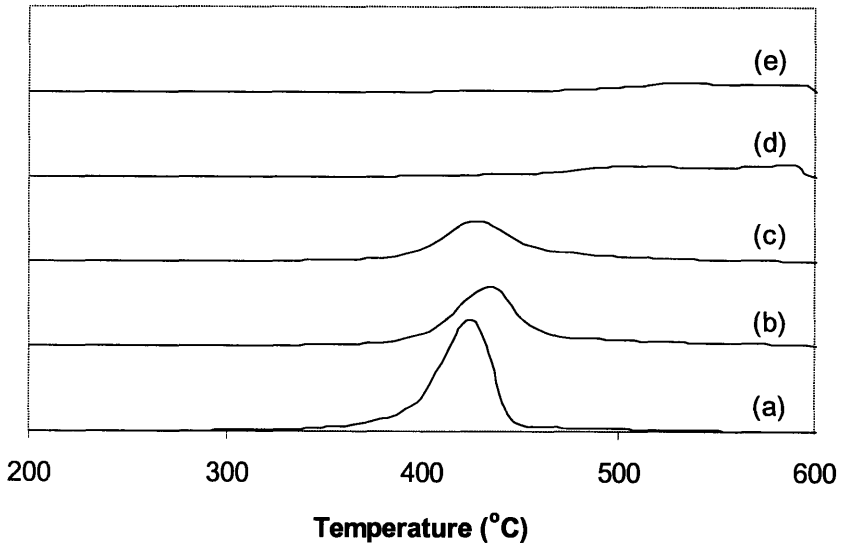

Figure 4.15. TPD profile of SO_2 for CuO-MgO/Al_2O_3 sorbents with a total Cu + Mg loading of 30 wt% consisting of (a) 0 wt%, (b) 6 wt%, (c) 12 wt%, (d) 18 wt% and (e) 24 wt% Mg. See Sections 4.2.5 on SO_2 TPD.

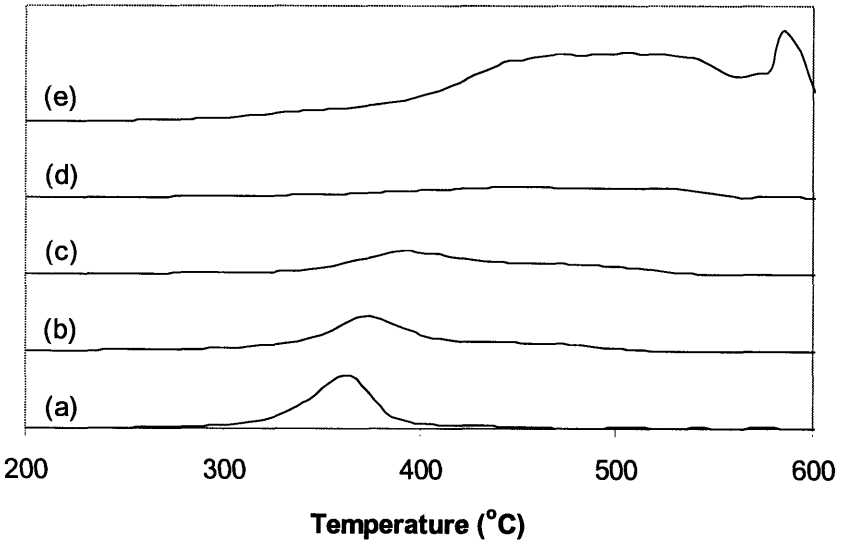

Figure 4.16. TPD profile of SO_2 for CuO-MgO/Al_2O_3 sorbents with 1 wt% Pt, 1 wt% Rh, and a total Cu + Mg loading of 30 wt% consisting of (a) 0 wt%, (b) 6 wt%, (c) 12 wt%, (d) 18 wt% and (e) 24 wt% Mg. See Sections 4.2.5 on SO_2 TPD.

4.3.4.2. NO_x Storage-Reduction

To understand the effect of Mg incorporation on the NSR activity, the transient NO concentration downstream of sorbents with various Cu and Mg loadings was measured over periodic lean/rich cycles at 300°C. Figures 4.17 and 4.18 show that the presence of Mg significantly improved the NO_x storage capacity of $Rh/CuO/Al_2O_3$ and $Pt/CuO/Al_2O_3$, respectively, under the oxidizing atmosphere. Much more NO_x was removed by the sorbents with 6 wt% Mg compared with those that contained no Mg, even though only half the amount of sorbents was used in the former. Further addition of Mg generally led to even higher NO_x removal efficiencies. This was especially true for the Rh-loaded sorbent where the addition of 12 wt% Mg allowed almost all of the NO_x to be stored over the first 15 min of each adsorption cycle. Higher Mg loadings of 18 wt% and 24 wt% led to undesirable N_2O formation, possibly through the direct decomposition of NO. Thus, excessive Mg loading was not beneficial to the NO_x storage capacity of the $Rh/CuO\text{-}MgO/Al_2O_3$ sorbents.

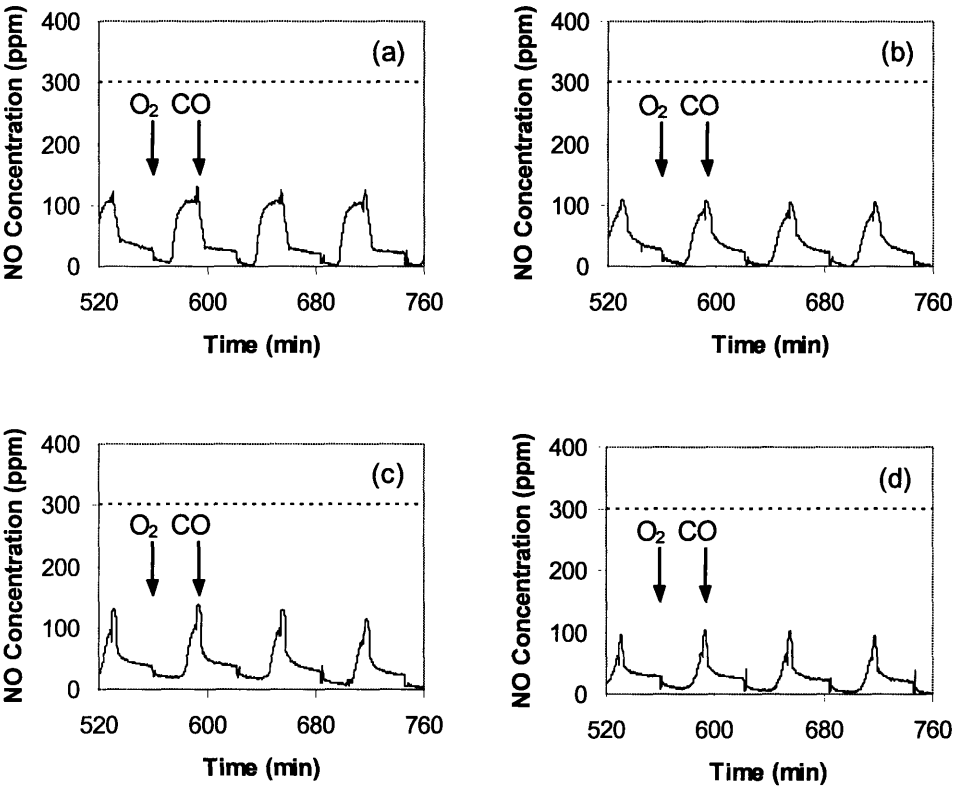

Figure 4.17. NO adsorption/desorption profile of CuO-MgO/Al_2O_3 sorbents with 1 wt% Rh, and a total Cu + Mg loading of 30 wt% consisting of (a) 6 wt%, (b) 12 wt%, (c) 18 wt% and (d) 24 wt% Mg at 300°C. The reactions were run at a space velocity of 32,000 h^{-1} with 300 ppm NO, and alternating pulses of 7% O_2 for 30 min and 1% CO for 30 min.

Significantly less NO was removed during the oxidizing cycle when Pt was used in place of Rh. The amount of NO_x stored by the Pt/CuO-MgO/Al_2O_3 sorbent with 12 wt% Mg was only comparable to that stored by the Rh/CuO-MgO/Al_2O_3 with 6 wt% Mg. As more Mg was incorporated into the Pt/CuO-MgO/Al_2O_3 sorbents, more NO was oxidized to NO_2 during the oxidizing cycle. This was not observed in the Rh/CuO-MgO/Al_2O_3 sorbents, as adsorbed NO seemed to be more stable in the presence of Rh. Despite the increase in NO oxidation, Pt/CuO-MgO/Al_2O_3 sorbents were able to store more NO_x as their Mg loadings were increased (as seen by the increase in the amount of NO desorbed during regeneration in Figure 4.18). This trend was not observed over the Rh/CuO-MgO/Al_2O_3 sorbents, which showed highly efficient NO reduction under the reducing atmosphere.

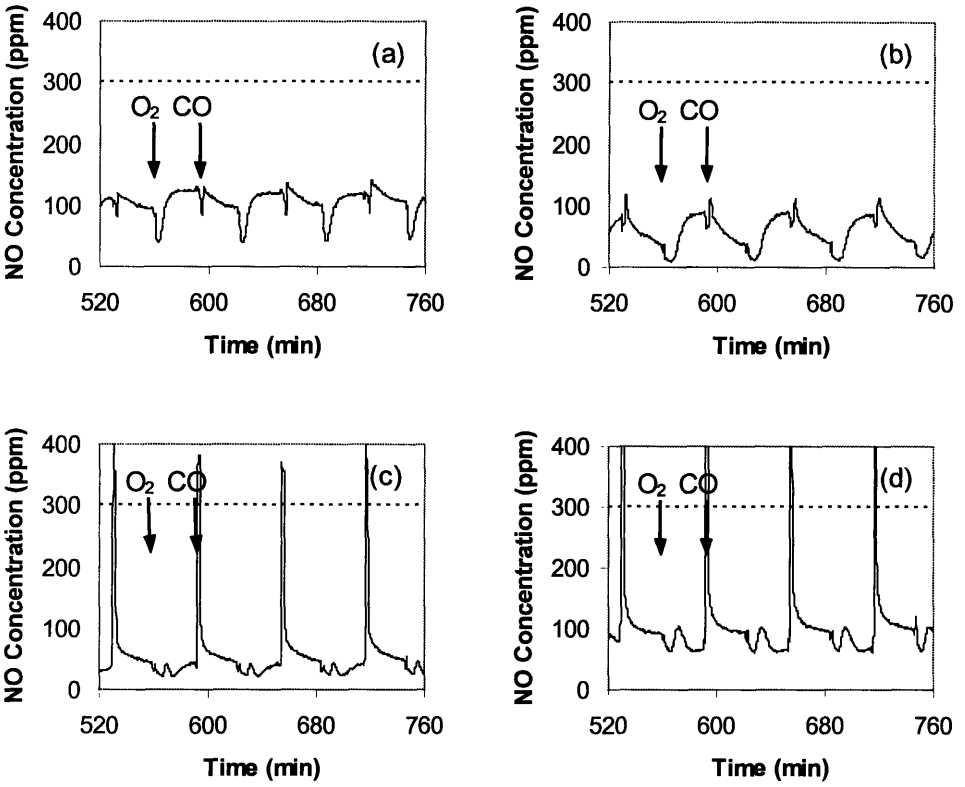

Figure 4.18. NO adsorption/desorption profile of CuO-MgO/Al_2O_3 sorbents with 1 wt% Pt, and a total Cu + Mg loading of 30 wt% consisting of (a) 6 wt%, (b) 12 wt%, (c) 18 wt% and (d) 24 wt% Mg at 300°C. The reactions were run at a space velocity of 32,000 h^{-1} with 300 ppm NO, and alternating pulses of 7% O_2 for 30 min and 1% CO for 30 min.

The NO adsorption/desorption profiles of Pt-Rh/CuO-MgO/Al_2O_3 sorbents are illustrated in Figure 4.19 with their NO breakthrough capacities summarized in Figure 4.20. These results show that all the Pt-Rh/CuO-MgO/Al_2O_3 sorbents with > 6 wt% Mg had sufficient NO breakthrough capacity (≥ 1.8 mg NO/g) for the NSR operation under periodic 5-min lean/rich cycles. As seen in Figure 4.21, almost all the NO_x in the feed stream was removed during the 5-min oxidizing cycle for all the temperatures examined. Good NO conversions of over 80% were maintained over the sorbents even at 400°C, regardless of their Mg loadings.

Although improvement in the lean NO_x activity was observed with Mg addition, Mg incorporation also lowered the NO reduction activity of the sorbent (as seen by the increase in the amount of unreduced NO desorbed during regeneration in Figure 4.22). The Mg content of the sorbents was therefore limited to that necessary to achieve

sufficient NO_x storage. The low Mg loading required was also valuable towards maintaining the sorbents' resistance against SO_2 poisoning.

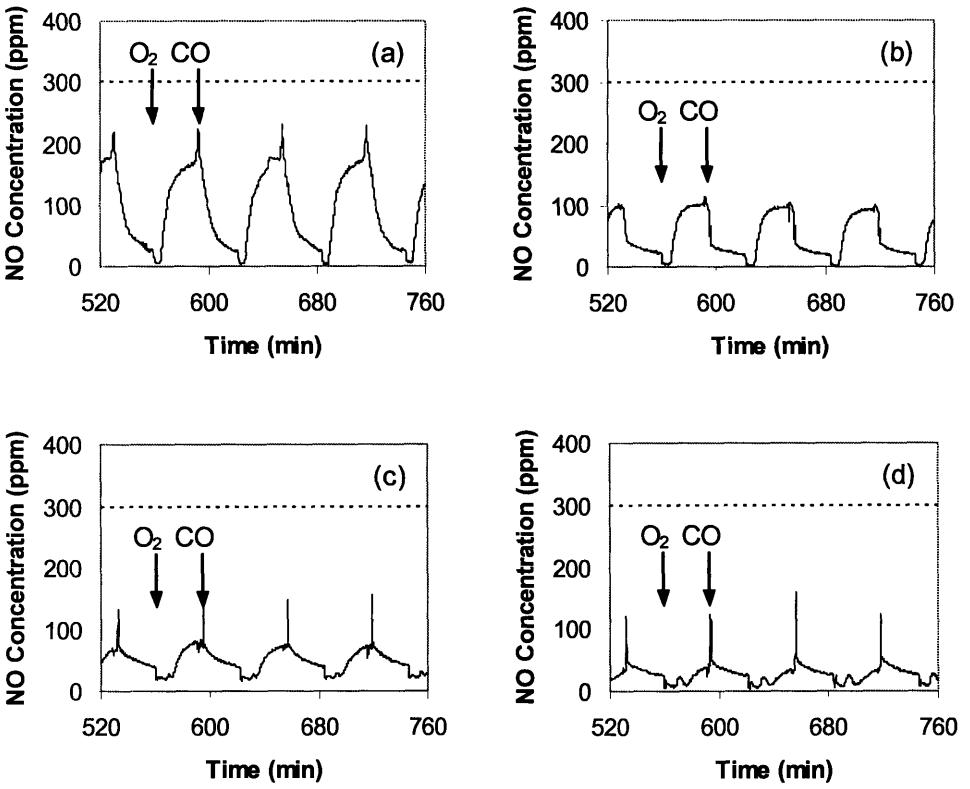

Figure 4.19. NO adsorption/desorption profile of $CuO\text{-}MgO/Al_2O_3$ sorbents with 1 wt% Pt, 1 wt% Rh, and a total Cu + Mg loading of 30 wt% consisting of (a) 6 wt%, (b) 12 wt%, (c) 18 wt% and (d) 24 wt% Mg at 300°C. The reactions were run at a space velocity of 32,000 h^{-1} with 300 ppm NO, and alternating pulses of 7% O_2 for 30 min and 1% CO for 30 min.

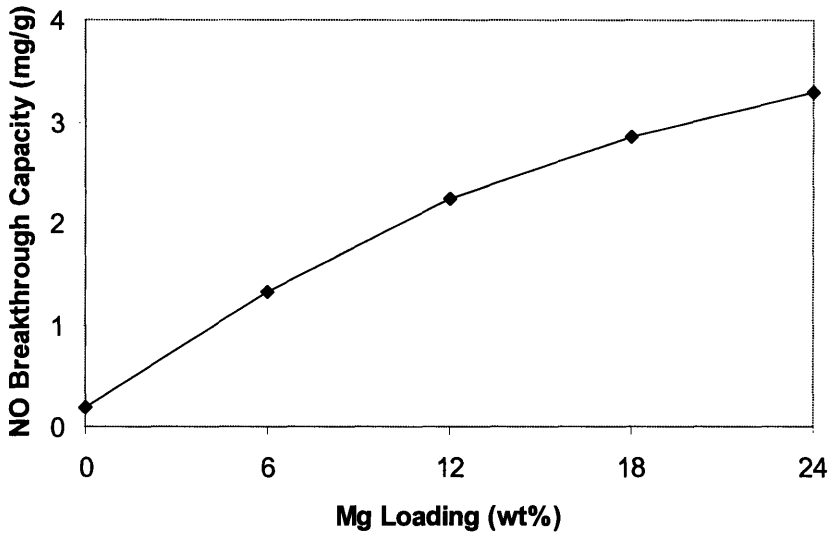

Figure 4.20. Effect of Mg loading on the NO breakthrough capacity of CuO-MgO/Al_2O_3 sorbents with 1 wt% Pt, 1 wt% Rh, and a total Cu + Mg loading of 30 wt% at 300°C. The reactions were run at a space velocity of 32,000 h^{-1} with 300 ppm NO, and alternating pulses of 7% O_2 for 30 min and 1% CO for 30 min.

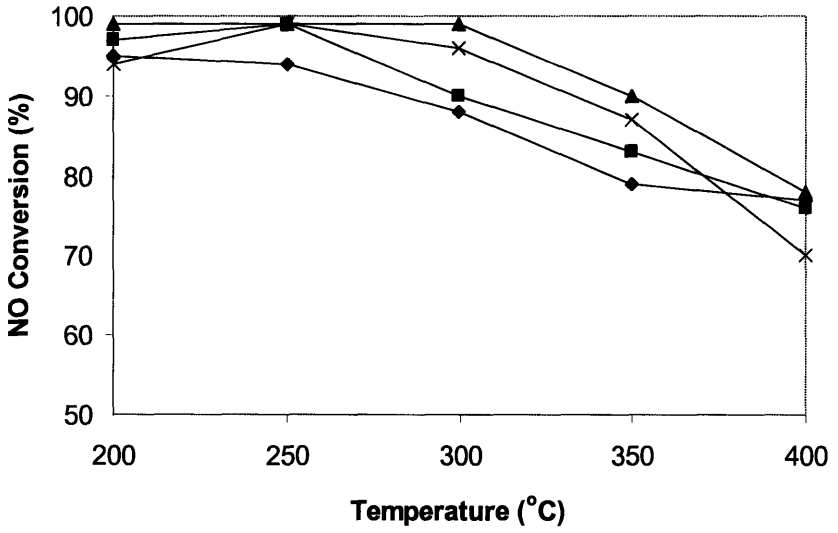

Figure 4.21. NO conversion over CuO-MgO/Al_2O_3 sorbents with 1 wt% Pt, 1 wt% Rh, and a total Cu + Mg loading of 30 wt% consisting of (♦) 6 wt%, (■) 12 wt%, (▲) 18 wt% and (×) 24 wt% Mg during the lean adsorption cycles. The reactions were run at a space velocity of 32,000 h^{-1} with 300 ppm NO, and alternating pulses of 7% O_2 for 5 min and 1% CO for 5 min.

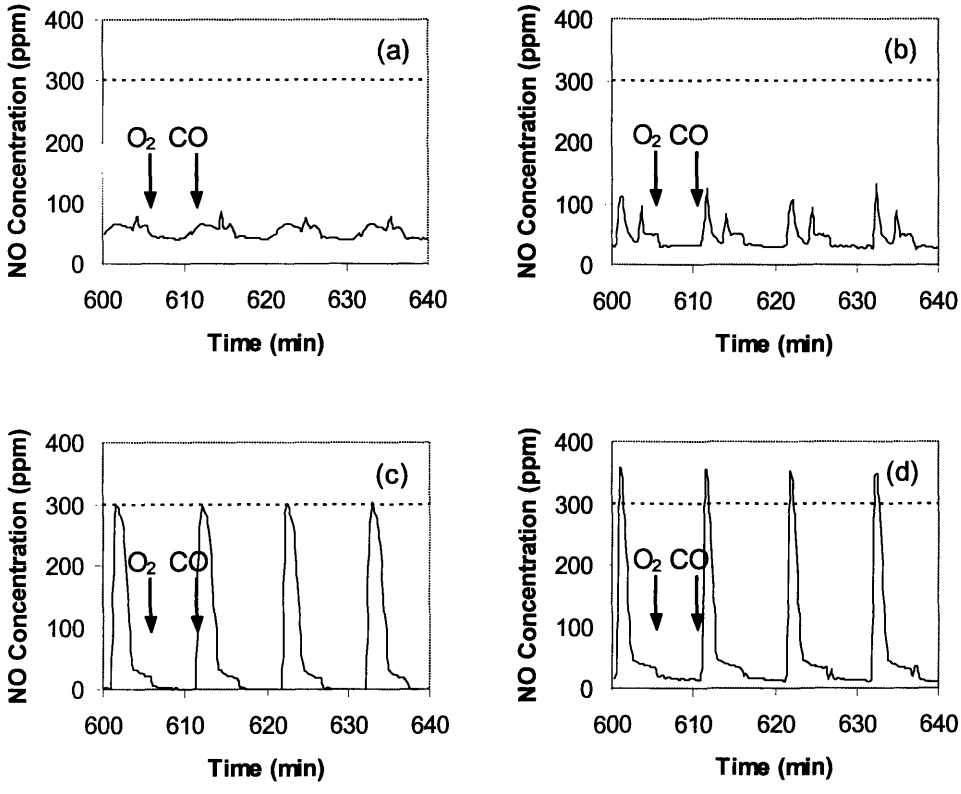

Figure 4.22. NO adsorption/desorption profile of CuO-MgO/Al_2O_3 sorbents with 1 wt% Pt, 1 wt% Rh, and a total Cu + Mg loading of 30 wt% consisting of (a) 6 wt%, (b) 12 wt%, (c) 18 wt% and (d) 24 wt% Mg at 300°C. The reactions were run at a space velocity of 32,000 h^{-1} with 300 ppm NO, and alternating pulses of 7% O_2 for 5 min and 1% CO for 5 min.

4.3.4.3. Effect of SO_2

The SO_2 resistance of the Pt-Rh/CuO-MgO/Al_2O_3 sorbents could be improved at the expense of their NO_x storage capacities by using a small amount of Mg. Higher Mg loadings could be beneficial towards maintaining the NSR activities of these sorbents in the presence of SO_2 since more adsorption sites would be available for NO_x and SO_x storage. The transient NO concentration downstream of the Pt-Rh/CuO-MgO/Al_2O_3 sorbents with various Mg loadings was measured over periodic lean/rich cycles at 300°C in the presence of SO_2. Figure 4.23 shows that while the performance of the sorbents with high Mg loadings deteriorated at faster rates, the NO conversion over these sorbents was significantly higher. For example, the sorbent with 24 wt% Mg had an initial NO conversion of 98%, which declined to 63% after 400 min of operation. In contrast, the

sorbent with 6 wt% Mg showed an initial NO conversion of 81%, which decreased to 56% during the operation. This illustrated that there were potential benefits in using sorbents with high Mg contents, especially in NSR applications that involved regeneration at high temperatures (> 300°C).

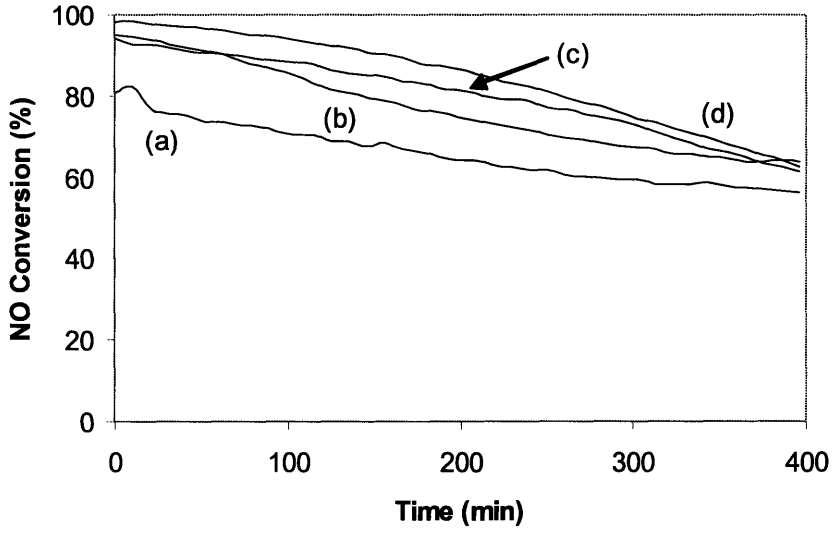

Figure 4.23. Lean NO conversion of $CuO\text{-}MgO/Al_2O_3$ sorbents with 1 wt% Pt, 1 wt% Rh, and a total Cu + Mg loading of 30 wt% consisting of (a) 6 wt%, (b) 12 wt%, (c) 18 wt% and (d) 24 wt% Mg at 300°C. The reactions were run at a space velocity of 32,000 h^{-1} with 300 ppm NO, 60 ppm SO_2, and alternating pulses of 7% O_2 for 5 min and 1% CO for 5 min.

Regardless of the chosen mode of NSR operation, it was important to recognize that a significant portion of the NO conversion observed over the sorbent was a direct result of steady-state NO oxidation to NO_2, which would not lead to NO_x removal from the gas stream. This unproductive reaction appeared to be the dominant NO conversion route during the later part of a cycle where less adsorption sites were available for NO_x storage (see Figures 4.17–4.19). Since SO_2 competed with NO_x for adsorption sites, the accumulation of adsorbed SO_2 on the sorbent would reduce the number of sites available for NO_x storage, leading eventually to steady-state NO oxidation. This form of NO conversion was observed over all sorbents after prolonged SO_2 exposure (see Figures 4.24 and 4.25). While the sorbent with 24 wt% Mg was able to maintain some NO_x storage capacity for 350 min under periodic lean/rich operation, the sorbent with 6 wt% Mg lost most of its NO_x storage capacity after 150 min. This illustrated the benefit of

employing a high Mg loading. The NO_x storage durations of the fresh sorbents are summarized in Table 4.1.

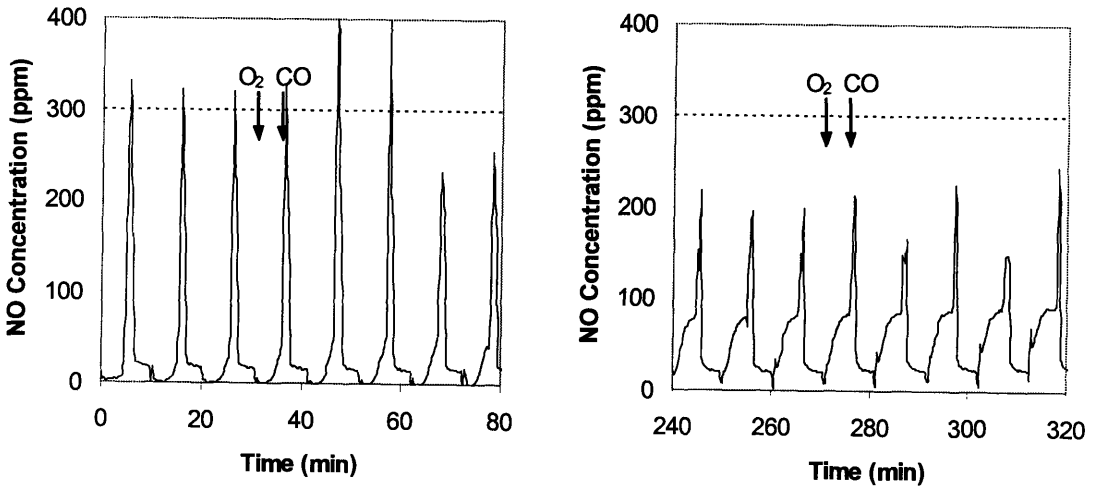

Figure 4.24. NO adsorption/desorption profile of CuO-MgO/Al_2O_3 sorbents with 1 wt% Pt, 1 wt% Rh, 6 wt% Cu and 24 wt% Mg at 300°C. The reactions were run at a space velocity of 32,000 h^{-1} with 300 ppm NO, 60 ppm SO_2, and alternating pulses of 7% O_2 for 5 min and 1% CO for 5 min.

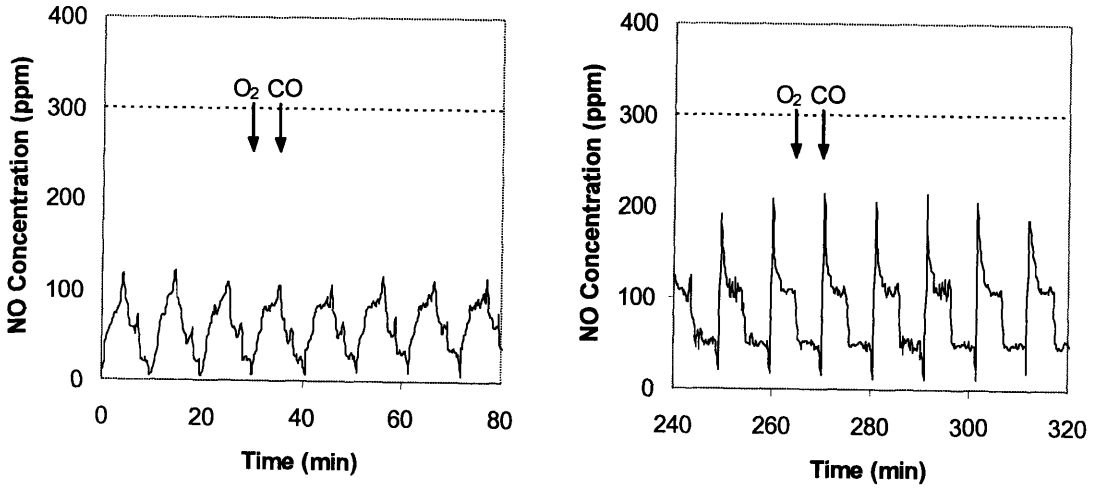

Figure 4.25. NO adsorption/desorption profile of CuO-MgO/Al_2O_3 sorbents with 1 wt% Pt, 1 wt% Rh, 24 wt% Cu and 6 wt% Mg at 300°C. The reactions were run at a space velocity of 32,000 h^{-1} with 300 ppm NO, 60 ppm SO_2, and alternating pulses of 7% O_2 for 5 min and 1% CO for 5 min.

Table 4.1. Lean NO conversion over the fresh and regenerated CuO-MgO/Al_2O_3 sorbents with 1 wt% Pt, 1 wt% Rh, and a total Cu + Mg loading of 30 wt%.

Cu Loading (wt%)	Mg Loading (wt%)	Fresh Sorbent's Activity[a] (%)	Duration (min)	Regenerated Sorbent's Activity[b] (%)
24	6	81	150	80
18	12	95	270	82
12	18	94	350	84
6	24	98	350	82

[a] The fresh sorbent's activity was measured at a space velocity of 32,000 h^{-1} at 300°C with 300 ppm NO, 60 ppm SO_2, and alternating pulses of 7% O_2 for 5 min and 1% CO for 5 min.
[b] The regenerated sorbent's activity was measured at a space velocity of 32,000 h^{-1} at 300°C with 300 ppm NO, and alternating pulses of 7% O_2 for 5 min and 1% CO for 5 min, after regeneration at 500°C with 1.5% CO.

Although the performance of fresh sorbents with high Mg loadings was superior to those with lower Mg contents, the latter could be regenerated efficiently under moderate temperatures. For the Pt-Rh/CuO-MgO/Al_2O_3 sorbents that had been exposed to SO_2 for 24 hours and subsequently regenerated at 500°C, NO concentration downstream was measured over periodic lean/rich cycles at 300°C. Figure 4.26 shows that even though the NO conversion after regeneration at 500°C was high over all Pt-Rh/CuO-MgO/Al_2O_3 sorbents, only partial regeneration was achieved since a significant portion of NO was still being converted to NO_2 via catalytic oxidation. In fact, the sorbent with 24 wt% Mg displayed almost no NO_x storage capacity after regeneration, indicating that this sorbent could not be regenerated at 500°C. The best NSR activities (~ 80% NO conversions) were displayed by the sorbents with 12 wt% and 18 wt% Mg. These two materials outperformed the sorbent with 6 wt% Mg (which showed the lowest SO_2 desorption temperature), possibly because of their greater intrinsic NO_x adsorption capacities associated with higher Mg loadings.

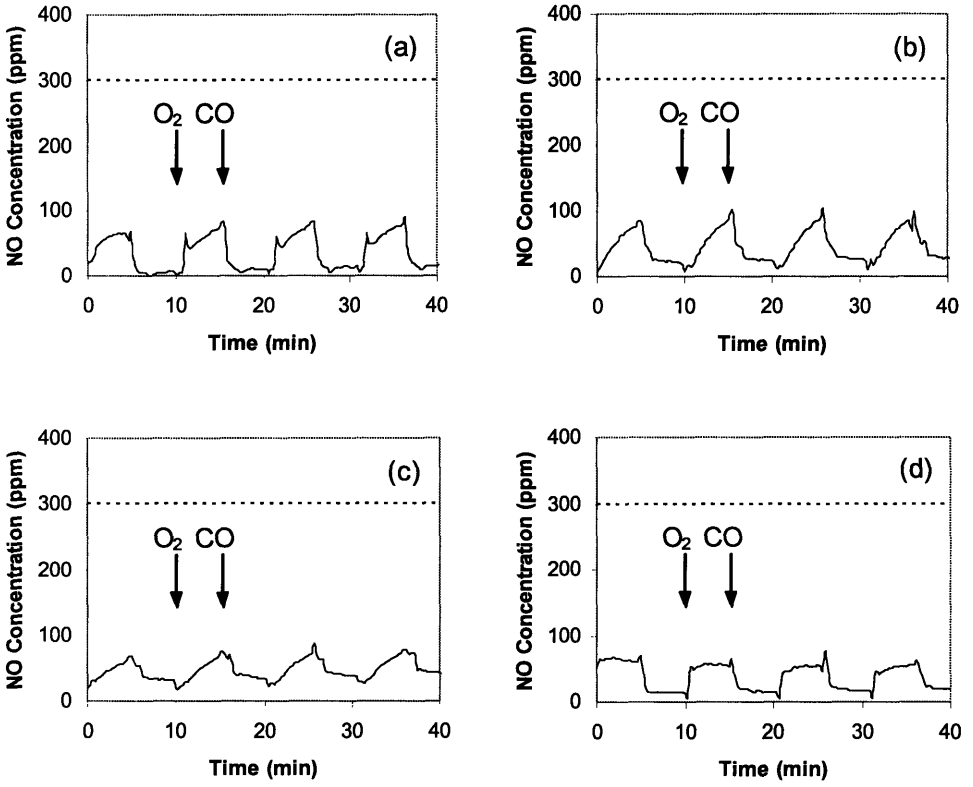

Figure 4.26. NO adsorption/desorption profile of CuO-MgO/Al_2O_3 sorbents with 1 wt% Pt, 1 wt% Rh, and a total Cu + Mg loading of 30 wt% consisting of (a) 6 wt%, (b) 12 wt%, (c) 18 wt% and (d) 24 wt% Mg at 300°C. The reactions were run at a space velocity of 32,000 h^{-1} with 300 ppm NO, and alternating pulses of 7% O_2 for 5 min and 1% CO for 5 min, after regeneration at 500°C with 1.5% CO.

To achieve desirable NSR performance, it would be important to attain a balance between the NO_x adsorption capacity and the regeneration efficiency at elevated temperatures. This could be controlled not only by the loadings of Cu and Mg, but also by the noble metal composition in the sorbents. Since the presence of Pt failed to eliminate the need for Pt-Rh/CuO-MgO/Al_2O_3 sorbents to regenerate at 500°C and yet lowered the NO_x storage capacities, Rh/CuO-MgO/Al_2O_3 sorbents were examined instead. Indeed, the latter were shown to have superior NO_x storage capacities and comparable SO_2 regeneration efficiencies to Pt-Rh/CuO-MgO/Al_2O_3 with similar Cu and Mg loadings (see Figures 4.27 and 4.28, respectively).

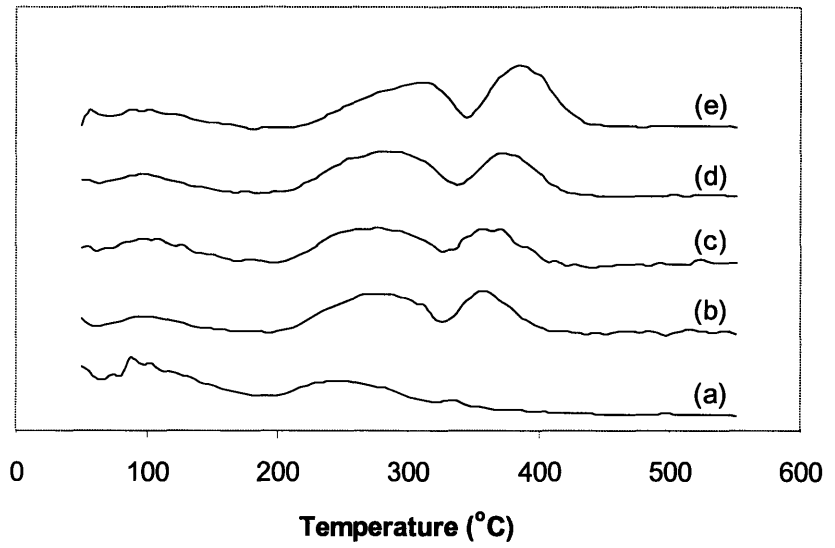

Figure 4.27. TPD profile of NO for CuO-MgO/Al_2O_3 sorbents with 1 wt% Rh, and a total Cu + Mg loading of 30 wt% consisting of (a) 0 wt%, (b) 6 wt%, (c) 12 wt%, (d) 18 wt% and (e) 24 wt% Mg. See Section 4.2.4 for details on NO TPD.

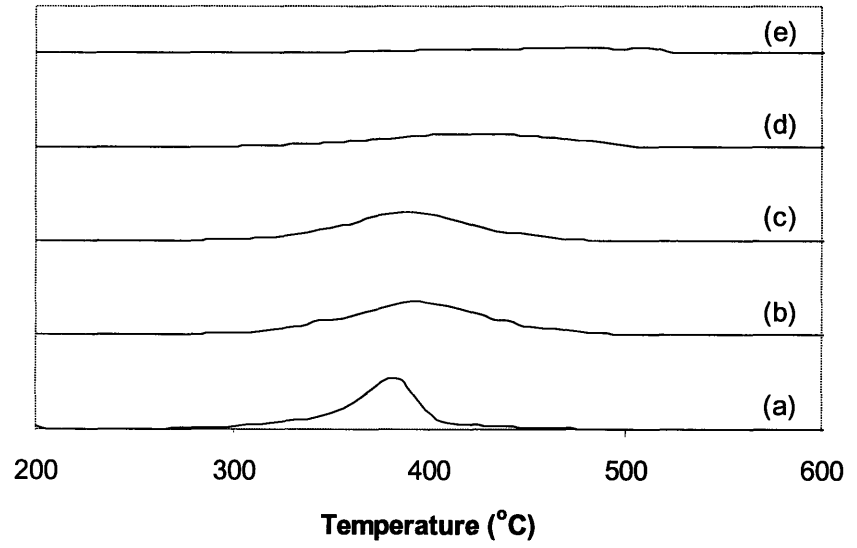

Figure 4.28. TPD profile of SO_2 for CuO-MgO/Al_2O_3 sorbents with 1 wt% Rh, and a total Cu + Mg loading of 30 wt% consisting of (a) 0 wt%, (b) 6 wt%, (c) 12 wt%, (d) 18 wt% and (e) 24 wt% Mg. See Section 4.2.5 for details on SO_2 TPD.

4.3.5. Rh/CuO-MgO/Al_2O_3

To investigate their use as SO_x-tolerant NSR catalysts, the transient NO concentration downstream of the Rh/CuO-MgO/Al_2O_3 sorbents was measured over

periodic lean/rich cycles at 300°C in the presence of SO_2. The changes in the lean NO conversion over these sorbents are shown in Figure 4.29, and the actual NO concentration profiles of the sorbents with 24 wt% and 6 wt% Mg are illustrated in Figures 4.30 and 4.31, respectively. The NO conversions achieved over the Rh/CuO-MgO/Al_2O_3 sorbents were significantly higher than those over the Pt-containing sorbents. Without Pt, the sorbents with 24 wt% and 6 wt% Mg were able to maintain some NO_x storage capacities for as long as 440 min and 280 min, respectively (see Table 4.2). The improvements in both NO conversion and durability of NO_x storage performance could be attributed to the increase in NO_x storage capacity in the absence of Pt, as seen by comparing the NO breakthrough capacities of the sorbents in Figure 4.17 with those in Figure 4.19.

This increase in NO_x adsorption, however, did not appear to hinder the regeneration of the aged sorbents at 500°C (see Table 4.2). In fact, the best NSR activities (> 85%) exhibited by the regenerated Rh/CuO-MgO/Al_2O_3 sorbents with 6 wt% and 12 wt% Mg (Table 4.2) were even slightly higher than those observed over the regenerated Pt-Rh/CuO-MgO/Al_2O_3 sorbents (Table 4.1).

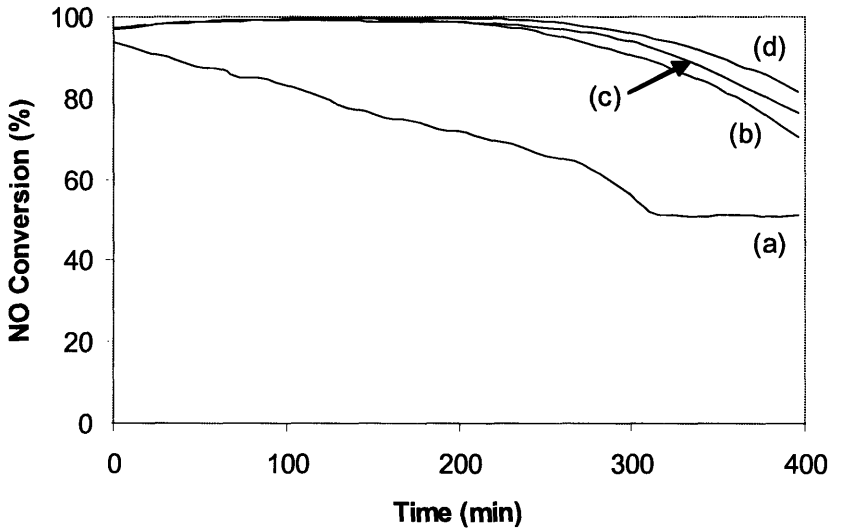

Figure 4.29. Lean NO conversion of CuO-MgO/Al_2O_3 sorbents with 1 wt% Rh, and a total Cu + Mg loading of 30 wt% consisting of (a) 6 wt%, (b) 12 wt%, (c) 18 wt% and (d) 24 wt% Mg at 300°C. The reactions were run at a space velocity of 32,000 h^{-1} with 300 ppm NO, 60 ppm SO_2, and alternating pulses of 7% O_2 for 5 min and 1% CO for 5 min.

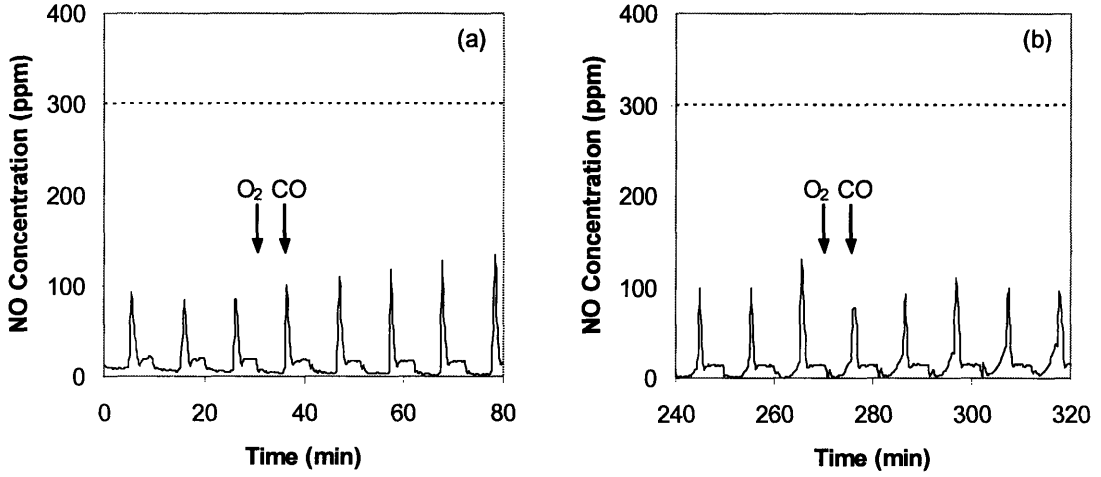

Figure 4.30. Effect of SO_2 exposure on the NO adsorption/desorption profile of CuO-MgO/Al_2O_3 with 1 wt% Rh, 6 wt% Cu and 24 wt% Mg at 300°C. The reactions were run at a space velocity of 32,000 h^{-1} with 300 ppm NO, 60 ppm SO_2, and alternating pulses of 7% O_2 for 5 min and 1% CO for 5 min.

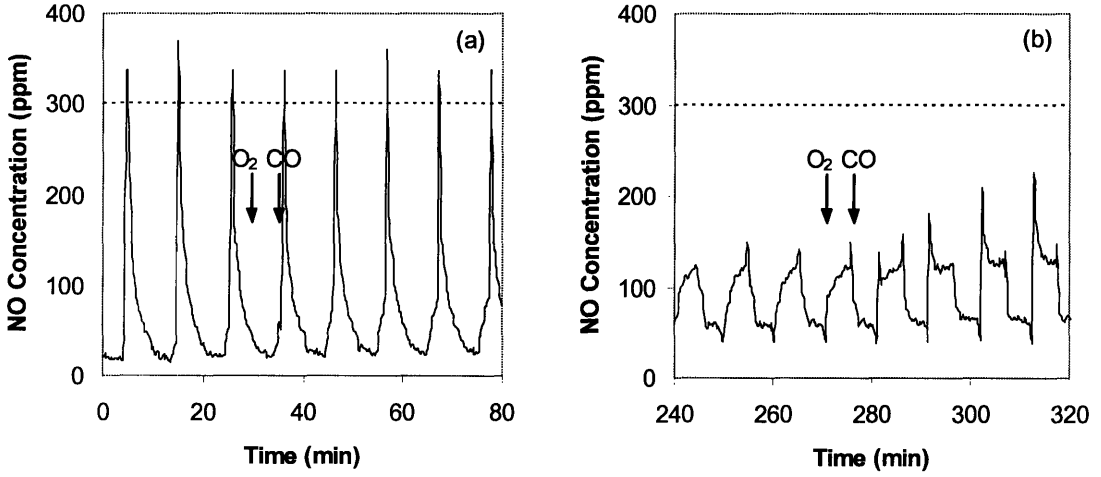

Figure 4.31. Effect of SO_2 exposure on the NO adsorption/desorption profile of CuO-MgO/Al_2O_3 with 1 wt% Rh, 24 wt% Cu and 6 wt% Mg at 300°C. The reactions were run at a space velocity of 32,000 h^{-1} with 300 ppm NO, 60 ppm SO_2, and alternating pulses of 7% O_2 for 5 min and 1% CO for 5 min.

The regenerated sorbents were re-exposed to SO_2 in another NSR operation. Figures 4.32 and 4.33 illustrate that all Rh/CuO-MgO/Al_2O_3 sorbents were at least partially regenerated, but only those with low Mg loadings recovered enough NO_x storage capacities to allow adequate NSR function during the second SO_2 exposure. The NSR activities observed in the second SO_2 exposure were remarkable especially

considering that these sorbents were completely deactivated by SO_2 in the previous 24-hour operation. This study illustrated the effectiveness of the $Rh/CuO-MgO/Al_2O_3$ sorbents at NSR operation in the presence of SO_2, which could be attributed to their excellent NO_x storage capacity and regeneration efficiency.

Table 4.2. Lean NO conversion over the fresh and regenerated $CuO-MgO/Al_2O_3$ sorbents with 1 wt% Rh, and a total Cu + Mg loading of 30 wt%.

Cu Loading (wt%)	Mg Loading (wt%)	Fresh Sorbent's Activity[a] (%)	Duration (min)	Regenerated Sorbent's Activity[b] (%)
24	6	94	280	86
18	12	97	410	88
12	18	97	440	84
6	24	97	440	83

[a] The fresh sorbent's activity was measured at a space velocity of 32,000 h^{-1} at 300°C with 300 ppm NO, 60 ppm SO_2, and alternating pulses of 7% O_2 for 5 min and 1% CO for 5 min.
[b] The regenerated sorbent's activity was measured at a space velocity of 32,000 h^{-1} at 300°C with 300 ppm NO, and alternating pulses of 7% O_2 for 5 min and 1% CO for 5 min, after regeneration at 500°C with 1.5% CO.

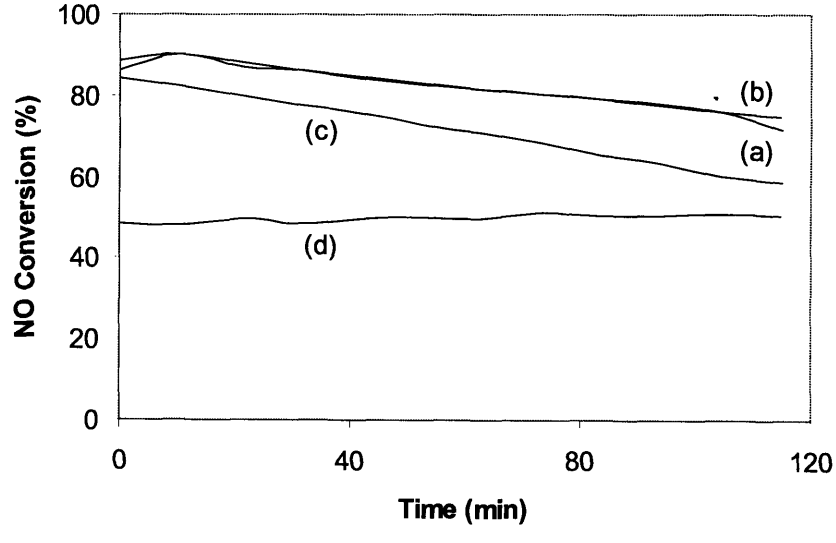

Figure 4.32. Effect of SO_2 exposure on the lean NO conversion of $CuO-MgO/Al_2O_3$ sorbents with 1 wt% Rh, and a total Cu + Mg loading of 30 wt% consisting of (a) 6 wt%, (b) 12 wt%, (c) 18 wt% and (d) 24 wt% Mg at 300°C. The reactions were run at a space velocity of 32,000 h^{-1} with 300 ppm NO, 60 ppm SO_2, and alternating pulses of 7% O_2 for 5 min and 1% CO for 5 min, after regeneration at 500°C with 1.5% CO.

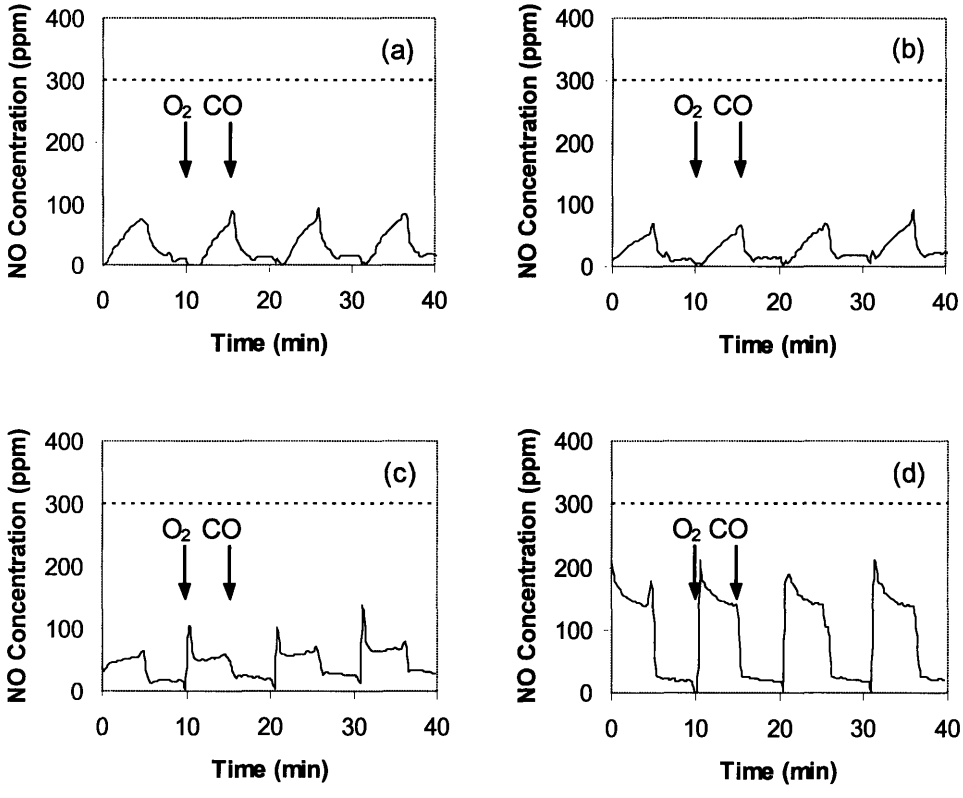

Figure 4.33. Effect of SO_2 exposure on the NO adsorption/desorption profile of regenerated CuO-MgO/Al_2O_3 sorbents with 1 wt% Rh, and a total Cu + Mg loading of 30 wt% consisting of (a) 6 wt%, (b) 12 wt%, (c) 18 wt% and (d) 24 wt% Mg at 300°C. The reactions were run at a space velocity of 32,000 h^{-1} with 300 ppm NO, and alternating pulses of 7% O_2 for 5 min and 1% CO for 5 min, after regeneration at 500°C with 1.5% CO.

4.3.6. Sorbent Characterization

The XRD patterns of the 500°C-calcined CuO-MgO/Al_2O_3 sorbents with 1 wt% Rh and a total Cu + Mg loading of 30 wt% are shown in Figure 4.34. At low Mg loadings, only diffraction peaks associated with CuO were observed, indicating that the Mg species were highly dispersed. At high Mg loadings of $\geq$ 18 wt%, crystalline peaks associated with MgO and $MgAl_2O_4$ became dominant relative to CuO peaks. The diffraction patterns for Rh/CuO-MgO/Al_2O_3 and CuO-MgO/Al_2O_3 sorbents were found to be similar since the Rh dispersion was high in the former.

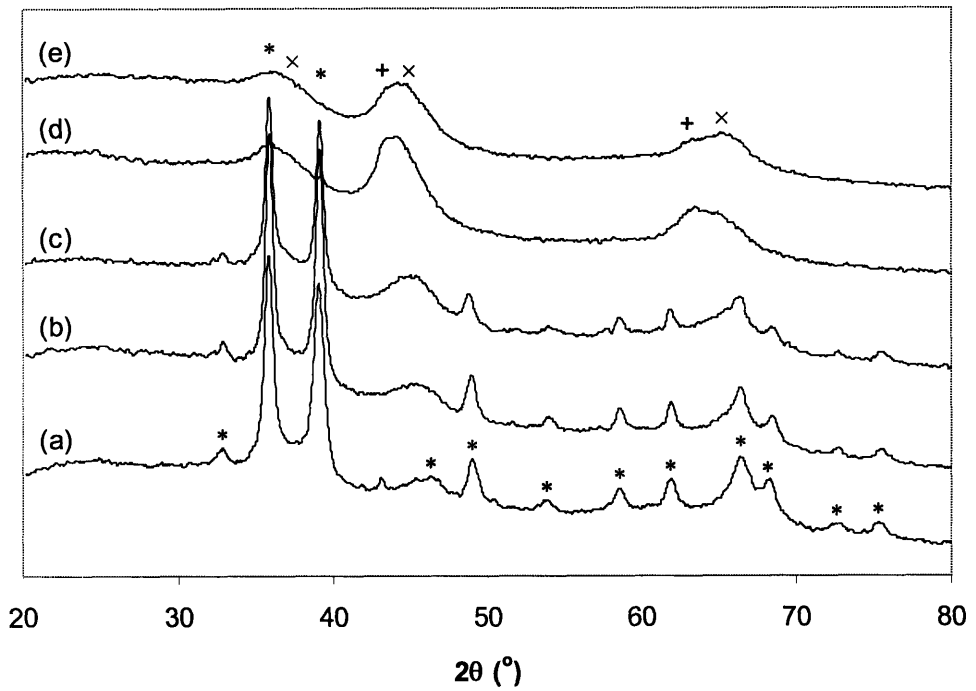

Figure 4.34. XRD patterns of CuO-MgO/Al_2O_3 sorbents with 1 wt% Rh, and a total Cu + Mg loading of 30 wt% consisting of (a) 0 wt%, (b) 6 wt%, (c) 12 wt%, (d) 18 wt% and (e) 24 wt% Mg. Phases present included (*) CuO, (+) MgO, and (×) $MgAl_2O_4$.

The Rh addition, however, brought about reductions in the BET surface area, pore size and pore volume of the CuO-MgO/Al_2O_3 sorbents, possibly due to some pore blockage by Rh. Tables 4.3 and 4.4 also show that the BET surface areas of CuO-MgO/Al_2O_3 and Rh/CuO-MgO/Al_2O_3 sorbents were increased at higher Mg loadings, due to the greater thermal stability imparted by MgO compared to CuO.

Table 4.3. Surface area, pore volume and pore diameter of CuO-MgO/Al_2O_3 sorbents with a total Cu + Mg loading of 30 wt%.

Cu Loading (wt%)	Mg Loading (wt%)	Surface Area (m^2/g)	Pore Volume (cm^3/g)	Pore Diameter (nm)
30	0	238	1.04	13.0
24	6	220	0.78	10.5
18	12	238	0.71	9.2
12	18	257	0.75	8.5
6	24	257	0.66	7.5

Table 4.4. Surface area, pore volume and pore diameter of CuO-MgO/Al_2O_3 sorbents with 1 wt% Rh, and a total Cu + Mg loading of 30 wt%.

Cu Loading (wt%)	Mg Loading (wt%)	Surface Area (m^2/g)	Pore Volume (cm^3/g)	Pore Diameter (nm)
30	0	186	0.47	11.4
24	6	198	0.55	8.5
18	12	205	0.53	7.9
12	18	215	0.54	6.8
6	24	229	0.55	6.6

4.4. Summary

CuO-based nanocomposite sorbents capable of adsorbing NO_x and SO_2 in oxygen-rich environment and releasing N_2 and SO_2 in reducing atmosphere have been successfully derived by sequential precipitation. The noble metal-loaded CuO/Al_2O_3 sorbents were able to maintain stable NSR activities in the presence of SO_2 due to the excellent SO_2 desorption efficiency provided by both CuO and noble metals. With 1 wt% loadings of both Pt and Rh, a stable NO conversion of 70% was achieved over the sorbent with 30 wt% Cu even after 7 hours of NSR operation in the presence of SO_2. However, the intrinsic NO_x storage capacities of these CuO/Al_2O_3 sorbents were low, especially at temperatures above 350°C. By using lower operating temperatures, the NO_x storage capacity, and consequently the NO conversion, could be improved for these sorbents at the expense of their SO_2 desorption efficiency.

The addition of Pt to improve the SO_2 desorption rate of the CuO/Al_2O_3 sorbents also led to reduced stability for the adsorbed nitrate, resulting in poor NO_x adsorption and greater NO oxidation to NO_2. The addition of Rh, on the other hand, significantly promoted the NO_x storage under fuel-lean conditions. In fact, the CuO/Al_2O_3 sorbents with 1 wt% Rh were able to achieve NO conversions of over 90% during NSR operation below 300°C at 16,000 h^{-1}.

For Pt-Rh/CuO/Al_2O_3 sorbents, NO_x storage capacity could be improved through the incorporation of MgO. The addition of just 6 wt% Mg could enhance the NO

breakthrough capacity, and allowed almost complete conversion of NO even at a high space velocity of 32,000 h^{-1}. However, the MgO introduction also increased the SO_2 desorption temperature for the sorbent. Therefore, it was not possible to maintain the high NO conversion of the Pt-Rh/CuO-MgO/Al_2O_3 nanocomposites in the presence of SO_2. Deactivation of the NSR activities could be lessened if Pt was not employed, since Rh/CuO-MgO/Al_2O_3 sorbents possessed higher NO_x storage capacities than Pt-Rh/CuO-MgO/Al_2O_3 sorbents. The optimized system, Rh/CuO-MgO/Al_2O_3 with 12 wt% Mg and 18 wt% Cu, was able to maintain its NSR activity over 6 hours of operation.

The NO_x storage capacities of the aged Rh/CuO-MgO/Al_2O_3 sorbents could be partially regenerated at 500°C under the reducing atmosphere, where NO conversions of over 85% were generally recovered. The effectiveness of this regeneration step was successfully increased with the Cu loading due to better SO_2 desorption efficiency.

4.5. References

[1] B.I. Bertelsen, Top. Catal. 16/17 (2001) 15.

[2] M. Amiridis, T. Zhang, R.J. Farrauto, Appl. Catal. B 10 (1996) 203.

[3] A. Fritz, V. Pitchon, Appl. Catal. B 13 (1997) 1.

[4] R. Burch, J.P. Breen, F.C. Meunier, Appl. Catal. B 39 (2002) 283.

[5] A. Konig, G. Herding, B. Hupfeld, T. Richter, K. Weidmann, Top. Catal. 16/17 (2001) 23.

[6] B. Westerberg, E. Fridell, J. Mol. Catal. A 165 (2001) 249.

[7] F. Prinetto, G. Ghiotti, I. Nova, L. Lietti, E. Tronconi, P. Forzatti, J. Phys. Chem. B 105 (2001) 12732.

[8] C. Hess, J.H. Lunsford, J. Phys. Chem. B 106 (2002) 6358.

[9] S. Hodjati, P. Bernhardt, C. Petit, V. Pitchon, A. Kiennemann, Appl. Catal. B 19 (1998) 209.

[10] E. Fridell, M. Skoglundh, B. Westerberg, S. Johansson, G. Smedler, J. Catal. 183 (1999) 196.

[11] A. Amberntsson, H. Persson, P. Engstrom, B. Kasemo, Appl. Catal. B 31 (2001) 27.

[12] L. Lietti, P. Forzatti, I. Nova, E. Tranconi, J. Catal. 204 (2001) 175.

[13] N.W. Cant, M.J. Patterson, Catal. Today 73 (2002) 271.

[14] P. Engstrom, A. Amberntsson, M. Skoglundh, E. Fridell, G. Smedler, Appl. Catal. B 22 (1999) L241.

[15] H. Mahzoul, L. Limousy, J.F. Brilhac, P. Gilot, J. Anal. Appl. Pyrolysis 56 (2000) 179.

[16] A. Amberntsson, M. Skoglundh, M. Jonsson, E. Fridell, Catal. Today 73 (2002) 279.

[17] C. Courson, A. Khalfi, H. Mahzoul, S. Hodjati, N. Moral, A. Kiennemann, P. Gilot, Catal. Commun. 3 (2002) 471.

[18] P. Pitukmanorom, J.Y. Ying, Metal Oxide Nanocomposites as SO_2 Storage Materials, in preparation, 2004.

[19] G. Centi, S. Perathoner, Appl. Catal. A 132 (1995) 179.

[20] H.Y. Huang, R.Q. Long, R.T. Yang, Energ. Fuel 15 (2001) 205.

[21] T. Nakatsuji, V. Komppa, Appl. Catal. B 30 (2001) 209.

[22] T. Nakatsuji, V. Komppa, Catal. Today 75 (2002) 407.

[23] C.N. Satterfield, Heterogeneous Catalysis in Industrial Practice, 2nd Edition, Krieger Publishing Company, Florida, 1986, p. 328.

Chapter 5 – Conclusions and Recommendations

5.1. Synthesis Technique

High surface area alumina-based nanocomposites with high loadings and good dispersion of active components had been synthesized via a novel sequential precipitation technique. The resulting oxide nanocomposites significantly outperformed the catalysts prepared by conventional synthesis routes in the selective catalytic reduction (SCR) of NO_x by propene, reversible SO_2 storage, and NO_x storage-reduction (NSR). These three reactions are all important to NO_x removal from the exhaust of lean-burn engines.

It would be of interest to apply the sequential precipitation technique to prepare alumina-based catalysts for other catalytic applications. In particular, the approach would be very useful towards synthesizing catalysts with high loadings of active components. In many conventional catalysts, the loading of active components has been kept low deliberately so as to minimize their agglomeration and grain growth. By providing a good dispersion of active components even at high loadings, superior catalysts could be generated for a variety of reactions.

5.2. SCR of NO_x by Hydrocarbons

The In_2O_3-Ga_2O_3/Al_2O_3 nanocomposites developed for the SCR of NO by propene had been shown to be highly active towards the reduction of NO in the oxygen-rich atmosphere that contained a large amount of water vapor. In fact, the 80% N_2 yield achieved over the catalyst with 2 wt% In and 8 wt% Ga was among the highest ever reported in the literature for the SCR of NO_x by hydrocarbons [1]. These In_2O_3-Ga_2O_3/Al_2O_3 nanocomposites also exhibited good poisoning resistance against SO_2 as well as moderate SCR activities by other hydrocarbons, demonstrating an excellent potential for the treatment of real exhausts.

The further development of these catalysts for the SCR of NO_x would greatly benefit from further insights into the reaction mechanisms that governed the reduction of NO_x, the formation of N_2, and the activation of hydrocarbons over the various components of the nanocomposite catalysts. Of special interest were the differences in the reactivity and mechanism between the SCR of NO_x by alkene (propene) and by

alkane (propane) over the In_2O_3-Ga_2O_3/Al_2O_3 nanocomposites. An understanding of these differences could lead to the development of SCR catalysts with active components specifically tailored to target different exhaust stream compositions.

5.3. SO_2 Storage Material

The proposed concept of reversible SO_x trap had been demonstrated through the use of Pt-Rh/CuO/Al_2O_3 sorbents. These nanocomposites exhibited good SO_2 adsorption in the oxidizing atmosphere, and fast SO_2 desorption with CO as the reducing agent. The SO_2 desorption temperature of 400°C was among the lowest reported [2]. To the best of our knowledge, the Pt-Rh/CuO/Al_2O_3 nanocomposites were amongst the first materials reported to show reversible SO_2 sorption behavior at a temperature of relevance to automotive applications.

The performance of the SO_x traps could benefit from reduced CuO grain size through further improvements in the synthesis. Coatings of thermally stable materials could be introduced to suppress the sintering of CuO particles at high temperatures. The effects of these coatings on the SO_2 adsorption and desorption properties should be studied to ensure that the good performance of the Pt-Rh/CuO/Al_2O_3 nanocomposites could be retained.

The CuO/Al_2O_3 nanocomposites loaded with Fe also have potential in the catalytic reduction of SO_2 to elemental sulfur by CO and CH_4. This would be of interest in the application of sulfur recovery from flue gas.

5.4. SO_x-Tolerant NO_x Trap

The benefits of using NO_x sorbent with good SO_2 resistance in the NSR operation had been demonstrated through the use of Rh/CuO-MgO/Al_2O_3 nanocomposites. These novel materials were able to maintain high NO conversion even after prolonged SO_2 exposure, despite being only periodically regenerated at a low temperature of 300°C. Furthermore, the NO_x storage capacities of the fully deactivated Rh/CuO-MgO/Al_2O_3 sorbents could be partially recovered by regeneration at 500°C under CO, with a regenerated NO conversion of > 85%. The performance of these sorbents is comparable

to those recently patented by large automotive catalyst manufacturer [3], suggesting that there are commercial interests for SO_x-tolerant NO_x traps.

Further regeneration studies on the Rh/CuO-MgO/Al_2O_3 sorbents in exhaust streams of more specific compositions would be beneficial since water and other hydrocarbons present might alter the desorption characteristics of both NO_x and SO_2 from the sorbents. The presence of alkenes, such as propene, in the exhaust could also trigger further reduction of NO_x during the lean cycle since CuO/Al_2O_3 has been known for its SCR activity. The composition of the Rh/CuO-MgO/Al_2O_3 nanocomposites could also be tailored to suit the specific needs of the application since these materials could be used either as a SO_x-tolerant NO_x trap by itself, or as a SO_x trap with the conventional NO_x storage material. Such compositional and functional flexibility would allow the performance of the entire system to be optimized.

5.5. References

[1] R. Burch, J.P. Breen, F.C. Meunier, Appl. Catal. B 39 (2002) 283.

[2] L. Limousy, H. Mahzoul, J.F. Brilhac, F. Garin, G. Maire, P. Gilot, Appl. Catal. B 45 (2003) 169.

[3] J.H.-Z. Wu, J.C. Dettling, US Patent 6,699,448 (2004).